Summer 8-15-2021

Co-registered photoacoustic and ultrasound tomographic imaging of human colorectal and ovarian cancer: light delivery, system development, and clinical study

Guang Yang
Washington University in St. Louis

WASHINGTON UNIVERSITY IN ST. LOUIS

Department of Biomedical Engineering

Dissertation Examination Committee:
Quing Zhu, Chair
Samuel Achilefu
Song Hu
Joan Riley
Chao Zhou

Co-registered Photoacoustic and Ultrasound Tomographic Imaging of Human Colorectal and Ovarian Cancer: Light Delivery, System Development, and Clinical Study

by

Guang Yang

A dissertation presented to
The Graduate School
of Washington University in
partial fulfillment of the
requirements for the degree
of Doctor of Philosophy

August 2021
St. Louis, Missouri

Table of Contents

List of Figures

List of Tables

Acknowledgments

First, I would like to express my heartfelt thanks to Dr. Quing Zhu, my Ph.D. supervisor, for her guidance and support throughout my entire Ph.D. She taught me how to behave like a professional researcher, how to write a good paper, and how to work hard and efficiently. Moreover, she gave me precious help on my career pathway and personal life. I feel extremely lucky to have a supervisor and life-time friend like Dr. Zhu.

I acknowledge the value of the critical feedback I received from my thesis committee members, Dr. Zhou, Dr. Hu, Dr. Riley, and Dr. Achilefu, which guided my thesis in the right direction.

I would like to thank all physicians, coordinators, and pathologists especially William who helped to get patients and ex vivo tissue samples.

I am grateful to all my lab mates and friends for their help and support. Specially, Eghbal, Hongbo, Kexin, Shihab, Atahar, Sreyankar, Sitai, Hengbo, Shuang, and Tong, with whom I have directly work in different projects and they also helped me in my projects.

I also want to thank Lin Chen for giving me lots of life experience and suggestions and Prof. James Ballard for the manuscripts and dissertation editing.

I offer special thanks to the Washington University School of Engineering for allowing us to use their dissertation template as a starting point for the development of this document.

Guang Yang

Washington University in St. Louis

August 2021

Dedicated to my family: Yong Yang, Yulin Li, Huijuan Xie, and Blair Yang.

ABSTRACT OF THE DISSERTATION

Co-registered Photoacoustic and Ultrasound Tomographic Imaging of Human Colorectal and Ovarian Cancer: Light Delivery, System Development, and Clinical Study

by

Guang Yang

Doctor of Philosophy in Biomedical Engineering

Washington University in St. Louis, 2021

Professor Quing Zhu, Chair

Ovarian cancer remains the deadliest of all the gynecological malignancies. Conventional screening tests, including pelvic examination, transvaginal ultrasound (TVUS), and blood testing for cancer antigen 125 (CA-125), lack sufficient specificity for early ovarian cancer diagnosis. Imaging modalities such as computed tomography (CT), positron emission tomography (PET), and magnetic resonance imaging (MRI) have been used for surgical guidance. However, all of these modalities have limitations in detecting small lesions.

Globally, colorectal cancer is the second most commonly diagnosed malignancy and the fourth most common cause of cancer mortality. Accurate staging and post-treatment surveillance of this prevalent disease are critical because treatment strategies are predicated upon the stage at presentation and the patient's response to pre-surgical therapy – in some instances, detailed imaging allows certain patients to avoid surgery altogether. While colonoscopy and biopsy are the gold-standard diagnostic tests for colorectal cancers, multiple imaging modalities are also utilized, including optical imaging, endoscopic ultrasound (EUS), pelvic magnetic resonance imaging (MRI), computed tomography (CT), and positron emission tomography (PET). Unfortunately, each of these modalities has critical weakness in evaluating colorectal tumors. In staging colorectal

tumors and evaluating their therapeutic response, more precise imaging modalities could transform the standard of care.

This dissertation explores co-registered photoacoustic and ultrasound tomographic imaging of two fatal cancers: ovarian cancer and colorectal cancer. It is composed of three main parts: light delivery optimization/fiber optics, system development and optimization, and pilot patient and sample study.

To begin, we designed, optimized, and evaluated an hand-held photoacoustic and ultrasound probe suitable for endo-cavity subsurface tumor imaging. Compared to previous designs, the prototype probe, consisting of four 1 mm multi-mode optical fibers attached to 1.5 mm diameter ball-shaped fiber tips sandwiched between a transvaginal ultrasound transducer and a custom-made sheath, demonstrated a higher light output and better beam homogeneity on the tissue subsurface.

Second, we developed a novel fiber diffuser tip using microspheres dispersed within an ultraviolet (UV) adhesive to scatter light. This diffuser keeps the skin surface fluence under the maximum permissible exposure (MPE), while enabling higher laser energy injection to enhance the photoacoustic (PA) signal generated from the tissue.

Third, we proposed an improved beamformer, named lag-based delay multiply and sum combined with coherence factor (DMAS-LAG-CF). Simulations and phantom experiments demonstrate that compared with conventional delay and sum (DAS), the proposed algorithm can provide 1.39 times better resolution and 10.77 dB higher contrast. For patient data, similar improvements in contrast ratios have been observed. However, since diagnostic accuracy in distinguishing between cancer and benign/normal groups is the significant measure, we have extracted the photoacoustic histogram features of mean, kurtosis, and skewness. When mean and skewness are used as features,

DMAS-LAG-CF can improve cancer diagnosis, with an AUC of 0.91 in differentiating malignant from benign ovarian lesions.

Fourth, to investigate the ability of co-registered photoacoustic and ultrasound tomographic imaging to assess human colorectal cancer, we conducted a pilot study on 23 *ex-vivo* human colorectal tissue samples that were collected immediately after surgical resection. Co-registered photoacoustic images of malignancies showed significantly increased PAT signals compared to normal regions of the same sample. We found statistically significant differences between untreated colorectal tumors and normal tissues, based on the quantitative relative total hemoglobin concentration (rHbT) computed from four optical wavelengths, spectral features such as the mean spectral slope and 0.5 MHz intercept extracted from PAT and US spectral data, and image features such as the first and second order statistics along with the standard deviation of the mean radon transform of PAT images. Using either a logistic regression model or a support vector machine, the best set of parameters of rHbT and PAT intercept achieved AUC values of 0.97 and 0.95 for the training and testing data sets, respectively, in predicting histologically confirmed invasive carcinoma. One limitation of the current system is its poor image resolution (~ 250 μm axial resolution) limited by the commercial endo-cavity ultrasound transducer array (6 MHz central frequency, 80% bandwidth). For better image resolution in high frequency PAT/US imaging, we first decoded the pin configuration of a high-frequency transducer array (15 MHz central frequency, 9-18 MHz bandwidth) and adapted it to our home-made 128 channel ultrasound pulsing and receiving system (sampling rate: 40 MHz). To further improve the performance, we are building a 64-channel FPGA-based high frequency photoacoustic imaging system with a sampling rate of 80 MHz and signal-to-noise ratio (SNR) of 40 dB. For *in-vivo* patient study, this system will be integrated with an endo-rectal probe with a side-firing fiber tip.

Fifth, we investigated the laser safety of photoacoustic imaging, in preparation for its use in clinical reproductive medicine. Using preimplantation mouse blastocyst stage embryos, we assessed potential DNA damage from photoacoustic laser exposure. Different embryo groups were exposed to either 5- or 10- minute 15-Hz laser doses (typical clinical doses), or a 1-minute 1-kHz laser dose (a significantly higher dose). We demonstrated that typical lasers and exposure times used for photoacoustic imaging do not induce increased cell death in mouse blastocysts.

Sixth, we demonstrated a novel fiber endface photoacoustic generator using IR 144 laser dye dispersed within an ultraviolet (UV) adhesive. The generator provides wide acoustic bandwidth in the transducer frequency range of 2-7 MHz, high thermal conversion efficiency (> 90%), good PA intensity controllability (via the easily controlled IR 144 concentration), and high feasibility (simple procedures). Through a series of experimental validations, we show this fiber-based endface photoacoustic generator can be a useful tool for a broad range of biomedical applications, such as calibrating the local absorption coefficient of biological tissue for quantitative photoacoustic tomography.

Chapter 1: Introduction

Ovarian cancer remains the deadliest of all the gynecological malignancies. According to the American Cancer Society, 21,750 women in the United States were diagnosed with ovarian cancer in 2020, and 13,940 deaths were reported [1]. Colorectal cancer is the second most common malignancy diagnosed globally and the fourth leading cause of cancer mortality, with more than 100,000 new cases diagnosed annually in the US [1-2]. Photoacoustic imaging (PAI), also known as optoacoustic imaging (OA), is an emerging biomedical imaging modality that uses the resolution of ultrasound imaging and the contrast of optical imaging to provide structural and functional information [3-4]. Optical absorption, the main PA contrast, is directly related to tumor angiogenesis and tumor hypoxia. Tumor angiogenesis and oxygen consumption are significant indicators for tumor growth, metastasis, and therapeutic response [5-6]. PAI has demonstrated its potential for image-guided diagnosis in oncology (e.g., breast [7-9], thyroid [10-11], cervical [12], colorectal [13], ovarian [14-17], and prostate cancers [18-19]), peripheral vascular diseases (PVDs) [20], joint inflammations [21-23], and skin diseases [24-26]. Our lab focuses on assessment of human ovarian cancer and colorectal cancer using co-registered multispectral photoacoustic and ultrasound tomographic imaging. Because two or more optical wavelengths are used, photoacoustic waves can be used to reconstruct the distribution of oxygenated and deoxygenated hemoglobin, which are the main chromophores related to tumor angiogenesis and hypoxia. Oxygen saturation (sO_2) can then be measured, which is an important indicator of tumor metabolism and therapeutic response [14].

This thesis begins by introducing facts about and known causes of ovarian cancer, colorectal cancer, and surface tumors, then it describes conventional screening, staging, and treatment

response monitoring methods. It also discusses the principles of PAI and its clinical applications especially in oncology. Finally, we introduce the progress of our lab's work on co-registered photoacoustic and ultrasound tomographic (PAT/US) imaging.

In Chapter Two, we report the optimal design, implementation, and evaluation of an optical fiber-based transvaginal PAT/US imaging probe for endo-cavity imaging of adenocarcinomas.

In Chapter Three, we develop an effective fiber diffuser tip to reduce the fluence on the target tissue surface while injecting more laser energy and enhancing the photoacoustic signal generated from the tissue.

In Chapter Four, we propose an improved beamformer, named lag-based delay multiply and sum combined with coherence factor (DMAS-LAG-CF), to improve spatial resolution and image contrast for better in vivo ovarian cancer diagnosis.

In Chapter Five, to investigate the ability of co-registered PAT/US imaging to assess human colorectal cancer, we describe a pilot study on 23 *ex-vivo* human colorectal tissue samples collected immediately after surgical resection. To improve the spatial resolution of the current system, we have built a 64-channel FPGA based high frequency photoacoustic imaging system with a sampling rate of 80 MHz and signal-to-noise ratio (SNR) of 40 dB. For *in-vivo* patient study, we have integrated this system with a commercial endo-rectal probe with a side-firing fiber tip.

In Chapter Six, we investigate the laser safety of photoacoustic imaging, with an eye to its adoption by clinical reproductive medicine: using preimplantation mouse blastocyst stage embryos, we examine potential DNA damage from photoacoustic laser exposure.

In Chapter Seven, we develope a novel fiber endface photoacoustic generator that provides wide acoustic bandwidth, high thermal conversion efficiency, good PA intensity controllability, and high feasibility.

In Chapter Eight, we summarize the dissertation and present possible directions for future work in transmission-mode ultrasound imaging using the fiber endface photoacoustic generator. We also propose using photoacoustic remote-sensing imaging to evaluate human ovarian cancer and colorectal cancer.

1.1 Cancer

1.1.1 Ovarian Cancer

Ranking fifth among fatal cancers affecting women, ovarian cancer accounts for more deaths than any other cancer of the female reproductive system. According to the American Cancer Society, in 2020, about 21,750 women received a new diagnosis of ovarian cancer and about 13,940 women died from ovarian cancer. Due to the lack of early screening and diagnostic techniques, many women are diagnosed with ovarian cancer when it is already at stages III or IV, where the mortality rates are high (70 to 75%). Conventional screening tests, including pelvic examination, transvaginal ultrasound (TVUS), and blood testing for cancer antigen 125 (CA-125), lack sufficient specificity for early ovarian cancer diagnosis. Imaging modalities such as computed tomography (CT), positron emission tomography (PET), and magnetic resonance imaging (MRI) have been used for surgical guidance. However, all of these modalities have limitations in detecting small lesions. In previous work, to address this limitation, we developed a co-registered photoacoustic and TVUS technique to improve ovarian cancer diagnosis.

1.1.2 Colorectal Cancer

Adenocarcinoma of the colon and rectum is the second most common malignancy diagnosed globally and the 4th leading cause of cancer mortality. Accurate staging and post-treatment surveillance of this prevalent disease are critical because treatment strategies are predicated upon the stage at presentation and the response to pre-surgical therapy—in some instances, detailed imaging allows certain patients to avoid surgery altogether. Colonoscopy and biopsy are the gold-standard diagnostic tests for colorectal cancers. They work reasonably well for diagnosis/screening, but are not used for staging and monitoring treatment response. Endoscopic ultrasound (EUS) and magnetic resonance imaging (MRI) are good for staging, but not used for monitoring treatment response. Also, MRI is costly. Computed tomography (CT) and positron emission tomography (PET) are not used much: they suffer from low specificity and sensitivity, and they require radiation. New imaging modalities to stage cancer's invasion and predict the patient's therapeutic response could greatly improve patient outcomes.

1.1.3 Surface Tumor

Adenocarcinoma is a type of cancerous tissue that forms in mucus-secreting glands throughout the body. For example, adenocarcinomas make up around 96% of colorectal cancers, and some cervical cancers (10%) are also adenocarcinomas. The depth of invasion for early stage adenocarcinoma is generally between 1 mm to 7 mm. For example, the stromal invasion depth for cervical adenocarcinoma has been measured by microscopy to be 5 mm or less from the base of the epithelium, with a horizontal spread of 7 mm or less. Previously, our group designed several optical fiber-based transvaginal PAT/US imaging probes for ovarian cancer diagnosis. In the design presented here, the 8 to 10 mm thick vaginal muscle wall functions as the light diffuser to

homogenize the light beam before it reaches the ovary. However, the light beam is not optimized for endo-cavity imaging of surface tumors, such as adenocarcinomas.

1.2 Photoacoustic Imaging

1.2.1 The Principles of Photoacoustic Imaging

PAI works on the basic principle of the PA effect, where usually a light beam (usually from a laser) with a short pulse width (pulse duration < 10 ns) illuminates the target tissue. For efficient generation of PA waves, the pulse duration of the laser should be within the thermal relaxation time and stress relaxation time, i.e., the excitation is in thermal and stress confinement. Upon laser irradiation, chromophores in the tissue (such as blood, melanin, lipid, and water) absorb the light and convert it into heat, generating a local temperature rise. This temperature rise creates a thermos-elastic expansion (the so-called initial pressure rise) that generates an acoustic wave. The propagation of successive acoustic waves is finally detected by ultrasonic transducers. Because sound scatters 1000 times less than light in tissue, the acoustic signal propagates much farther in biological tissue without significant attenuation. The absorber size and the pulse width of the laser excitation dictate the bandwidth of the generated acoustic wave (ranging from several tens of hertz to hundreds of megahertz).

Because each tissue chromophore exhibits its own characteristic absorption spectrum, conducting PAI at multiple wavelengths allows their relative quantification and helps to investigate physiological changes in disorders. This information can reveal the mechanism behind the disorders and suggest how they can be managed effectively.

Generally, PAT systems can be grouped into two configurations subjected to their combination of optical illumination methods and acoustic detection methods: photoacoustic microscopy (PAM) which is based on mechanical scanning of a focused or diffused excitation light beam and a focused single element ultrasonic transducer (Figure 1.1 (a)-(c)) and photoacoustic computed tomography (PACT) which is inverse reconstruction image formation, based on widefield light illumination and acoustic detection at multiple locations (Figure 1.1 (d)-(g)). PAI can also be implemented for endoscopy (Figure 1.1 (h)). Furthermore, because it combines optical excitation with acoustic detection, PAI is compatible with complementary imaging modalities, especially the following co-registered photoacoustic and ultrasound tomographic imaging in chapter 1.3.

PAM can be further classified into optical-resolution PAM (OR-PAM) (Figure 1.1 (a) and (b)) and acoustic-resolution PAM (AR-PAM) (Figure 1.1 (c)) depending on usage of ultrasound focusing, or light focusing, or both to achieve improved spatial resolution images. In both OR-PAM and AR-PAM, the axial resolution is determined acoustically. In OR-PAM, the optically determined lateral resolution is typically finer than the axial resolution. Conversely, in AR-PAM, the axial resolution is typically finer than the lateral resolution.

PACT can be configured with a 1D ultrasonic transducer array (Figure 1.1 (d) and (e)), a 2D transducer array (Figure 1.1 (f)), or their scanning equivalents (Figure 1.1 (g)).

The imaging depth of PAI scales over a wide range from the quasi-ballistic regime (typically ≤ 1 mm in tissue) to the diffuse regime (typically ≥ 10 mm in tissue), up to the dissipation limit (~ 10 cm in tissue). Reducing the imaging depth of PAI improves its spatial resolution in approximate proportion. As a rule of thumb, the ratio of the imaging depth to the resolution is ~ 200, permitting PAI to provide high-resolution imaging across a wide range of imaging depths (Figure 1.2).

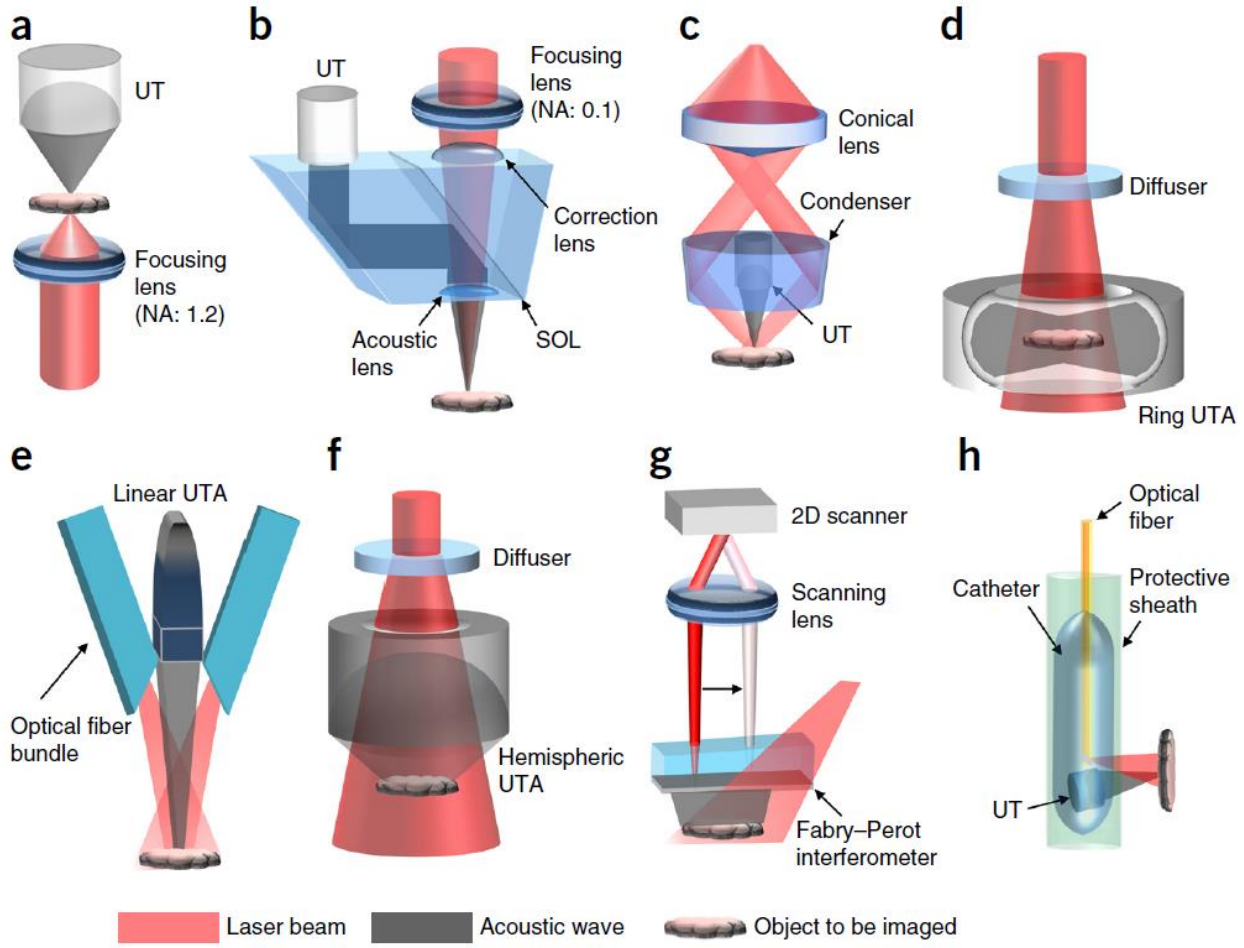

Figure 1.1: Schematic of major embodiments of photoacoustic imaging (from Ref. [4]). (a) Transmission-mode OR-PAM system, where the ultrasonic transducer (UT) and the water-immersion focusing lens are on opposite sides of the object. (b) Reflection-mode OR-PAM system with an optical-acoustic combiner that transmits light but reflect sound. (c) AR-PAM system with a dark-field illumination. The laser light is only weakly focused, with the UT in the dark cone. (d) PACT system with a ring-shaped ultrasonic transducer array (UTA). The laser beam is expanded and homogenized by a diffuser to provide widefield illumination. (e) PACT system with a linear UTA. The excitation light is delivered through a fused-end, bifurcated fiber bundle that flanks both sides of the UTA. (f) PACT system with a hemispherically shaped UTA. The UTA is rotated around the object to be imaged to provide dense spatial sampling for 3D imaging. (g) PACT system

with a 2D Fabry-Perot interferometer as the acoustic sensor. The PA waves are recorded by raster scanning a probing laser beam over the surface of the interferometer. (h) Side-viewing intravascular PA catheter with an outer diameter of 1.25 mm, including the protective sheath in which the catheter rotates.

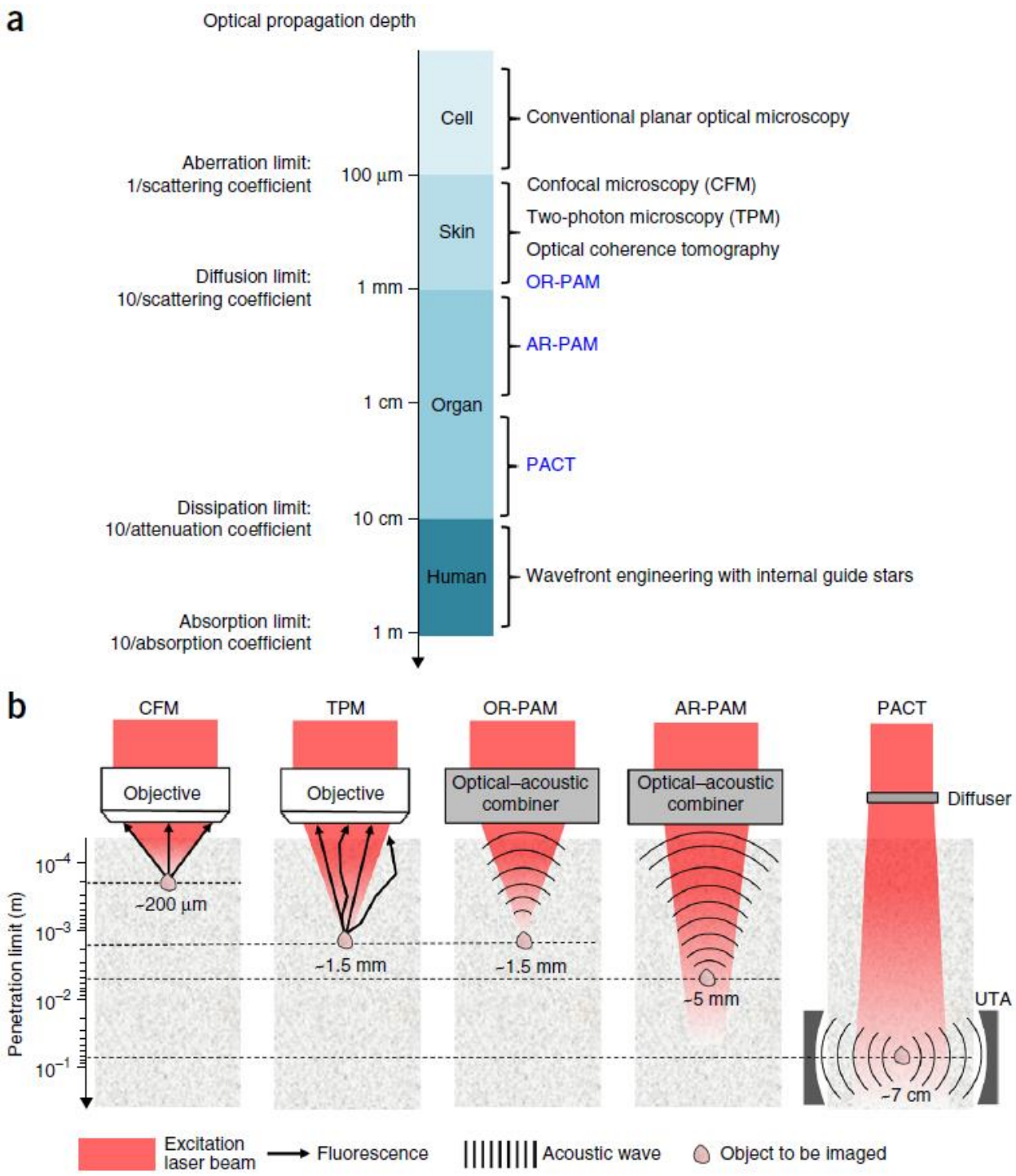

Figure 1.2: Photon propagation regimes in soft tissue and the penetration limits of representative high-resolution optical imaging modalities (from Ref. [4]). (a) Photon propagation regimes in soft tissue and association with the penetration limits of high-resolution optical imaging modalities.

The four regimes are divided at photon propagation depths of approximately 0.1 mm (aberration limit), 1 mm (diffusion limit), 10 cm (dissipation limit), and 1 m (absorption limit), with an optical absorption coefficient of 0.1 cm^{-1}, optical scattering coefficient of 100 cm^{-1} and anisotropy of 0.9. The classification holds in the optical-scattering-dominant media. Note that the penetration limits shown here are order-of-magnitude approximations and the penetration of wavefront engineering is a theoretical projection. (b) Single generation and detection in confocal microscopy (CFM), two-photon microscopy (TPM) and PAT, with different penetration limits in scattering tissue. The colors shown for the excitation light do not represent the true optical wavelengths.

1.2.2 The Clinical Applications of PAT

Breast Imaging

Photoacoustic imaging of the breast has garnered immense interest among researchers worldwide owing to the penetration depth it can comfortably achieve to over the entire, if not most of the breasts. Breast cancer is the most common cancer in women and a leading cause of cancer-related death worldwide. Oraevsky et al. demonstrated the first use of PAI for breast imaging in patients as early as 2001 [31]. Then Manohar et al. applied the Twente Photoacoustic Mammoscope to human breast imaging and near-infrared photoacoustic images of regions-of-interest in 4 of the 5 cases of patients with symptomatic breast reveal higher intensity which is attributed to vascular distribution associated with cancer [32]. Ermilov et al. designed, fabricated, and tested the laser optoacoustic imaging system for breast cancer detection (LOIS-64). They used LOIS-64 to perform a preliminary clinical studies on 27 patients [33]. Kruger et al. developed a dedicated breast photoacoustic mammography system using a spherical detector aperture of 512 elements [34]. They imaged four human volunteers and the vasculature was well visualized throughout the

breast tissue, including to the chest wall. Kitai et al. developed a photoacoustic system wherein the patients again lie in a prone position with the breast suspended and compressed between two plates and illuminated through both plates [35]. Since multiple wavelengths were used, they calculated sO_2 from 26 patients, and all detected lesions showed lower sO_2 levels as compared to the surrounding and contralateral breast tissues. Diot et al. introduced fast handheld multispectral optoacoustic tomography (MSOT) of the breast at 28 wavelengths, aiming to identify high-resolution optoacoustic patterns of breast cancer and noncancerous breast tissue [36]. Very recently, two high impact system and clinical trials have been developed and performed for breast cancer imaging [37, 7-9]. Neuschler et al. completed a large multicenter prospective clinical trial of over 2000 women, using the photoacoustic imaging system developed by Seno Medical Instruments. The combination of PAT and US exceeded US specificity by 14.9% with similar sensitivity (US: 96% vs. 98.6%) [37]. Lin et al. developed a single-breath-hold photoacoustic computed tomography (SBH-PACT) system to reveal detailed angiographic structures in human breasts as shown in Figure 1.3 [8]. SBH-PACT features a deep penetration depth (4 cm in vivo) with high spatial and temporal resolutions (255 μm in plane resolution and a 10 Hz 2D frame rate). By scanning the entire breast within a single breath hold (~ 15 s), a volumetric image can be acquired and subsequently reconstructed. They also demonstrated multipurpose imaging to reveal detailed angiographic information in biological tissues ranging from the rodent brain to the human breast [9].

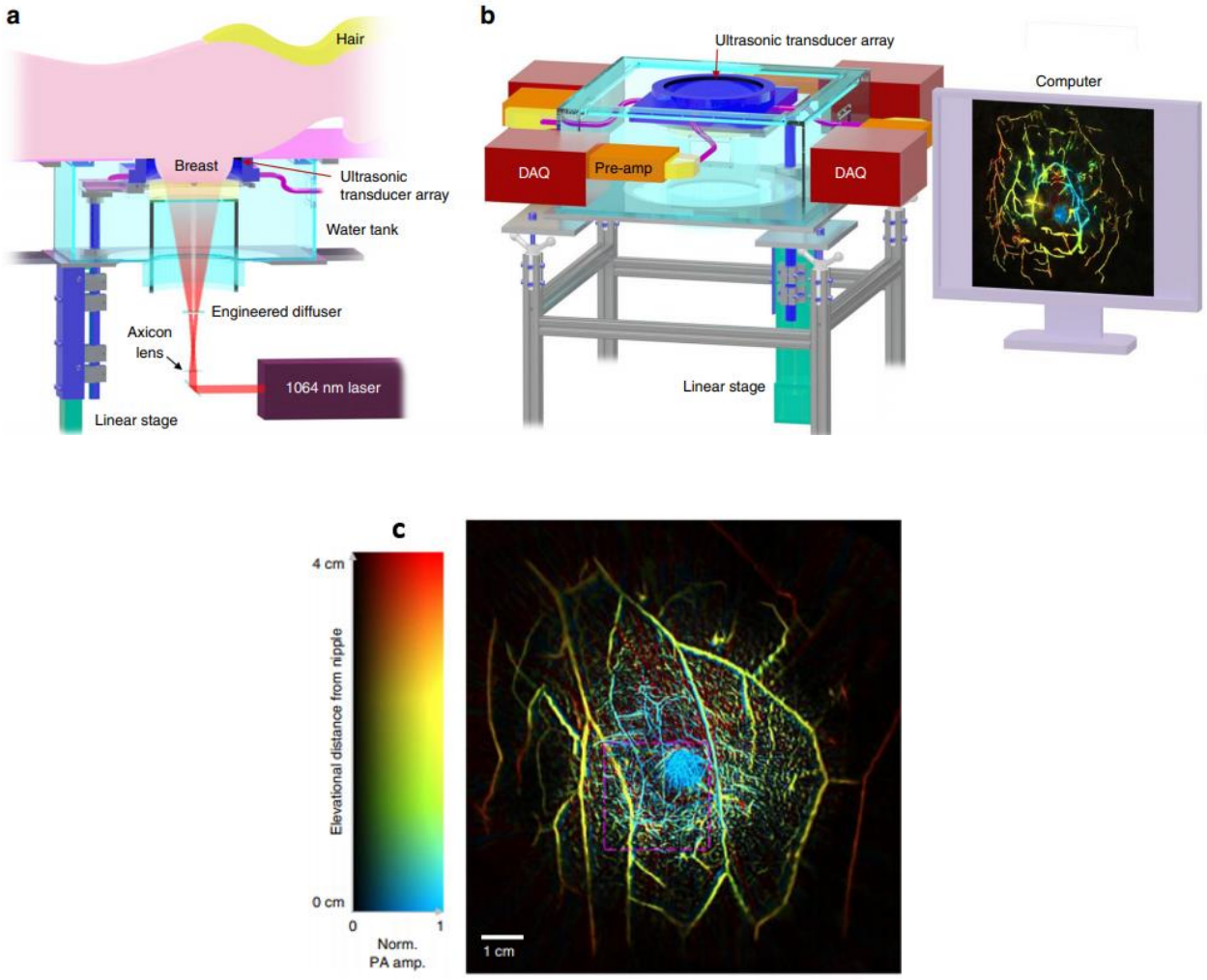

Figure 1.3: Representations of the SBH-PACT system and healthy breast imaging (from Ref. [8]). a Perspective cut-away view of the system with data acquisition components removed. b Perspective view of the system with patient bed and optical components removed. c Vasculature in the right breast of a 27-year-old healthy female volunteer with color-encoded depths.

Brain Imaging

Clinical brain imaging is one of the most challenging applications for photoacoustic imaging, due to strong optical scattering by the skull and brain tissue, which severely limits the optical fluence. Furthermore, the acoustic signal became distorted and attenuated on transit from the brain back through the skull and scalp. Multiple studies have performed photoacoustic brain imaging in small animals in vivo using PAT. Wang et al. firstly reported in vivo noninvasive transdermal and transcranial imaging of the structure and function of rat brain by means of laser-induced photoacoustic tomography (PAT) [38]. Nasiriavanaki et al. developed a functional connectivity photoacoustic tomography system, which allows noninvasive imaging of resting-state functional connectivity in the mouse brain, with a large field of view and a high spatial resolution [39]. Laufer et al. applied a Fabry-Perot polymer film sensing interferometer to image the mouse brain [40]. Noninvasive images of the vasculature in the mouse brain were obtained at different wavelengths between 590 and 889 nm, showing that the cerebral vascular anatomy can be visualized with high contrast and spatial resolution to depths up to 3.7 mm. Zhang et al. reported a PACT system equipped with a high frequency linear transducer array for mapping the microvascular network of a whole mouse brain with the skull intact and studying its hemodynamic activities [41]. Gottschalk et al. demonstrated both ex vivo and non-invasive in vivo functional optoacoustic (OA) neuroimaging of mice expressing the genetically encoded calcium indicator GCaMP6f [42] as shown in Figure 1.4. The approach offers rapid, high-resolution three-dimensional snapshots of whole-brain neuronal activity maps using single OA excitations. Very recently, a few studies have addressed its feasibility on human brain imaging [27, 43]. Wang et al. conducted experiments to examine the feasibility of functional imaging of neonatal brains in a noninvasive transcranial manner by using reflection mode photoacoustic technique for the first time [43]. Nie et al.

demonstrated the feasibility of PAT through a whole adult human skull for the first time by using a photon recycler to increase light transmittance through the skull [27].

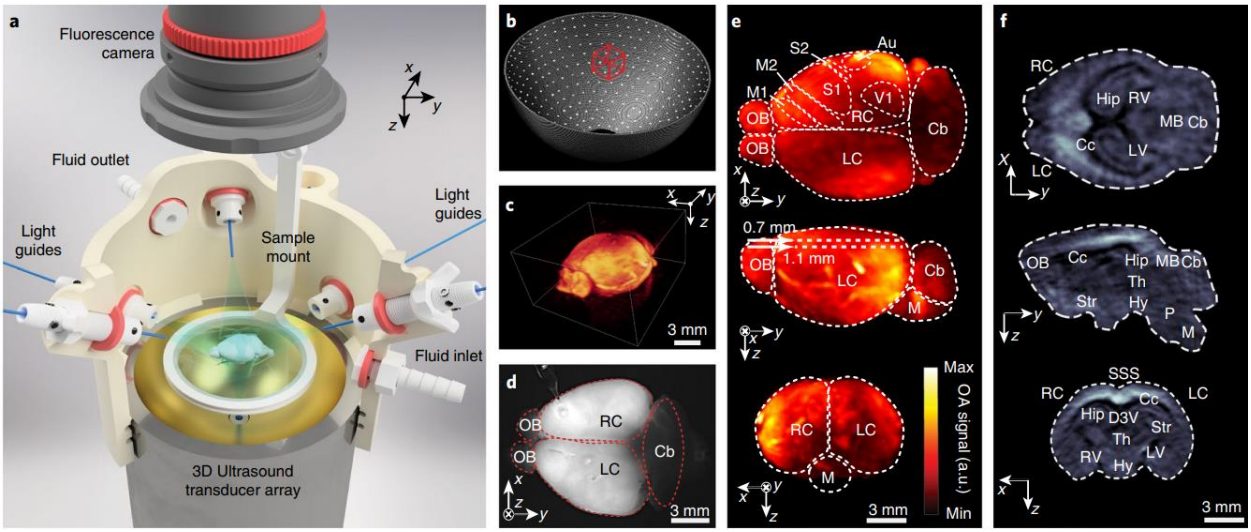

Figure 1.4: Bi-modal OA and fluorescence imaging of isolated brains (from Ref. [42]). a, 3D rendering the imaging setup featuring a 512-element spherical matrix transducer array inserted into a custom-made 3D-printed holder. The holder features an inlet and outlet to facilitate perfusion with ACSF while the excised brain in placed on top of a transparent polyethylene foil that is attached to the submerged sample mount. The brain is evenly illuminated via seven light guides (fibers) and a sensitive scientific complementary metal-oxide semiconductor camera is positioned at the top for concurrent wide-field fluorescence imaging. b, Distribution of detection elements on the spherical array, with its effective volumetric imaging FOV indicated by the red bounding box. c, Representative volumetric OA data recorded from an excised GCaMP6f-expressing brain at an excitation wavelength of 488 nm. d, Corresponding planar fluorescence image. The glass capillary visible on top of the right cortex (RC) was used for intracortical injections. e, Maximum intensity projections (axial, top; sagittal, middle; and coronal, bottom) of the 3D OA dataset shown in c. f,

Representative coronal (top), sagittal (middle) and transverse orthoslices (bottom) of the 3D OA image acquired at 590 nm.

Gastrointestinal Imaging

Under acute conditions of the clinical phenotypes of inflammatory bowel diseases i.e. Crohn's disease (CD) and ulcerative colitis, the care management entails constant adjustment of therapeutic interventions to avoid severe irreversible complications. As shown in Figure 1.5, Knieling et al. conducted a pioneering study involving 108 patients with varying degrees of CD severity [28]. They used a clinical MSOT Acuity system fitted with a handheld detector (3 – 4 MHz, 256 transducer elements) to acquire images from abdomen and monitor the changes in colon upon inflammation. This study demonstrated a major distinction in single wavelength data at 760 nm and HbT signals between patients who show no inflammation in the intestines via scope and those with low grade inflammation. Future more, Waldner et al. show a continuous increase of total and HbO_2 content and sO_2 in the intestinal wall correlating with endoscopic and microscopic intestinal inflammation [44]. Thus, multispectral optoacoustic tomography seems a promising approach to quickly and noninvasively evaluate disease activity in CD patients and might therefore serve as a tool to more rapidly adapt therapy regimes to personal needs.

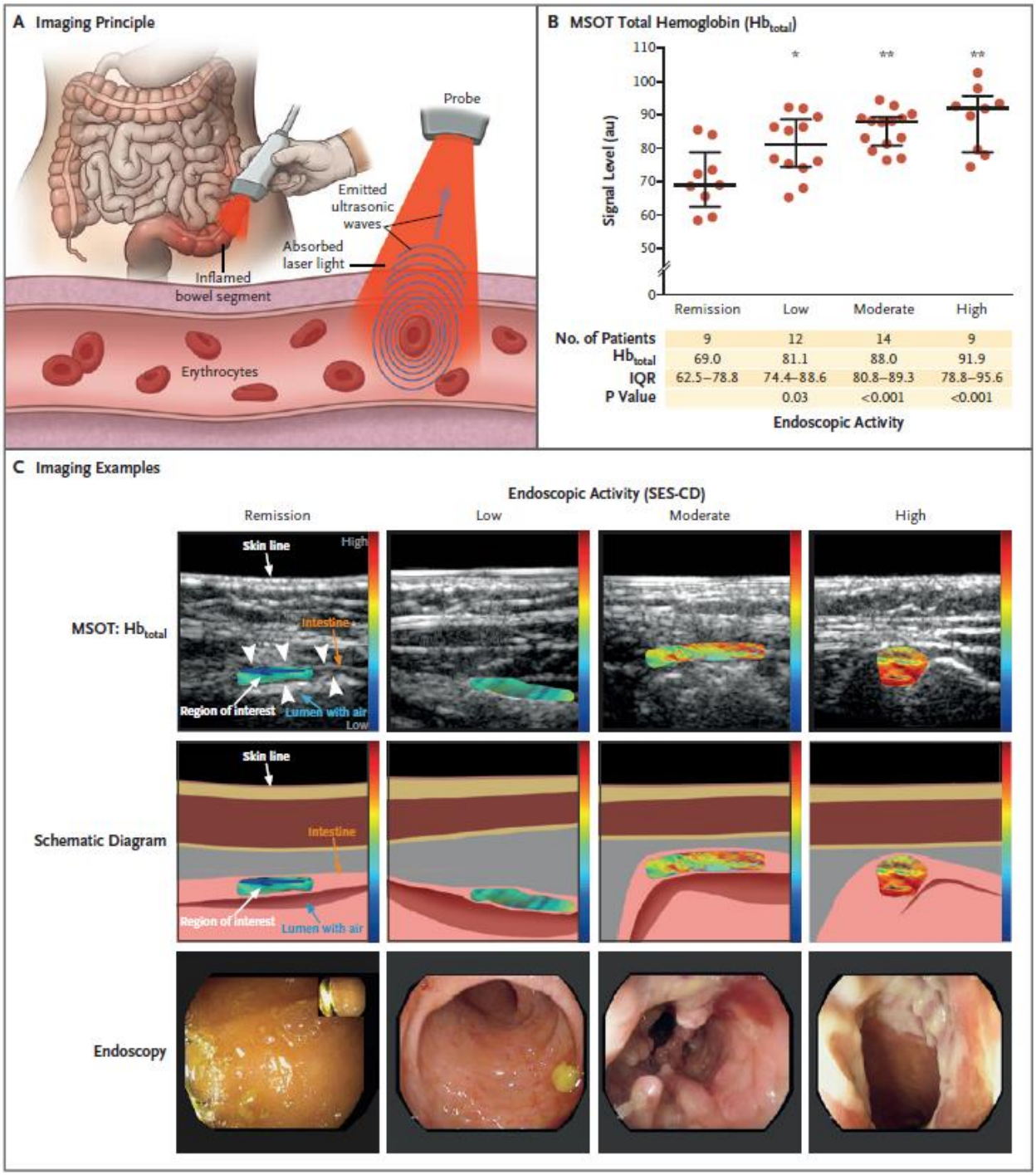

Figure 1.5: MSOT imaging for the assessment of Crohn's Disease activity (from Ref. [28]). A, the transabdominal imaging approach, which uses the same detector for laser light emission and ultrasonic detection of signal levels by means of MSOT. B, MSOT-derived total Hb signal levels

in the intestinal wall (in both the large bowel and the small intestine) in 44 patients with Crohn's disease with different degrees of endoscopic inflammation. C, representative images of MSOT measurements of total Hb in the large bowel and small intestine in patients with different grades of endoscopic disease activity.

Gynecological and Urologic Imaging

Both the male and female reproductive and urological systems present attractive clinical opportunities for PAT since the illumination and acoustic detection can be positioned in relative proximity to the target organ by using an endocavity device, such as in the prostate imaging. Wang et al. demonstrated the feasibility of photoacoustic tomography (PAT) for noninvasive imaging of prostate cancer through the study on a canine model in vivo [45]. Yassen et al. developed a laser OA imaging system for the prostate [46]. The system consists of a fiber-coupled Q-switched laser operating at 757 nm, a commercial 128-channel ultrasonic probe, a digital signal processor, and software that uses the filtered radial back-projection algorithm for image reconstruction. The system is used to reconstruct OA images of a blood-rich lesion induced in vivo in a canine prostate. Kumon et al. performed a frequency-domain analysis of the radio-frequency signals from photoacoustic imaging to generate quantitative parameters for classification of representing prostate adenocarcinoma tumors and adjacent normal flank tissue in a murine model [47]. Dogra et al. validated that ex-vivo multispectral photoacoustic imaging can differentiate between malignant prostate tissue, benign prostatic hyperplasia, and normal prostate tissue involving a total of 30 patients undergoing prostatectomy for biopsy-confirmed prostate cancer [19]. Horiguchi et al. developed the first combined ultrasonic/ photoacoustic device for clinical use and tested it in a pilot study on seven patients to improve real-time visualization of the neurovascular bundle during radical prostatectomy [48]. Very recently, Kothapalli et al. reported the development and bench-

to-bedside translation of an integrated TURS and photoacoustic (TRUSPA) device as shown in Figure 1.6 [29]. TRUSPA uses a miniaturized capacitive micro-machined ultrasonic transducer array for simultaneous imaging of anatomical and molecular optical contrasts [intrinsic: hemoglobin; extrinsic: intravenous indocyanine green (ICG)] of the human prostate. In conclusion, TRUSPA has high potential to differentiate clinically relevant and insignificant PCa cancers, replace/reduce random biopsies with targeted biopsies, and help select suitable treatment options.

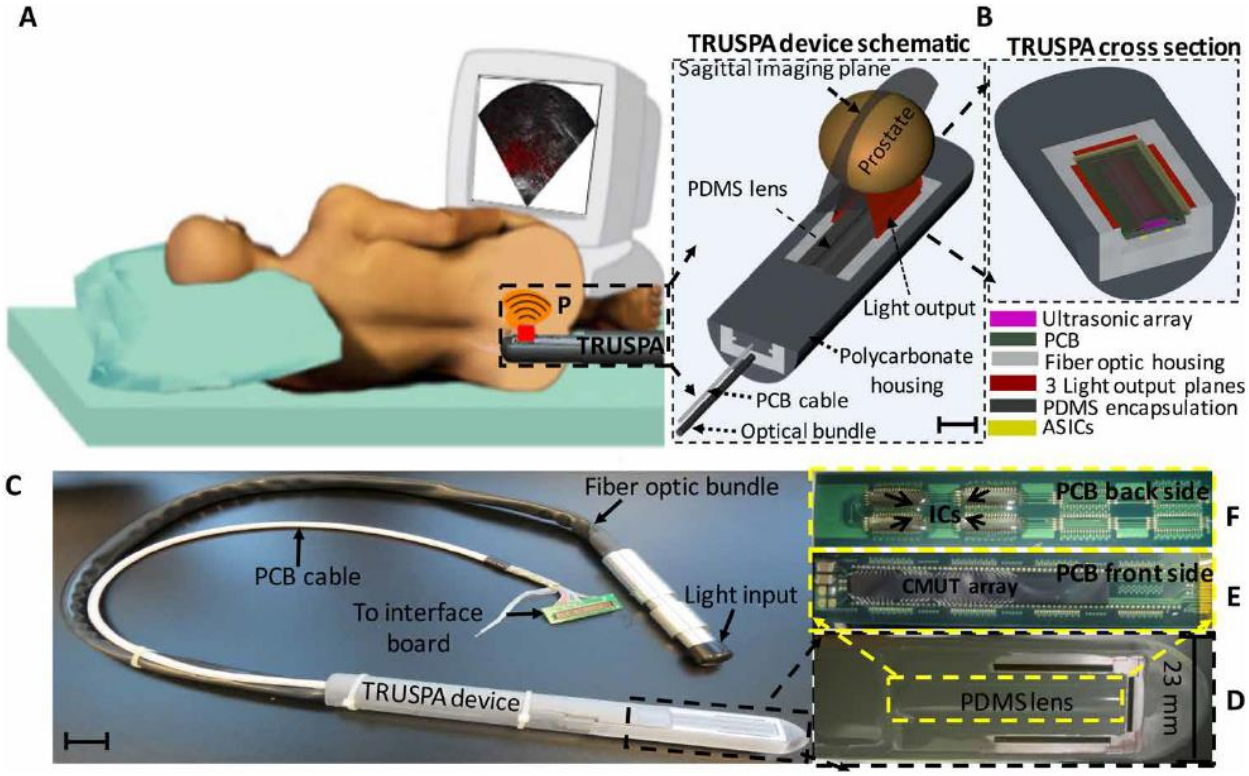

Figure 1.6: Schematics and photographs of TRUSPA imaging of the human prostate (from Ref. [29]). (A) Schematic representation of transrectal imaging of prostate (P) using the TRUSPA device. (B) Schematics of the distal end of the TRUSPA device and its cross section showing key components. (C) Photograph of the TRUSPA device with a 23-mm scale bar. (D) Magnified photograph showing the distal end of the device that is inserted into the rectum of the patient. The three dark lines around three sides of the device are the output end of the optical fibers that deliver

light into the prostate from three different planes [the red colored planes shown in (B)]. The device is encapsulated with a gray-color PDMS lens (yellow-dotted rectangular box) above the CMUT surface to achieve elevation focusing. (E and F) Images of the front (E) and back (F) sides of the custom-made PCB.

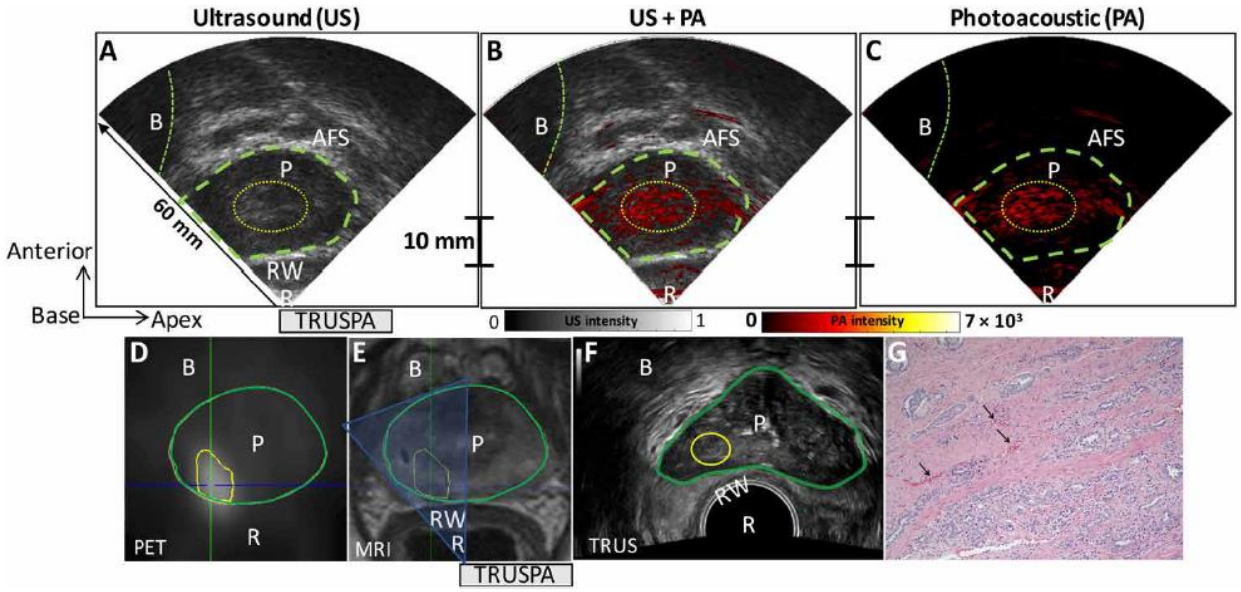

Figure 1.7: In vivo multimodal PET, MRI, TRUSPA imaging of the prostate in a patient with PCa (from Ref. [29]). In all images, the rectum (R), rectal wall (RW), bladder (B), anterior fibromuscular stroma (AFS), and prostate (P; green contour) are labeled. (A to C) Ultrasound (US) in grayscale, PA in red color scale, and co-registered US + PA images of human prostate obtained in vivo with the TRUSPA device. (D) Axial PET imaging showing PCa (yellow contour) using ^{68}Ga-labeled radioactive tracer targeting bombesin receptor on the PCa cells. (E) Axial MRI showing anatomical information of the prostate with yellow contour covering the extent of PCa identified using PET molecular imaging. (F) Axial TRUS image showing targeted region (yellow

contour) for biopsy using the data from both MRI and PET; targeted biopsy confirmed PCa. (G) Final histopathology from the prostatectomy showing areas of hypervascularity (arrows within) the tumor. Scale bar, 10mm.

Thyroid Imaging

Thyroid cancer is over diagnosed and over treated. Ultrasonography, in combination with fine needle aspiration cytology (FNAC) followed by histology, is the primary diagnostic tool for thyroid cancer. Kang et al. evaluated the diagnostic utility of PAI at detecting thyroid microcalcifications at 700 nm laser wavelengths including 36 resected samples in 18 patients [49]. Dogra et al. validated that ex vivo multispectral photoacoustic imaging can be used to differentiate malignant tissue, benign nodules, and normal human thyroid tissue including fifty patients undergoing thyroidectomy [50]. Yang et al. reported an initial clinical study of in vivo human thyroid by a photoacoustic/ultrasound handheld probe [11]. Both healthy and cancerous thyroids were imaged non-invasively and they compared the photoacoustic imaging with color Doppler ultrasound. The results of photoacoustic thyroid imaging could reveal many blood vessels that were not sensitive for Doppler ultrasound. As shown in Figure 1.8, Roll et al. evaluated hybrid multispectral optoacoustic tomography/ultrasound for imaging thyroid disorders, including Graves' disease and thyroid nodules [10]. The functional biomarkers and tissue parameters deoxygenated hemoglobin, oxygenated hemoglobin, total hemoglobin, saturation of hemoglobin, fat content, and water content were analyzed in thyroid lobes affected by Graves' disease, thyroid lobes with healthy tissue, benign thyroid nodule, and malignant thyroid nodules. This pilot study showed the applicability and the potential of hybrid multispectral optoacoustic tomography/ultrasound to semiquantitatively provide tissue characterization and functional parameters in thyroid disorders for improved noninvasive diagnostics of thyroid diseases.

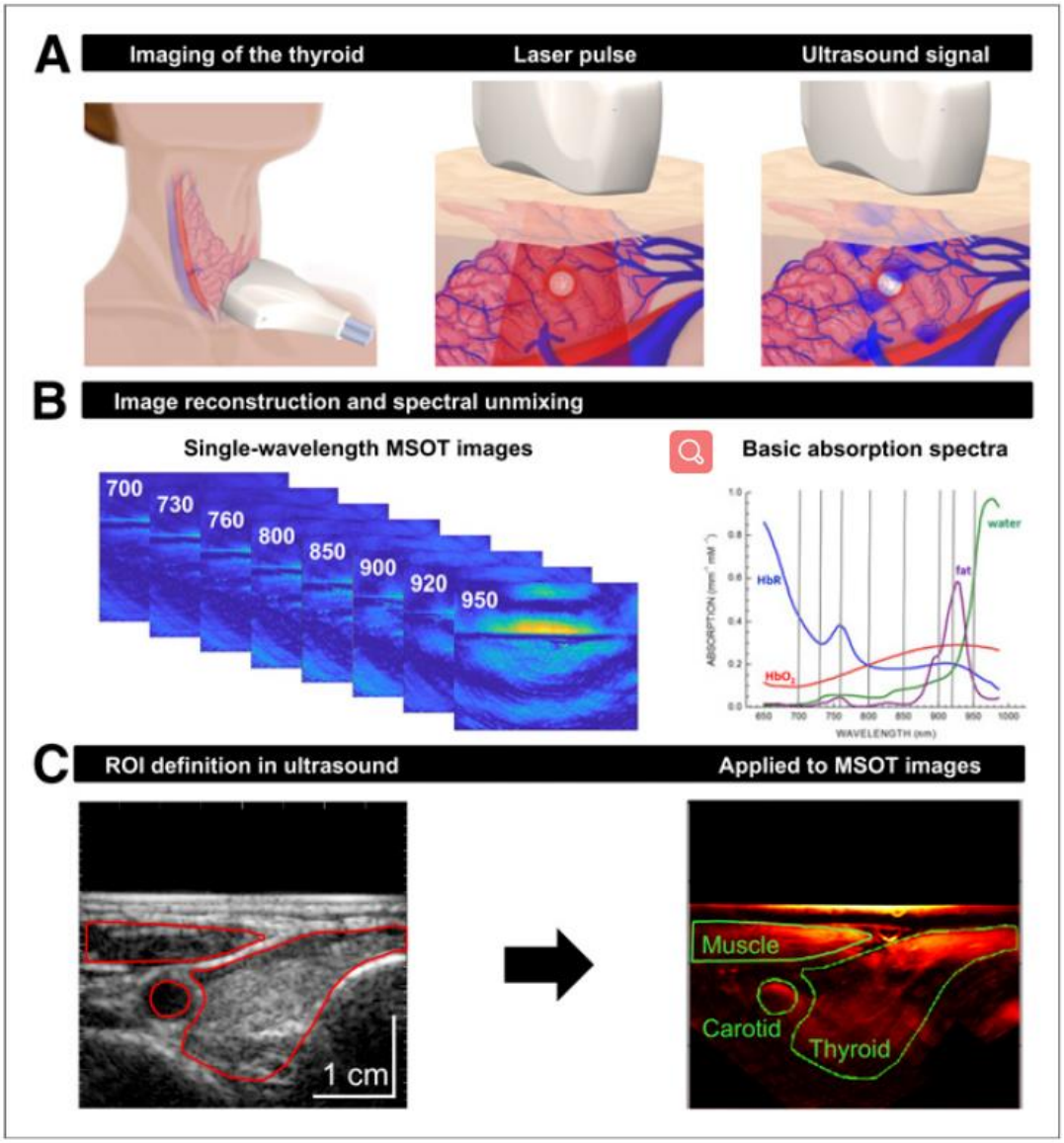

Figure 1.8: Principles of clinical MSOT of thyroid (from Ref. [10]). (A) Scheme of examination of thyroid gland with handheld hybrid MSOT/ultrasound system (left). Patients with thyroid nodules, healthy individuals, and Graves' disease patients were scanned in a reproducible setup. (B) In a first step, MSOT image are acquired for single wavelengths (left). Spectral unmixing, based on specific absorption spectra of different tissue constituents (right), allows assessment of functional parameters such as HbR, HbO_2, fat content, and water content. (C) Transversal ultrasound image of thyroid gland and surrounding tissue allows exact localization of anatomic

structures (left). ROIs drawn on ultrasound images were transferred to coregistered pseudo color-coded averaged MSOT images (here, HbT) for visual and quantitative analysis (right).

Dermatologic Imaging

The human skin, being easily accessible, makes it an ideal location for non-invasive imaging. Attia et al. performed MSOT imaging with two-and three-dimensional handheld scanners on 21 Asian patients with non-malanoma skin cancers (NMSC) [26]. The tumors and their oxygenation parameters could be distinguished from normal skin endogenously. The intraclass correlation coefficient correlating tumor dimension measurements between MSOT and ex vivo histology of excised tumors, showed good correlation. Real-time 3D imaging was found to provide information on lesion morphology and its underlying neovasculature, indicators of the tumor's aggressiveness. As shown in Figure 1.9, Aguirre et al. demonstrated that raster-scan optoacoustic mesoscopy (RSOM) implemented in ultra-broadband (10-180 MHz) detection mode bridges the depth capabilities of ultrasound and the resolution range and high contras of optical methods in clinical dermatology [24]. They visualized skin morphology and vascular patterns in the dermis and sub-dermis of psoriasis patients, enabling quantification of inflammation and other biomarkers of psoriasis without the need for contrast agents. Moreover, Kim et al. performed multispectral ex vivo photoacoustic imaging of cutaneous melanoma for better selection of the excision margin [25].

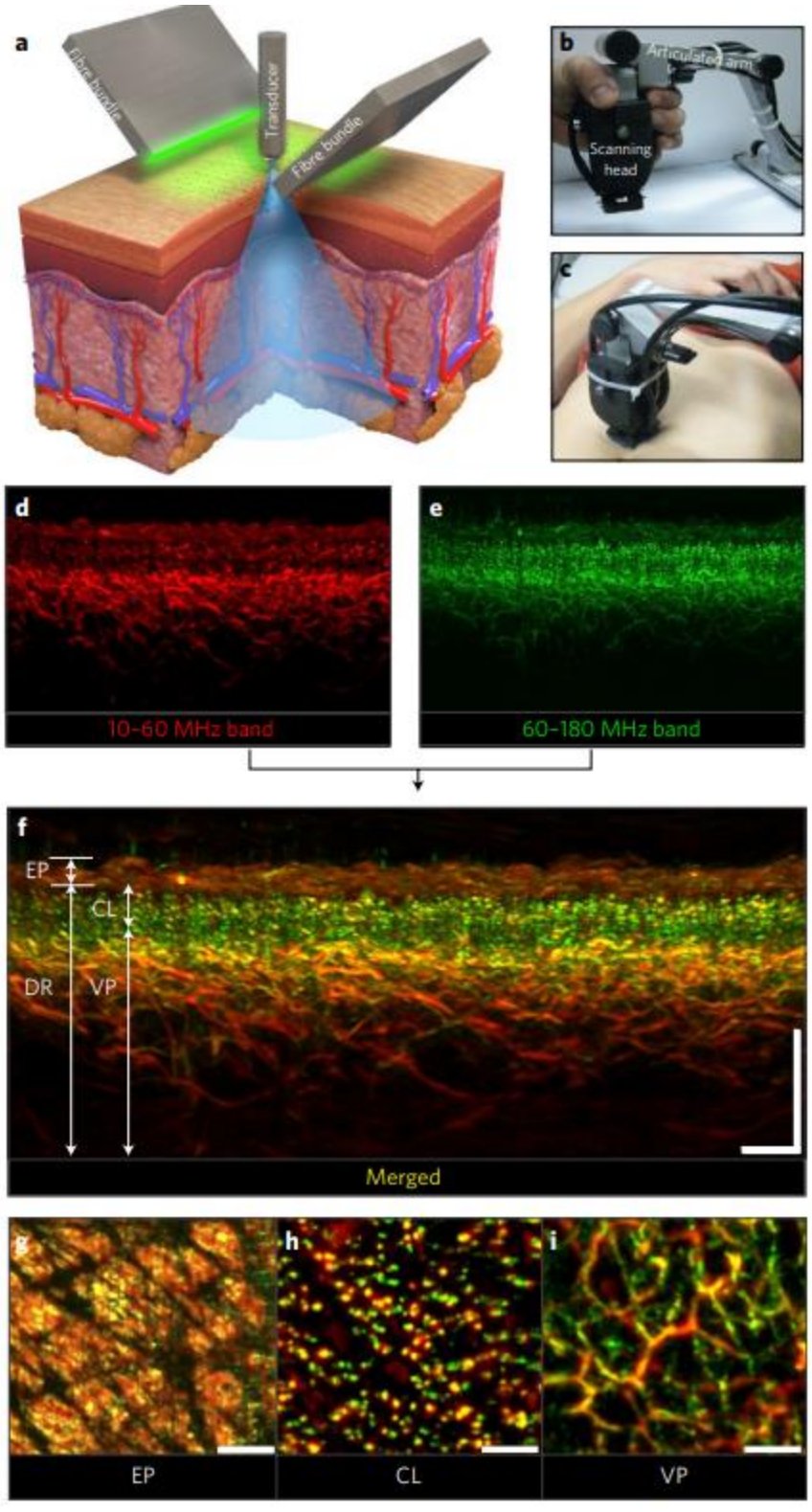

Figure 1.9: Skin imaging with the portable UB-RSOM system, using color coding of frequency bands (from Ref. [24]). a, Schematic of the operation of UB-RSOM. The transducer is raster-scanned parallel to the skin surface, acquiring acoustic signals (A lines) that are generated by laser illumination from two fixed fiber bundles. The focal point of the transducer is kept above the skin surface. b, Photograph of the scanning head and the articulated arm. c, Photograph of the scanning head in position, ready for data acquisition. d,e, The collected optoacoustic signals are filtered in two frequency bands and reconstructed into two images shown in red and green, representing low and high spatial frequencies, respectively. f, UB-RSOM image of healthy skin which combines low and high spatial frequencies in a single color-coded image. g-i, Maximum intensity projections in the coronal direction of the epidermis, showing the indentations of the skin (g), the capillary loop layer (h) and the dermis (i).

1.3 Co-registered Photoacoustic and Ultrasound Tomographic Imaging

Our lab has performed co-registered photoacoustic and ultrasound tomographic imaging on human ovarian cancer for couple of years. Two generations of systems have been developed and applied to ovarian cancer clinical study [30, 14]. Shown in Figure 1.10, the first generation system consisted of a laser source, a fiber-optic light delivery system, a transvaginal US probe, and a real-time PAT/US data acquisition and processing module. The laser source, a tunable Ti: Sapphire laser (LS-2211, Symphotics TII, Camarillo, California) pumped by a Q-swithced Nd: YAG laser (LS-2134, Symphotics TII), delivers 20 ns pulses at 15 Hz repletion rate. In the fiber-optic light delivery system, laser light propagates through a single homemade cylindrical lens array (Edmund

Optics Inc., Barrington, New Jersey). The lenses are arranged with two in front and another two behind, and positioned orthogonally to the pair in front. With the incident laser light centered on the lens array, the beam was splitted into four separate and equal spots [51]. Each beam is coupled into a 1 mm core optical fiber with a numerical aperture of 0. 48. In the transvaginal US probe, four 1 mm core optical fibers are sandwiched between a 3D printed sheath and a 128-element transvaginal US array with a 6 MHz central frequency and 80% bandwidth [52]. In the real-time PAT/US data acquisition and processing module, a unique field-programmable gate array (FPGA) is used to control, acquire, store, delay-and-sum, and transfer data for real-time co-registered imaging [53]. The FPGA controls the ultrasound transmission and ultrasound and photoacoustic data acquisition process of a customized 16-channel module that contains all of the necessary analog and digital circuits.

Figure 1.11, shows images from a clinical study of 25 excised ovaries from 15 patients. Additionally, two patients who had suspicious ovarian masses were imaged in vivo four to eight days before prophylactic oophorectomy. They achieved a sensitivity of 70.4% and specificity of 95.6% using the logistic model whereas as sensitivity of 87.7% and specificity of 97.9% using the SVM. Moreover, for the two in vivo cases, the logistic classifier accurately identified 12 out of 14 imaging frames from a high-grade, early-stage serous epithelial carcinoma, and all 17 images from a benign ovarian mass.

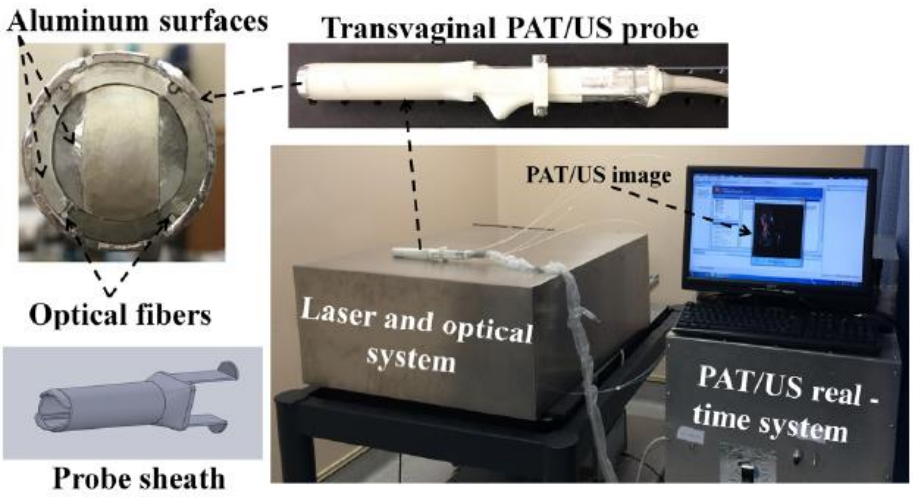

Figure 1.10: The first generation transvaginal coregistered photoacoustic/ultrasound imaging system located at the Radiology Department of the UCONN Health Center for patients' studies (from Ref. [30]).

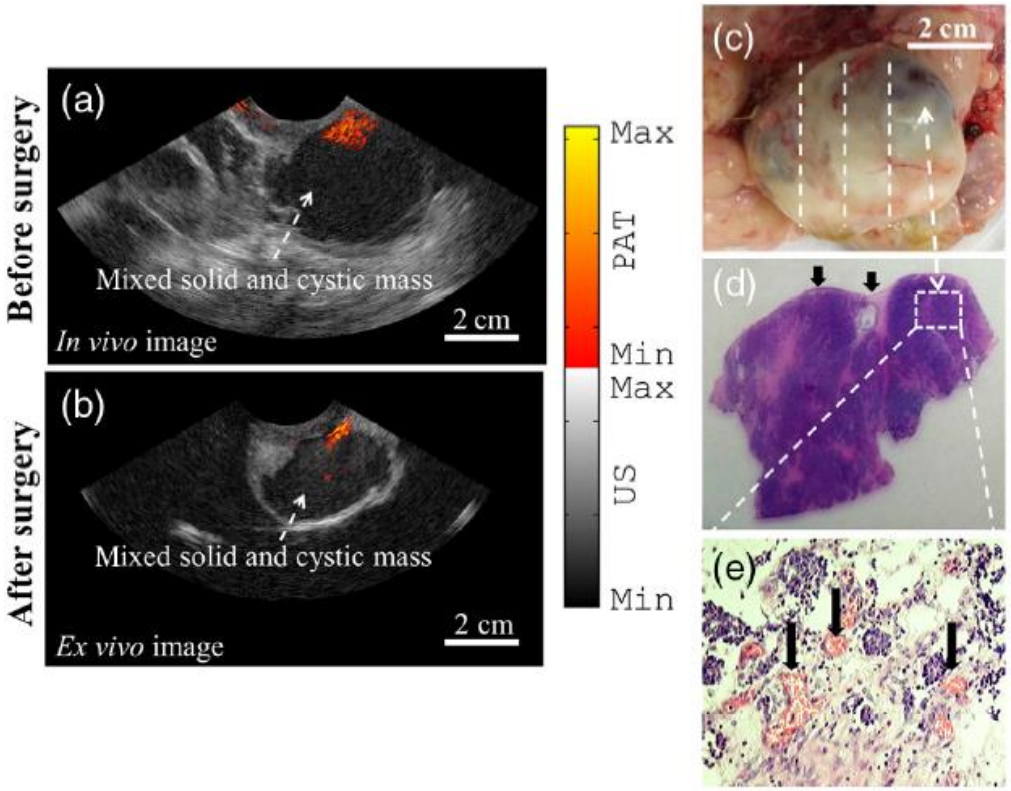

Figure 1.11: (a) In vivo coregistered PAT/US image of a postmenopausal ovarian mass, (b) ex vivo coregistered PAT/US image of the same ovary after oophorectomy, and (c) photograph of the ovary. The dashed lines illustrate the 2-D PAT/US scan positions and the corresponding H&E cuts. (d) H&E staining of the malignant area. The arrows point to the ovary surface. (e) Microvessels from the rectangular region indicated in (d) (from Ref. [30]).

Shown in Figure 1.12, the second generation system has the same laser source, fiber-optic light delivery system, and the transvaginal probe as the first. The only difference is the real-time PAT/US data acquisition and processing module. Instead of using the home-made module, we employed a commercial US system from Alpinion Inc. The Alpinion system provides channel data for both US pulse-echo and photoacoustic imaging, and it can be programmed as a computer terminal for displaying US and photoacoustic images side by side or in co-registered mode.

Using the second generation system, between February 2017 and December 2017, we did another round of in vivo clinical study, including 26 ovarian masses from 16 participants, as shown in Figure 1.13. The average rHbT was 1.9 times higher for invasive epithelial cancers than for the benign/normal ovaries (P = .01). Additionally, the rHbT distribution was extensive in invasive epithelial cancers, but was scattered in benign/normal ovaries. However, the rHbT values of two borderline serous tumors and one stromal tumor were in the same range as that of benign/normal ovaries. The mean sO2 of invasive epithelial cancers, and of the borderline and stromal tumors, was 8.2% lower than that of benign/ normal ovaries (P = .003). Invasive epithelial ovarian cancers showed higher and more extensive tumor vascularity and lower oxygen saturation than benign and normal ovaries. In summary, the coregistered PAT and pulse-echo US was able to distinguish these features and has great potential to improve diagnostic US.

Currently, we are recruiting more patients to participate in a screening and high-risk patient treatment monitoring study at the Washington University School of Medicine.

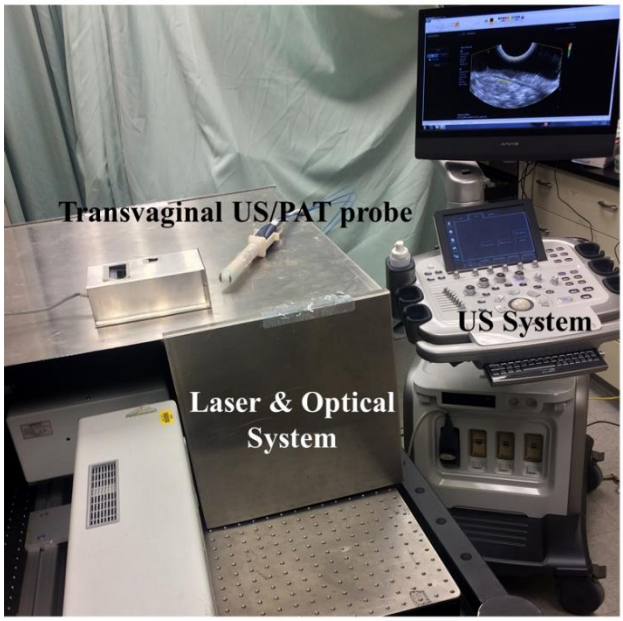

Figure 1.12: Photograph of the photoacoustic tomography (PAT) and pulse-echo US system used for patient study (from Ref. [14]). The laser and optical system was sealed inside a metal cover, with only four fibers coupled to the probe.

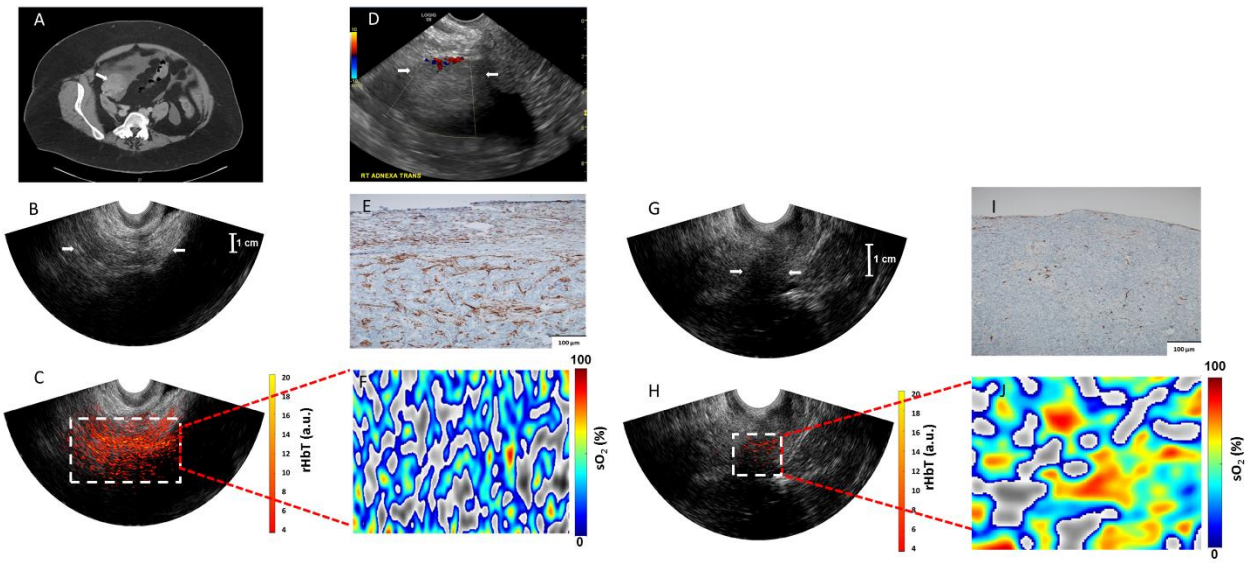

Figure 1.13: Images in a 63-year-old woman after menopause who had a solid right adnexal mass measuring up to 4.5 cm, ascites, and a thickened endometrium at contrast enhanced CT (patient 3) (from Ref. [14]). A. Contrast-enhanced CT image. B. US image (EC-12R; Alpinion Medical Systems) of the right adnexa (arrows). C. The coregistered US and photoacoustic tomography relative total hemoglobin (rHbT) map shown in color, with extensive diffused vascular distribution covering a large area of the region of interest in the depth range of 1-4 cm. D. US Doppler image (Logiq 8S; GE Healthcare) of the right adnexa shows a hypoechoic soft tissue mass with minimal peripheral flow on color Doppler images (arrows). E, CD31 immunostaining in the suture area, showing numerous and extensive micro-vessels; F, Oxygen saturation (sO_2) map of the region of interest marked by the white rectangular box in C with mean sO_2 of 43.2%. G, US image in the left ovary (arrows). H, Coregistered US and photoacoustic tomography rHbT map shows scattered photoacoustic tomography signals. I, CD31 immunostaining of surgical sample. J, sO_2 map of the region of interest identified by coregistered US with measured mean sO_2 of 58.2%. Pathologic examination found a normal ovary with no significant histopathologic abnormalities.

References

1. American Cancer Society, Cancer Facts and Figures, American Cancer Society, Atlanta, GA, 2019.
2. R. L. Siegel et al., “Colorectal cancer statistics, 2017,” CA: a cancer journal for clinicians, 67(3), 177-193 (2017).
3. L. V. Wang, & S. Hu, “Photoacoustic tomography: in vivo imaging from organelles to organs,” Science, 335(6075), 1458-1462, (2012).

4. L. V. Wang, & J. Yao, “A practical guide to photoacoustic tomography in the life sciences,” Nature methods, 13(8), 627, (2016).
5. N. Weidner, J.P. Semple, W.R. Welch, J. Folkman, Tumor angiogenesis and metastasis--correlation in invasive breast carcinoma., N. Engl. J. Med. (1991). doi:10.1056/NEJM199101033240101.
6. P. Vaupel, F. Kallinowski, P. Okunieff, Blood flow, oxygen and nutrient supply, and metabolic microenvironment of human tumors: a review., Cancer Res. (1989). doi:10.1158/0008-5472.can-07-5575.
7. Oraevsky, A. A., Clingman, B., Zalev, J., Stavros, A. T., Yang, W. T., & Parikh, J. R., “Clinical optoacoustic imaging combined with ultrasound for coregistered functional and anatomical mapping of breast tumors,” Photoacoustics, 12, 30-45, (2018).
8. Lin, L., Hu, P., Shi, J., Appleton, C. M., Maslov, K., Li, L., ... & Wang, L. V., “Single-breath-hold photoacoustic computed tomography of the breast,” Nature communications, 9(1), 1-9, (2018).
9. Lin, Li, et al. "High-speed three-dimensional photoacoustic computed tomography for preclinical research and clinical translation." *Nature communications* 12.1 (2021): 1-10.
10. W. Roll, N. A. Markwardt, M. Masthoff, A. Helfen, J. Claussen, M. Eisenblätter, ... & V. Ntziachristos, “Multispectral Optoacoustic Tomography of Benign and Malignant Thyroid Disorders: A Pilot Study,” Journal of Nuclear Medicine, 60(10), 1461-1466, (2019).
11. M. Yang, L. Zhao, X. He, N. Su, C. Zhao, H. Tang, ... & B. Zhang, “Photoacoustic/ultrasound dual imaging of human thyroid cancers: an initial clinical study,” Biomedical optics express, 8(7), 3449-3457, (2017).

12. K. Peng, L. He, B. Wang, & J. Xiao, “Detection of cervical cancer based on photoacoustic imaging—the in-vitro results,” Biomedical optics express, 6(1), 135-143, (2015).
13. G. Yang, E. Amidi, W. C. Chapman, S. Nandy, A. Mostafa, H. Abdelal, ... & Q. Zhu, “Co-registered photoacoustic and ultrasound imaging of human colorectal cancer,” Journal of biomedical optics, 24(12), 121913, (2019).
14. S. Nandy, A. Mostafa, I. S. Hagemann, M. A. Powell, E. Amidi, K. Robinson, ... & Q. Zhu, “Evaluation of ovarian cancer: initial application of coregistered photoacoustic tomography and US,” Radiology, 289(3), 740-747, (2018).
15. E. Amidi, A. Mostafa, S. Nandy, G. Yang, W. Middleton, C. Siegel, & Q. Zhu, “Classification of human ovarian cancer using functional, spectral, and imaging features obtained from in vivo photoacoustic imaging,” Biomedical optics express, 10(5), 2303-2317, (2019).
16. Amidi, E., Yang, G., Uddin, K. S., Luo, H., Middleton, W., Powell, M., ... & Zhu, Q. (2020). Role of blood oxygenation saturation in ovarian cancer diagnosis using multi-spectral photoacoustic tomography. Journal of Biophotonics, e202000368.
17. G. Yang, E. Amidi, & Q. Zhu, “Photoacosutic tomography reconstruction using lag-based delay multiply and sum with a coherence factor improves in vivo ovarian cancer diagnosis,” Biomedical Optics express, 12(4), (2021).
18. C. Liu, M. Xing, B. Cong, C. Qiu, D. He, C. Wang, ... & T. Ma, “In vivo transrectal imaging of canine prostate with a sensitive and compact handheld transrectal array photoacoustic probe for early diagnosis of prostate cancer,” Biomedical optics express, 10(4), 1707-1717, (2019).

19. V. S. Dogra, B. K. Chinni, K. S. Valluru, J. V. Joseph, A. Ghazi, J. L. Yao, ... & N. A. Rao, "Multispectral photoacoustic imaging of prostate cancer: preliminary ex-vivo results," Journal of clinical imaging science, 3, (2013).
20. Y. Wang, Y. Zhan, L. M. Harris, S. Khan, & J. Xia, "A portable three-dimensional photoacoustic tomography system for imaging of chronic foot ulcers," Quantitative imaging in medicine and surgery, 9(5), 799, (2019).
21. J. Jo, G. Xu, M. Cao, A. Marquardt, S. Francis, G. Gandikota, & X. Wang, "A functional study of human inflammatory arthritis using photoacoustic imaging," Scientific reports, 7(1), 1-9, (2017).
22. P. J. van den Berg, K. Daoudi, H. J. B. Moens, & W. Steenbergen, "Feasibility of photoacoustic/ultrasound imaging of synovitis in finger joints using a point-of-care system," Photoacoustics, 8, 8-14, (2017).
23. J. Jo, C. Tian, G. Xu, J. Sarazin, E. Schiopu, G. Gandikota, & X. Wang, "Photoacoustic tomography for human musculoskeletal imaging and inflammatory arthritis detection," Photoacoustics, 12, 82-89, (2018).
24. J. Aguirre, M. Schwarz, N. Garzorz, M. Omar, A. Buehler, K. Eyerich, & V. Ntziachristos, "Precision assessment of label-free psoriasis biomarkers with ultra-broadband optoacoustic mesoscopy," Nature Biomedical Engineering, 1(5), 1-8, (2017).
25. J. Kim, Y. H. Kim, B. Park, H. M. Seo, C. H. Bang, G. S. Park, ... & C. Kim, "Multispectral ex vivo photoacoustic imaging of cutaneous melanoma for better selection of the excision margin," British Journal of Dermatology, 179(3), 780-782, (2018).

26. A. B. E. Attia, S. Y. Chuah, D. Razansky, C. J. H. Ho, P. Malempati, U. S. Dinish, ... & M. W. P. Tan, "Noninvasive real-time characterization of non-melanoma skin cancers with handheld optoacoustic probes," Photoacoustics, 7, 20-26 (2017).
27. L. Nie, X. Cai, K. I. Maslov, A. Garcia-Uribe, M. A. Anastasio, & L. V. Wang, "Photoacoustic tomography through a whole adult human skull with a photon recycler," Journal of biomedical optics, 17(11), 110506, (2012).
28. F. Knieling, C. Neufert, A. Hartmann, J. Claussen, A. Urich, C. Egger, ... & M. J. Waldner, "Multispectral optoacoustic tomography for assessment of Crohn's disease activity," The New England journal of medicine, 376(13), 1292-1294, (2017).
29. S. R. Kothapalli, G. A. Sonn, J. W. Choe, A. Nikoozadeh, A. Bhuyan, K. K. Park, ... & S. S. Gambhir, "Simultaneous transrectal ultrasound and photoacoustic human prostate imaging," Science translational medicine, 11(507), (2019).
30. H. S. Salehi, H. Li, A. Merkulov, P. D. Kumavor, H. Vavadi, M. Sanders, ... & Q. Zhu, "Coregistered photoacoustic and ultrasound imaging and classification of ovarian cancer: ex vivo and in vivo studies," Journal of biomedical optics, 21(4), 046006, (2016).
31. A. A. Oraevsky, A. A. Karabutov, S. V. Solomatin, E. V. Savateeva, V. A. Andreev, Z. Gatalica, ... & R. D. Fleming, (2001, June). Laser optoacoustic imaging of breast cancer in vivo. In Biomedical Optoacoustics II (Vol. 4256, pp. 6-15). International Society for Optics and Photonics.
32. S. Manohar, S. E. Vaartjes, J. C. van Hespen, J. M. Klaase, F. M. van den Engh, W. Steenbergen, & T. G. Van Leeuwen, "Initial results of in vivo non-invasive cancer imaging in the human breast using near-infrared photoacoustics," Optics express, 15(19), 12277-12285, (2007).

33. S. A. Ermilov, T. Khamapirad, A. Conjusteau, M. H. Leonard, R. Lacewell, K. Mehta, ... & A. A Oraevsky, “Laser optoacoustic imaging system for detection of breast cancer,” Journal of biomedical optics, 14(2), 024007, (2009).

34. R. A. Kruger, C. M. Kuzmiak, R. B. Lam, D. R. Reinecke, S. P. Del Rio, & D. Steed, “Dedicated 3D photoacoustic breast imaging,” Medical physics, 40(11), 113301, (2013).

35. T. Kitai, M. Torii, T. Sugie, S. Kanao, Y. Mikami, T. Shiina, & M. Toi, “Photoacoustic mammography: initial clinical results,” Breast Cancer, 21(2), 146-153, (2014).

36. G. Diot, S. Metz, A. Noske, E. Liapis, B. Schroeder, S. V. Ovsepian, ... & V. Ntziachristos, “Multispectral optoacoustic tomography (MSOT) of human breast cancer,” Clinical Cancer Research, 23(22), 6912-6922, (2017).

37. E. I. Neuschler, R. Butler, C. A. Young, L. D. Barke, M. L. Bertrand, M. Böhm-Véle, ... & B. E. Dogan, “A pivotal study of optoacoustic imaging to diagnose benign and malignant breast masses: a new evaluation tool for radiologists,” Radiology, 287(2), 398-412, (2018).

38. X. Wang, Y. Pang, G. Ku, X. Xie, G. Stoica, & L. V. Wang, “Noninvasive laser-induced photoacoustic tomography for structural and functional in vivo imaging of the brain,” Nature biotechnology, 21(7), 803-806, (2003).

39. M. Nasiriavanaki, J. Xia, H. Wan, A. Q. Bauer, J. P. Culver, & L. V. Wang, “High-resolution photoacoustic tomography of resting-state functional connectivity in the mouse brain,” Proceedings of the National Academy of Sciences, 111(1), 21-26, (2014).

40. J. Laufer, E. Zhang, G. Raivich, & P. Beard, “Three-dimensional noninvasive imaging of the vasculature in the mouse brain using a high resolution photoacoustic scanner,” Applied optics, 48(10), D299-D306, (2009).

41. P. Zhang, L. Li, L. Lin, P. Hu, J. Shi, Y. He, ... & L. V. Wang, "High-resolution deep functional imaging of the whole mouse brain by photoacoustic computed tomography in vivo," Journal of biophotonics, 11(1), e201700024, (2018).
42. S. Gottschalk, O. Degtyaruk, B. Mc Larney, J. Rebling, M. A. Hutter, X. L. Deán-Ben, ... & D. Razansky, "Rapid volumetric optoacoustic imaging of neural dynamics across the mouse brain," Nature biomedical engineering, 3(5), 392-401, (2019).
43. X. Wang, D. L. Chamberland, & G. Xi, "Noninvasive reflection mode photoacoustic imaging through infant skull toward imaging of neonatal brains," Journal of neuroscience methods, 168(2), 412-421, (2008).
44. M. J. Waldner, F. Knieling, C. Egger, S. Morscher, J. Claussen, M. Vetter, ... & M. F. Neurath, "Multispectral optoacoustic tomography in Crohn's disease: noninvasive imaging of disease activity." Gastroenterology, 151(2), 238-240, (2016).
45. X. Wang, W. W. Roberts, P. L. Carson, D. P. Wood, & J. B. Fowlkes, "Photoacoustic tomography: a potential new tool for prostate cancer," Biomedical optics express, 1(4), 1117-1126, (2010).
46. M. A. Yaseen, S. A. Ermilov, H. P. F. Brecht, R. Su, A. Conjusteau, M. P. Fronheiser, ... & A. A. Oraevsky, "Optoacoustic imaging of the prostate: development toward image-guided biopsy." Journal of biomedical optics, 15(2), 021310, (2010).
47. R. E. Kumon, C. X. Deng, & X. Wang, "Frequency-domain analysis of photoacoustic imaging data from prostate adenocarcinoma tumors in a murine model," Ultrasound in medicine & biology, 37(5), 834-839, (2011).
48. A. Horiguchi, K. Tsujita, K. Irisawa, T. Kasamatsu, K. Hirota, M. Kawaguchi, ... & M. Ishihara, "A pilot study of photoacoustic imaging system for improved real-time

visualization of neurovascular bundle during radical prostatectomy," The Prostate, 76(3), 307-315, (2016).

49. J. Kang, W. Y. Chung, S. W. Kang, H. J. Kwon, J. Yoo, E. K. Kim, ... & J. Y. Kwak, "Ex vivo estimation of photoacoustic imaging for detecting thyroid microcalcifications," PLoS One, 9(11), e113358, (2014).
50. V. S. Dogra, B. K. Chinni, K. S. Valluru, J. Moalem, E. J. Giampoli, K. Evans, & N. A. Rao, "Preliminary results of ex vivo multispectral photoacoustic imaging in the management of thyroid cancer," American Journal of Roentgenology, 202(6), W552-W558, (2014).
51. H. S. Salehi, T. Wang, P. D. Kumavor, H. Li, & Q. Zhu, "Design of miniaturized illumination for transvaginal co-registered photoacoustic and ultrasound imaging," Biomedical optics express, 5(9), 3074-3079, (2014).
52. H. S. Salehi, P. D. Kumavor, H. Li, U. Alqasemi, T. Wang, C. Xu, & Q. Zhu, "Design of optimal light delivery system for co-registered transvaginal ultrasound and photoacoustic imaging of ovarian tissue," Photoacoustics, 3(3), 114-122, (2015).
53. U. Alqasemi, H. Li, A. Aguirre, & Q. Zhu, "FPGA-based reconfigurable processor for ultrafast interlaced ultrasound and photoacoustic imaging," IEEE transactions on ultrasonics, ferroelectrics, and frequency control, 59(7), 1344-1353, (2012).

Chapter 2: Optimize a light delivery probe, using ball lenses for co-registered photoacoustic and ultrasound endo-cavity subsurface imaging

2.1 Introduction

Adenocarcinoma is a type of cancerous tissue that forms in mucus-secreting glands throughout the body. For example, adenocarcinomas make up around 96% of colorectal cancers, and some cervical cancers (10%) are also adenocarcinomas [1-4]. The depth of invasion for early stage adenocarcinoma is generally around 1 mm to 7 mm. For example, the stromal invasion depth for cervical adenocarcinoma was measured to be 5 mm or less from the base of the epithelium, with a horizontal spread of 7 mm or less by microscopy [5]. Currently, magnetic resonance imaging (MRI) is the best available imaging modality for detecting and surveilling these tumors, however, its resolution is limited, hindering imaging of small malignancies or abnormalities. Computed tomography (CT) and positron emission tomography (PET) are primary modalities for evaluating tumor metastasis, but are limited in their ability to locally stage malignancies [6]. Clearly, a non-invasive imaging technique is needed to provide high tumor contrast at reasonable microscale resolution and clinically relevant depths.

Photoacoustic imaging or tomography (PAI or PAT) is an emerging technique that can provide functional information about biological tissues [7-16]. Optical absorption, the main PAT contrast, is directly related to tumor angiogenesis and tumor hypoxia. Tumor angiogenesis and oxygen consumption are significant indicators for tumor growth, metastasis, and therapeutic response [17-18]. By combining PAT with ultrasound (US), a PAT/US dual-modality imaging system can

simultaneously provide anatomical and functional information about tumors [19-22].Optical fiber based photoacoustic imaging probes have been designed for various applications by several research groups [23-33]. Linear ultrasound transducer array based PAT probes with either a dark-field illumination scheme [29-31] or a bright-field scheme [32-33] have also been investigated. However, the large sizes of the US array and the high loss in the light transmission of the employed fiber bundles [28-33] make these probes unsuitable for endo-cavity PAT/US imaging. Our group has designed several optical fiber-based transvaginal PAT/US imaging probes for ovarian cancer diagnosis [34-35]. In one early study, the probe consisted of 36 fibers, each with a 200 micron core diameter, paired with a custom-made high-power fiber-optic beam splitter assembly that was integrated with a commercial transvaginal ultrasound transducer and housed in a protective shield. However, the custom-made beam splitter was expensive and easily damaged at the splitter junction by the high energy involved. A later design was modified to use four multi-mode optical fibers with 1 mm core diameters. To eliminate potential hotspots and homogenize the light output of the four fibers, the fibers were enclosed in a custom-designed sheath. The sheath was made of acrylonitrile butadiene styrene (ABS), constructed with a 3D printer, and internally lined with an aluminized film with a reflection coefficient of 85%. The sheath gradually tapered towards the exit end of the probe to allow easy penetration into the body cavity and optimize light homogeneity. In this later design, the 8 to 10 mm thick vagina muscle wall functioned as the light diffuser to homogenize the light beam before it reached the ovary. However, the light beam was not optimized for endo-cavity imaging of surface tumors, such as adenocarcinomas.

Commonly used lens components in fiber-optic microprobes include gradient-index (GRIN) lenses [36-37], drum lenses [38], and fiber fused ball lenses [39-40].

In this paper, we report the optimal design, implementation, and evaluation of an optical fiber based transvaginal PAT/US imaging probe for endo-cavity imaging of adenocarcinomas. A ball-shaped lens is glued to each of four fiber tips to homogenize the light illumination on the tissue surface. The light delivery system consists of light coupling optics, a custom-made transducer sheath, and four 1 mm core multi-mode optical fibers, each with a ball-shaped lens glued on its tip. The endo-cavity illumination design was simulated for various numerical apertures (NA), refractive indexes, probe taper angles, and fiber distances from the tip of the probe, and was subsequently validated by experimental measurements.

2.2 Methods and Materials

2.2.1 Experiment Setup and Imaging Probe

Shown in Figure 2.1 (a), the co-registered PAT/US system consists of a Ti:Sapphire (Symphotics TII, LS-2122, Symphotics, Camarillo, California) optically pumped with a Q-switched Nd:YAG laser (Symphotics TII, LS-2134) to deliver pulsed laser light (10 ns pulse duration, 15 Hz pulse repetition rate, 20 mJ/pulse at 750 nm wavelength). Four fibers receive light from the laser through an optimized illumination system [41]. A commercial US system (EC-12R, Alpinion Medical System, Republic of Korea) is used to acquire the corresponding US and PAT data.

To deliver light to the imaged tissue, the imaging probe was constructed based on the optimal parameters obtained from the simulation. Four 1 mm core multi-mode optical fibers (FP1000ERT, 0.50 NA, THORLABS, n = 1.4 in the 700-800 nm wavelength range) were housed in four corresponding slots on the inner surface of the sheath and sandwiched between the sheath and a 128-channel curved trans-vaginal US transducer (central frequency: 6 MHz, 80% bandwidth). A custom-designed 3D printed sheath, shown in Figure 2.1 (b), was made of photopolymer

(RGD525). The inner surface of the sheath and the outer surface of the ultrasound transducer were covered with an aluminized film having a reflection coefficient of 85% at 750 nm wavelength.

Four ball lenses (1.5-mm-diameter, n = 1.517, Edmund Optics, N-BK7) were individually glued (Norland Optical Adhesives, Edmund Optics) to the ends of 1 mm core multi-mode optical fibers, as shown in Figure 2.1 (c).

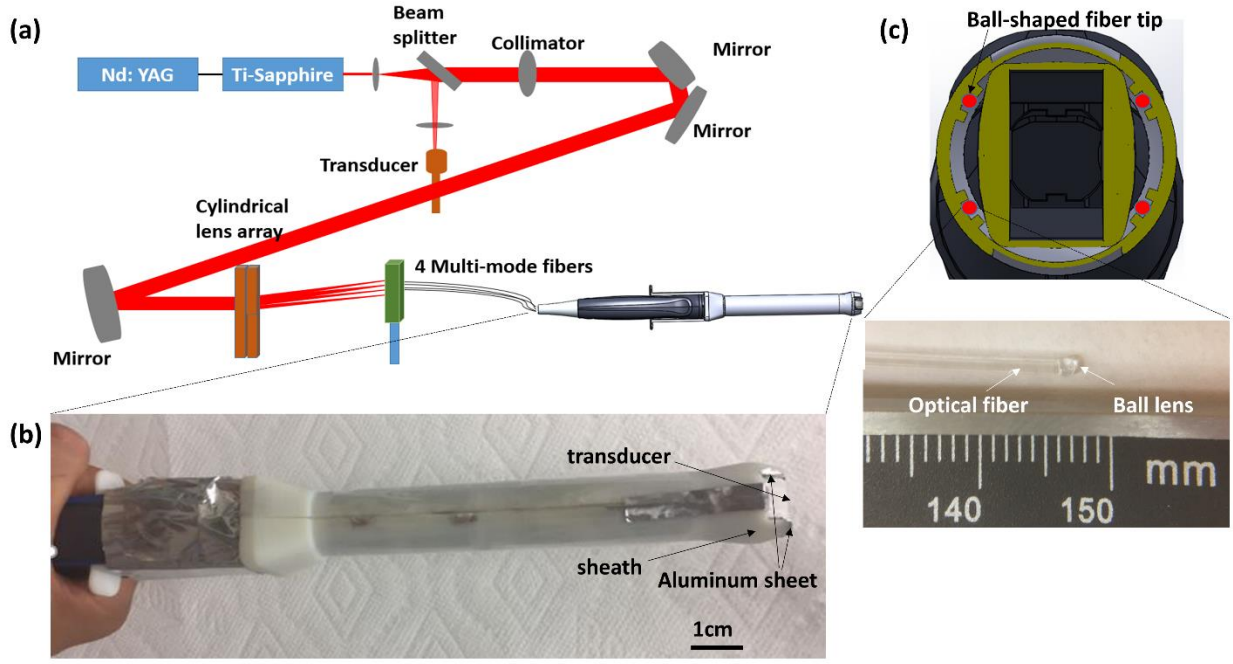

Figure 2.1: (a) Light delivery path of PAT/US system. (b) Zoomed-in view of the imaging probe illustrating co-registered PAT/US transducer with cover sheath and transducer inside sheath. (c) Transducer face with four ball-shaped fiber tips (red color). Insert is the enlarged optical fiber with ball-shaped fiber tip.

2.2.2 Optimization of Imaging Probe Design

Our co-registered US and photoacoustic probe design was optimized to refine its shape and to achieve uniform light homogeneity on the tissue surface, high fluence levels, however, below the

ANSI safety limit (~25 mJ/cm^2 in the 700-800 nm wavelength range) [42], and acceptable power output efficiency. Two sets of simulations were performed as described below.

Using a 3D model in Zemax software, the first set of simulations was performed by measuring the subsurface fluence distribution of the four fibers with and without ball-shaped lenses on the fiber tips. The model of the imaging probe, shown in Figure 2.2, consisted of two concentric hollow cylinders with diameters of 20 mm and 25 mm, which represented the transvaginal US transducer and the probe sheath, respectively. For the inner cylinder, the front face was a convex curvilinear shape with a rectangular cross-section, representing a typical transvaginal or transrectal transducer front face. The light tunnel formed between the inner surface of the outer cylinder and the outer surface of the inner cylinder was assigned a reflection coefficient of 85% at 750 nm, which is the reflection coefficient of typical aluminized film. The power output efficiency is defined as the ratio of the total energy output from the probe to the total energy exiting the four fibers.

A ball-shaped lens on the fiber tip increases fiber's effective NA. The original fiber's NA was 0.5 without a ball lens, and the ball lens of radius 0.75 mm at the fiber tip increased the NA up to 1.2.

The ball-shaped lens also improved the light fluence, this is due to light refocusing at a short distance in front of the ball lens. The position of the focal point for ball-shaped fibers was calculated using paraxial theory [43-45]: $F = R_{ball} * n_{medium}/(n_{ball}-n_{medium}) = 5.33$ mm, where F is the distance of the distal focal point from the surface of the tip (radius of ball tips, R_{ball} =0.75 mm; refractive index, $n_{ball} = 1.517$) in the medium (refractive index, $n_{medium} = 1.33$). The position of the focal point is related to the radius of the sphere, the refractive index of the medium, and the refractive index of the ball lens.

Several parameters of the imaging probe were investigated in order to obtain light illumination homogeneity and acceptable fluence levels, while at the same time yielding higher power output efficiencies. These parameters, some of which are shown in Figure 2.2 include 1) the ball lens refractive index (n); 2) fiber numerical aperture (NA); 3) fiber displacement from the probe tip (L); and 4) sheath taper angle (θ).

The divergence angle of the light exiting the fiber depends on the fiber's NA, which was simulated in Zemax by adjusting the divergence of the light source corresponding to the fiber NA that would give the same divergence. Six different NA, with values of 0.5, 0.7, 0.9, 1.0, 1.1, and 1.2 were simulated.

The focus distance of a ball lens depends on ball lens's diameter, refractive index and the medium refractive index. The converging waist and the diverging angle of the ball lens depend on the ratio between the ball lens diameter and the fiber's diameter [43-45]. The original fiber's NA, refractive index, and diameter were 0.5, 1.4, and 1.0 mm respectively. The ball lens's refractive index was simulated in Zemax by adjusting the material of the lens while keeping the lens diameter fixed at 1.5 mm. Six different refractive indexes, of 1.45, 1.51, 1.6, 1.68, 1.77, and 1.87 were simulated.

The fiber displacement (L) was also varied in Zemax: displacements of 2.5, 5, 7.5 and 10 mm from the probe tip were simulated. For each displacement, the fluence and power output efficiency at the imaging plane were simulated for all the NA values and compared. The simulation results were obtained with the sheath diameter fixed at 25mm and the sheath taper angle at 0^o. The sheath taper angle (θ) was variously set at 0^o, 4^o, 7^o, 11^o, 12^o, 12.5^o, 14^o, 17^o, 21^o, and 24^o. These angles were simulated by fixing the taper height (H) at 8 mm and changing D1 from 9 to 12.5 mm, and were simply calculated from the inverse tangent of the ratio (D-D1)/H (Figure 2.2). The simulation

results were obtained with a beam divergence corresponding to a fiber NA of 1.2 and a displacement of 2.5 mm.

In the second set of simulations, to simulate a muscle wall, the probe was submerged inside a 100 mm deep volume of medium with a reduced scattering coefficient (μ_s') of 4 cm^{-1} and absorption coefficient (μ_a) of 0.02cm^{-1}. The resulting fluences at twelve different depths from 2.5 mm to 30 mm with 2.5 mm interval were compared. Please note that the depths are defined as the distance from the probe base to the detector plane as shown in Figure 2.2.

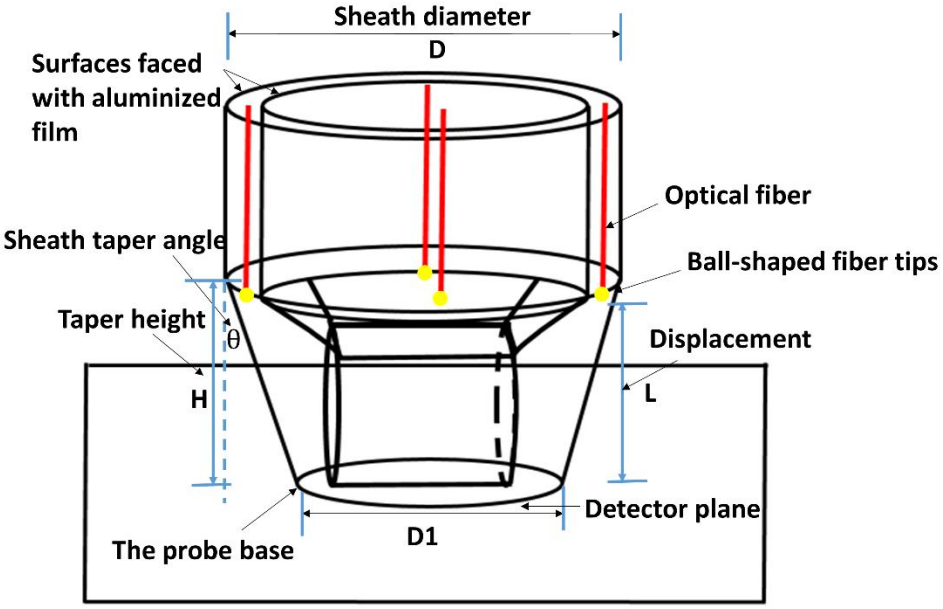

Figure 2.2: Model of the imaging probe employed in the simulation, with all design parameters shown. L, fiber displacement; D, sheath diameter; and θ, sheath taper angle. The detector plane is used in Zemax simulation to observe the light fluence.

2.2.3 Performance Evaluation

In order to validate the system performance [46], we conducted five sets of experiments using the setup shown in Figure 2.3. In the first experiment, we evaluated the light delivery efficiency using fibers with ball tips. The performance of the PAT probe with the original fiber tips and ball-shaped fiber tips was compared by measuring the PAT signals coming from a 400 μm diameter black thread parallel to the imaging plane submerged in a water tank filled with calibrated intralipid solution (Fresenius Kabi, USA). We measured signals at 12 different depths, from 2.5 to 30 mm, at 2.5 mm intervals and 780nm. The intralipid solution had a reduced scattering coefficient (μ_s') of 4 cm^{-1} and an absorption coefficient (μ_a) of 0.02 cm^{-1}. Next, we evaluated the fluence homogeneity using the ball-shaped fiber tips. We captured the laser fluence distributions at 780 nm at four different depths of calibrated intralipid solution (5, 10, 15, 20 mm), using a 12 bit CCD camera (Basler ace, 30 fps, dynamic range 57 dB), and compared the results with those for the original fiber tips. Subsequently, we buried sets of 400 μm black threads parallel to the imaging plane inside chicken breast tissue at five different depths, from 5 to 15 mm at 2.5 mm intervals, and imaged them at 780 nm. For each measurement, after coupling gel was applied, the probe was placed in contact with the chicken breast surface. The performance of the PAT probe with the original fiber tips and ball-shaped fiber tips was compared by measuring the PAT signal strengths from the black threads at each depth. Next, a freshly resected colorectal cancer tissue sample was imaged immediately, after surgical excision from a patient at Washington University School of Medicine. The performance of the PAT probe with the original and ball-shaped fiber tips was compared by measuring the PAT signals at 780 nm, which came from tumor absorption inside the colon sample. Finally, a palmar vein proximal to the human wrist at a depth of around 1-3 mm and parallel to the imaging plane was imaged in a healthy volunteer. The performance of the PAT

probe with the original and ball-shaped fiber tips was compared again by measuring the PAT signals from blood absorption at 780 nm.

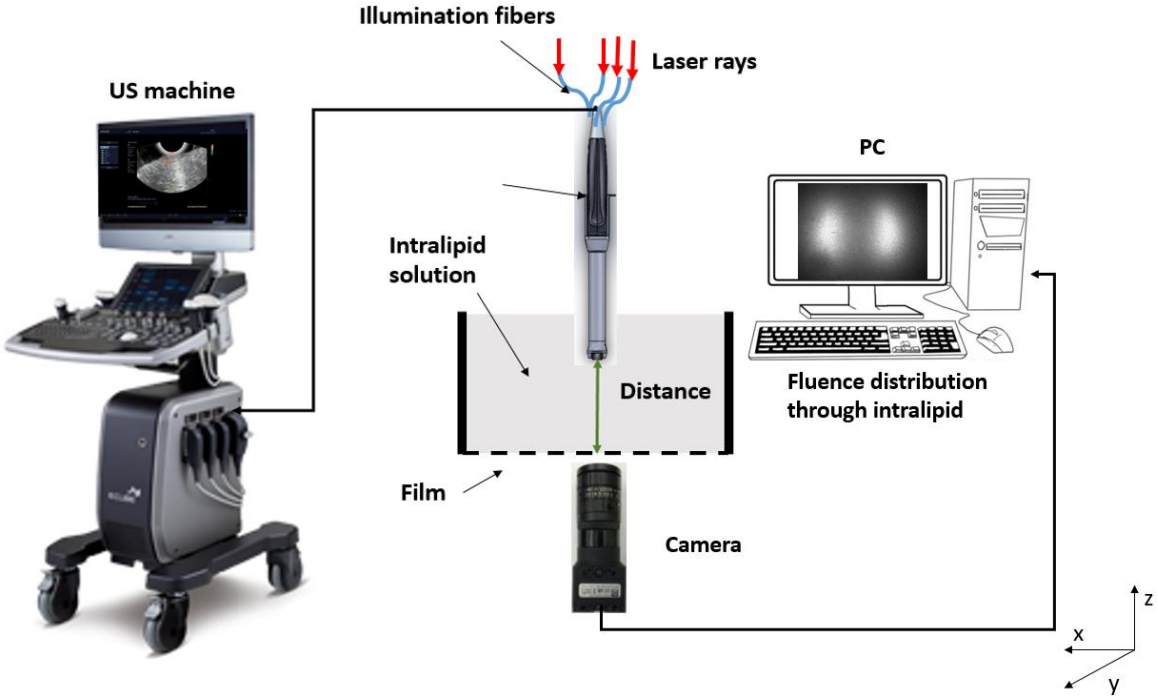

Figure 2.3: The experiment setup for measuring the PAT signal from a black thread inside calibrated intralipid solution and recording the light fluence profile. The US system is shown on the left and the detection camera is underneath the intralipid solution with a film to hold the intralipid. The same set-up is also used for measuring PAT signals with the black thread imbedded inside the chicken breast tissue (not show).

2.3 Results

2.3.1 Simulation Results

Four parameters were sequentially simulated and optimized to test the performance of the endo-cavity illumination design: the fiber's effective NA, the refractive index of the ball lens, the sheath taper angle, and the fiber displacement.

Fiber NA: The effects of using fibers with different NAs on the light fluence are shown in Figure 2.4 (a). As the NA increases, the maximum fluence and power output efficiency decrease, as shown in Figure 2.4 (b). However, increasing the divergence of the light exiting the fiber in turn increases the reflection of photons, resulting in a more diffuse and homogenized beam. For ball-shaped fiber tip, 5 different radii of 0.6, 0.65, 0.75, 0.85, 0.95 mm were investigated. The 2D fluence profile and the corresponding 1D profile taken along the horizontal direction were recorded at the detection plane at 7 mm away from the ball-shaped fiber tip. The full width at half maximum (FWHM) after Gaussian fitting of the corresponding 1D profile was used to calculate the ball-shaped fiber tip's NA. Based on the simulation, we selected an NA of 1.2 for the following ball tip design. Calculations showed that a 0.75 mm radius ball tip optimally increased the 1.0 mm diameter fiber's effective NA, from 0.5 to 1.2 as shown in Figure 2.5.

Ball lens refractive index (n): The effects of using ball lenses with different refractive indexes on the light fluence are shown in Figure 2.6. As the refractive index increases, the light fluence decreases, a consequence of the fiber's refractive index of 1.4. As ball lens' refractive index increases, the mismatch of refractive index between the original fiber and ball lens results in more back scattered light. Based on the simulation, we determined to use n = 1.45-1.52 to be the refractive index range with the highest fluence.

This study is evaluating three major parameters: fluence homogeneity and level on tissue surface, and power output efficiency. For lesions on the surface, the fluence homogeneity is a critical parameter to make sure the illumination pattern is uniform with no hot spots. Based on the simulation, we choose NA=1.2. We then consider trade-off between fluence level, power output efficiency and other probe design parameters. For example, we found other optimal parameters such as refractive index n=1.45-1.52 provided the highest fluence, 2.5 mm displacement provided the highest fluence and output power efficiency. For the taper angle, we choose 12.5 degree for the highest fluence and relatively high power output efficiency because in this condition, fluence and power output efficiency cannot achieve the highest performance simultaneously.

Second set of simulations: In a second set of the simulations, we examined the relationship between the distance of the optical detection plane from the fiber tips and the central area light fluence at the detection plane. Figure 2.7 shows the results for an original fiber tip (NA = 0.5, displacement = 5 mm) and a 0.75 mm radius ball-shaped fiber tip (NA = 1.2, displacement = 2.5 mm). At less than 13 mm distance, the central fluence from the ball tip is much higher than that from the original fiber tip, indicating an increased NA and improved light homogeneity. For distances greater than 13 mm, the fluence at the central imaging area underneath the probe of the original fiber setup is higher than with the ball-shaped fiber setup. With the original fiber, the light beam is homogenized by penetrating through the scattering medium, and the lower NA can decrease light scattering events. However, since more photons are scattered when the distance between the fibers and the detection plane increases, the fluence in the central area decreases for both the ball tip setup and the original fiber setup.

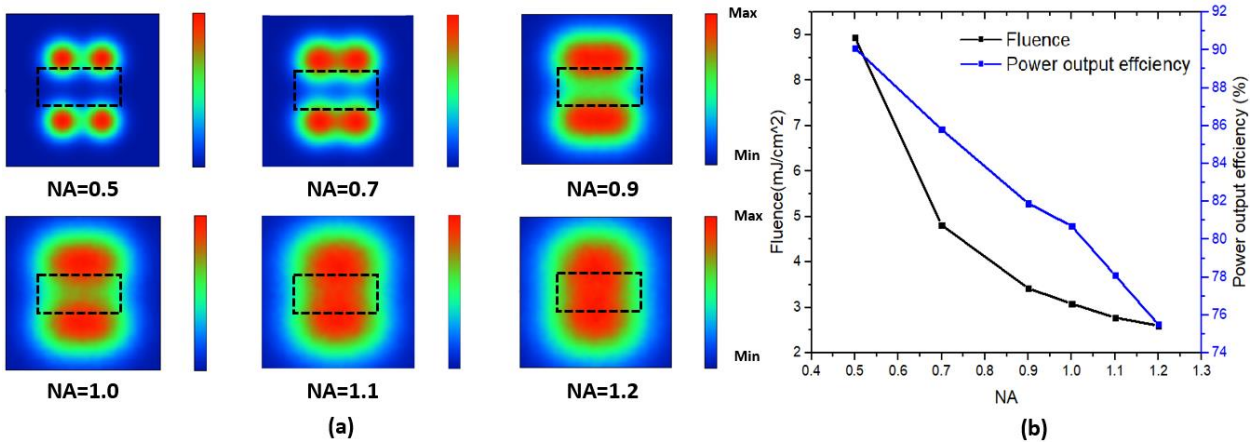

Figure 2.4: Simulated fluence profile corresponding to different fiber NA values. The dashed rectangle represents the cross section of the transducer front surface. (b) The laser fluence and power output efficiency corresponding to fiber NAs of 0.5, 0.7, 0.9, 1.0, 1.1, and 1.2.

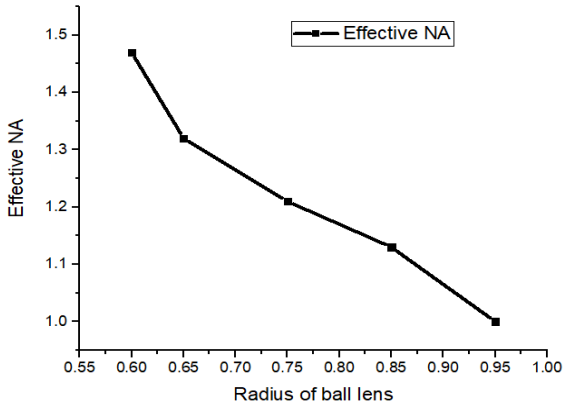

Figure 2.5: The relationship between the radius of ball lens and effective NA.

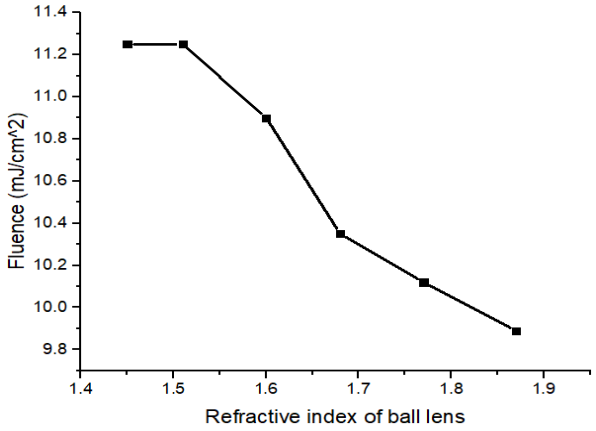

Figure 2.6: The laser fluence corresponding to ball lens refractive index of 1.45, 1.51, 1.6, 1.68, 1.77, and 1.87.

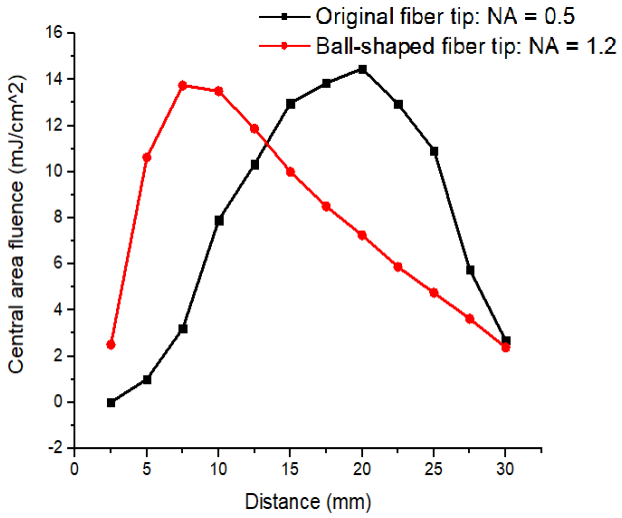

Figure 2.7: Simulated fluence in the central imaging area with the original fiber tip and 0.75 mm radius ball-shaped fiber tip, corresponding to detection plane depths from 2.5 to 30 mm, at 2.5 mm intervals.

2.3.2 Experimental Results

Figure 2.8 shows the PAT signals measured from a 400 μm diameter black thread parallel to the imaging plane at 12 different depths inside a water tank filled with calibrated intralipid solution.

The average peak value of 20 consecutive central beamline envelopes within the region of interest (ROI) was calculated for each distance. For imaging depths shallower than 15 mm, PAT signals from the ball tips are higher than those from the original fiber tips. At depths deeper than 15 mm, the PAT signals from the original fiber tips are higher since the beam is homogenized and the lower NA limits the divergence of the beam and delivers higher fluence. However, as the depth increases, the PAT signals from both tips drops, which is consistent with the previous simulation.

The fluence delivered by the probe after light propagation through 5-20 mm thicknesses of intralipid solution are shown in Figure 2.9 (a). As the thickness increases, the light fluence distribution from ball tips becomes more uniform than that from the original fiber tip setup, especially up to a thickness of 10 mm. In order to quantitatively evaluate uniformity, we use a merging factor ($M = \frac{\text{MaxFluence}-\text{CenterFluence}}{\text{MaxFluence}}$) [34] as shown in Figure 2.9 (b). Compared with the original fiber setup, the ball tips' merging factor is lower for each depth; that is, the beams merge faster and the light fluence distribution becomes more uniform in the photoacoustic imaging. Uniform light illumination over the imaged area is important to obtain an accurate representation of the light absorption map.

The PAT signals coming from a set of 400 μm diameter black threads parallel to the imaging plane and buried inside chicken breast tissue at five different depths are shown in Figure 2.10. The average peak value of 20 consecutive central beamline envelopes within ROI was calculated for each distance. At depths shallower than 11mm, the PAT signals from the ball tips are higher than from the original fiber tips, and at deeper imaging depths, the PAT signals from the original fiber tips are higher. Also, with the increasing depth, the PAT signals in both cases drop, similar to the previous simulation and measurements with the black thread inside intralipid solution. This

behavior implies that within an imaging depth of 10 mm, the PAT probe with ball-shaped fiber tips can achieve a higher light delivery efficiency in the central imaging area underneath the probe.

PAT signals from fresh human colorectal cancer tissue, parallel to the imaging plane at around 3 mm depth, were shown in Figure 2.11. We note here that this study was approved by Institutional Review Committee and the patient signed an informed consent document. The average peak value of 30 consecutive central beamline envelopes within the ROI was calculated. The PAT signals from the ball-shaped fiber design are higher than the original fiber setup within this depth range. Hence the PAT probe with a ball-shaped fiber tip has a better light delivery efficiency in the central imaging area underneath the probe and transducer, maximizing the sensitivity of the design.

PAT signals coming from a palmar vein proximal to a human wrist, parallel to the imaging plane at around 1-3 mm depth, are shown in Figure 2.12. The average peak value of 20 consecutive central beamline envelopes within the ROI was calculated. The PAT signals from the ball tip design are higher than from the original fiber setup within this depth range, which is consistent with the results of the human colon cancer sample.

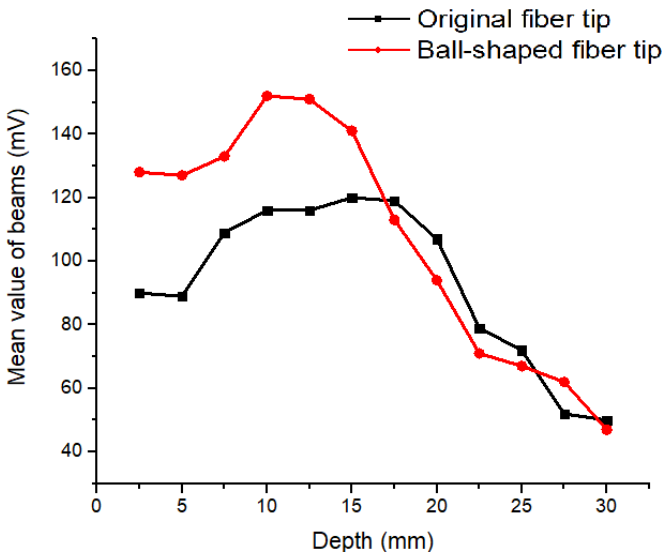

Figure 2.8: The experimental laser output power on a 400 μm black thread inside calibrated intralipid solution with the original fiber tip and a 0.75 mm radius ball-shaped fiber tip. Different depths between the fiber tip and the black thread are shown, from 2.5 to 30 mm, at 2.5 mm intervals.

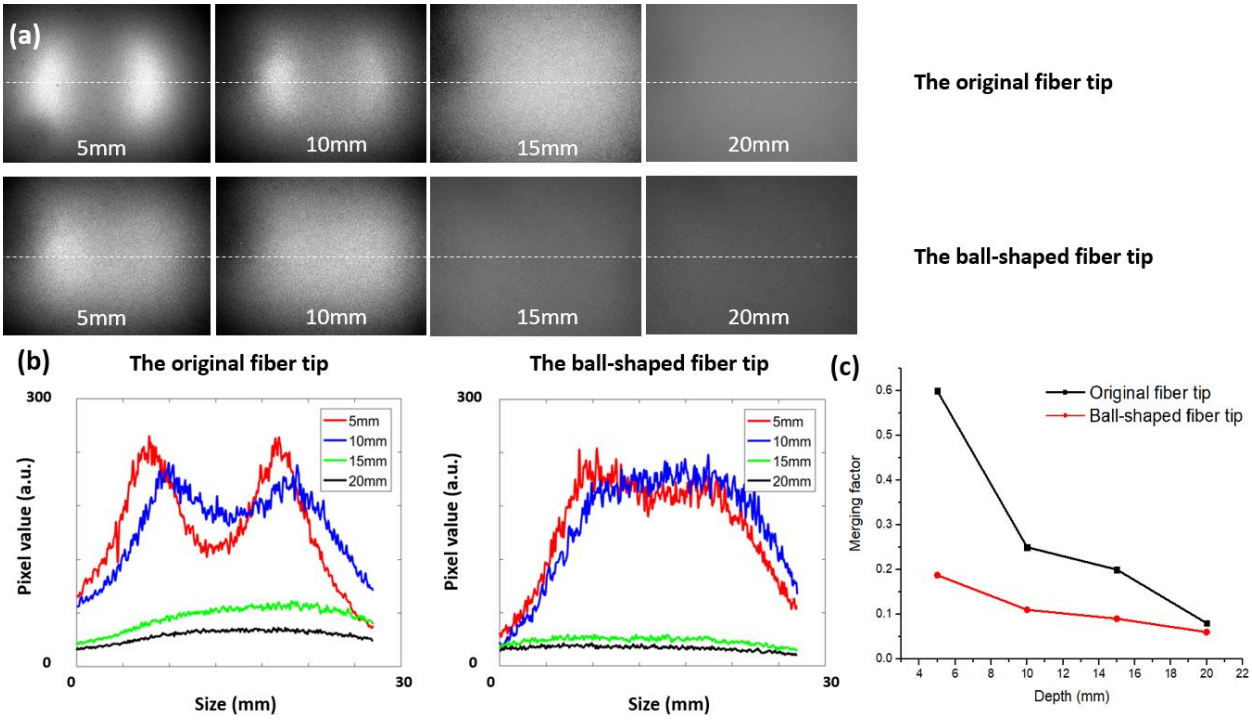

Figure 2.9: Experimental light fluence profiles through calibrated intralipid solution corresponding to different distances. (a) The fluence profile pattern through intralipid solution and (b) the corresponding 1D profile taken along the middle intersection in the horizontal direction at thickness of 5, 10, 15, and 20 mm, and (c) calculated merging factor versus depth.

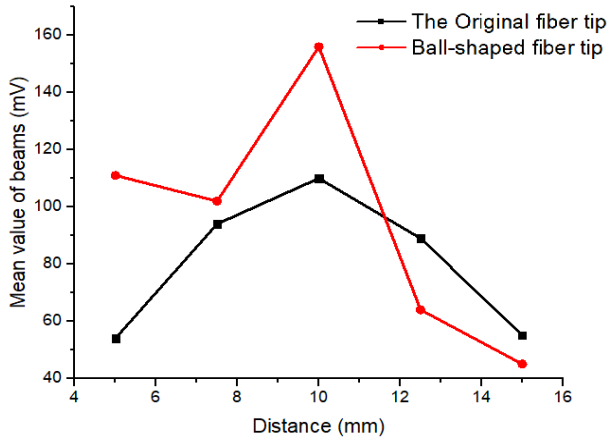

Figure 2.10: The experimental laser output power on a set of five 400 µm diameter black threads buried inside chicken breast tissue at depths of 5, 7.5, 10, 12.5 and 15 mm.

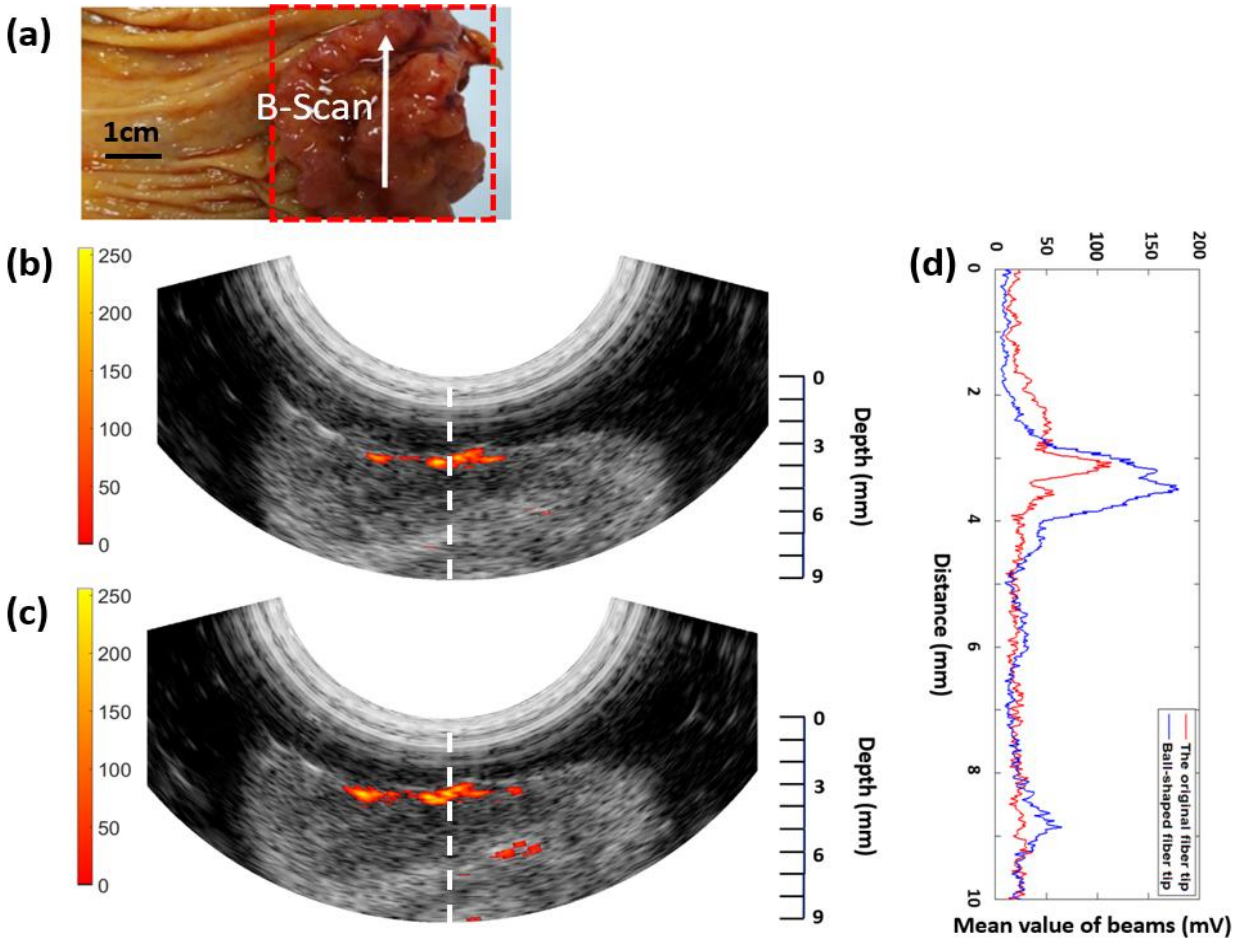

Figure 2.11: Color photograph of fresh human colon cancer tissue: (a) the dashed square box outlines the lesion region and the white arrow indicates the direction along which several B-scans were recorded. (b) *Ex-vivo* photoacoustic imaging of human colorectal cancer with the original fiber tip and (c) the ball-shaped fiber tip. (d) Corresponding PAT signals from the same ROI (white dashed line).

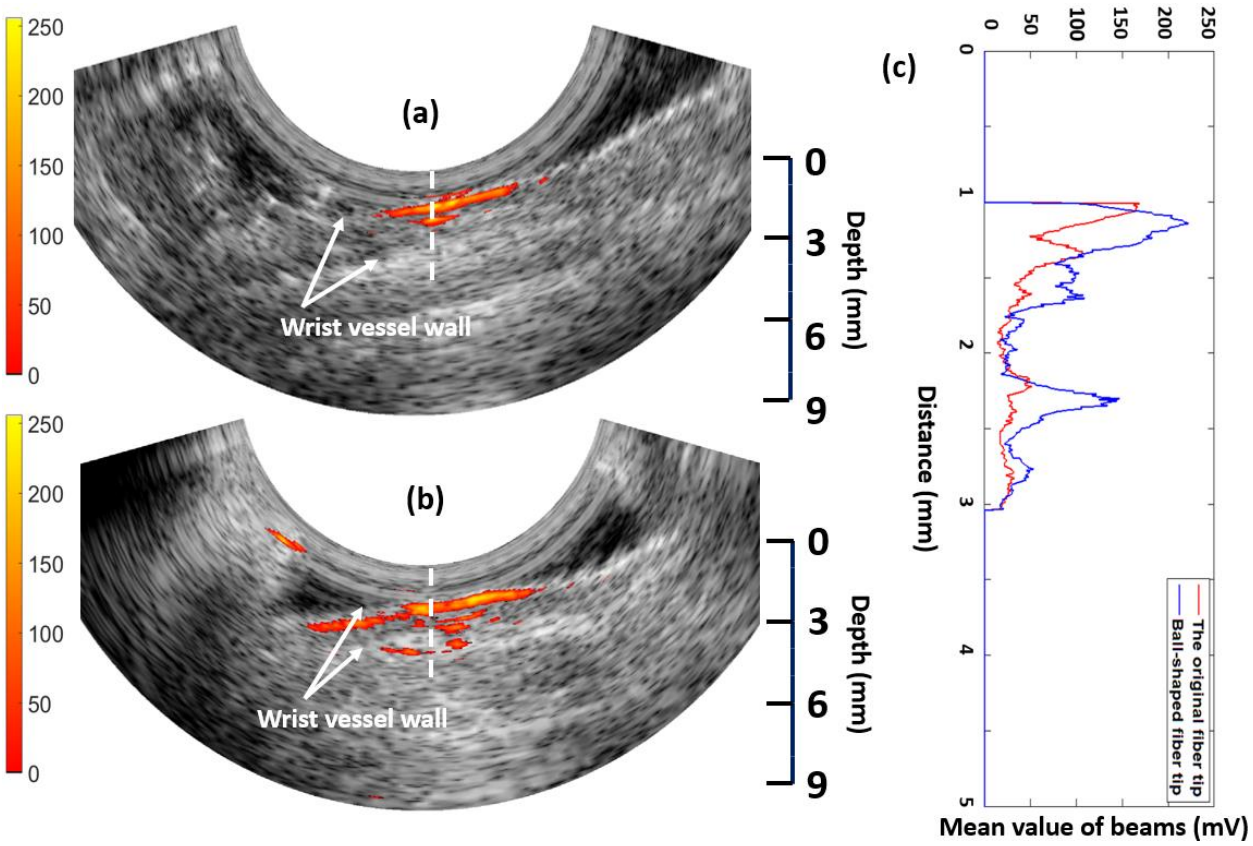

Figure 2.12: *In-vivo* photoacoustic imaging of one palmar vein proximal to the human wrist with (a) the original fiber tip and (b) the ball-shaped fiber tip. (c) Corresponding PAT signals from the same ROI (white dashed line).

2.4 Discussion and Summary

This study is evaluating three major parameters: fluence homogeneity and level on tissue surface, and power output efficiency. For lesions on the surface, the fluence homogeneity is a critical parameter to make sure the illumination pattern is uniform with no hot spots. Based on Fig. 4, we choose NA=1.2. We then consider trade-off between fluence level, power output efficiency and other probe design parameters. For example, we found other optimal parameters such as refractive index n=1.45-1.52 provided the highest fluence, 2.5 mm displacement provided the highest fluence and output power efficiency. For the taper angle, we choose 12.5 degree for the highest fluence and relatively high power output efficiency because in this condition, fluence and power output efficiency cannot achieve the highest performance simultaneously.

The proposed ball-shaped fiber tip design increases the fiber's NA, improving light homogeneity and increasing the light delivery fluence on the central imaging area, although there is a decrease in the maximum light fluence on the entire area. Nevertheless, the increased light homogeneity provides acceptable fluence within the ROI under the MPE for patient safety.

In future studies, fabricating the ball-shaped fiber tip directly from the original fiber end, instead of gluing the ball lens to the fiber ends, can yield a more Gaussian laser beam distribution. Moreover, customized micro fiber diffusers [47] can be explored.

The proposed co-registered photoacoustic and ultrasound probe with ball-shaped fiber tips for optimal light delivery has many clinical applications, especially for cancer diagnosis, staging and treatment assessment of surface tumors of internal organs. For example, colorectal cancers start from neoplastic growth from the inner surface of the colon and can penetrate to deeper layers of the colon at late stages. Cervical cancers arise from the cervix and can grow from the surface of

the cervix into deeper tissues of the cervix. The cancer may also be growing into the body of the uterus. Accurate diagnosis and staging on cancer invasive depth and repeated assessment of cancer treatment response of these surface cancers are current challenges and research opportunities. The utility of the proposed co-registered photoacoustic and ultrasound probe in these applications will be further explored in the near future.

In summary, we have demonstrated a hand-held endo-cavity photoacoustic/ultrasound probe using ball-shaped fiber tips for noninvasive imaging of human adenocarcinoma. The improved light homogeneity and increased fluence on the central imaged area make the designed probe suitable for in vivo noninvasive subsurface tissue imaging.

References

1. B.W. Stewart, C.P. Wild, World cancer report 2014, World Heal. Organ. (2014). doi:9283204298.

2. D. Saslow, D. Solomon, H.W. Lawson, M. Killackey, S.L. Kulasingam, J. Cain, F.A.R. Garcia, A.T. Moriarty, A.G. Waxman, D.C. Wilbur, N. Wentzensen, L.S. Downs, M. Spitzer, A.B. Moscicki, E.L. Franco, M.H. Stoler, M. Schiffman, P.E. Castle, E.R. Myers, American Cancer Society, American Society for Colposcopy and Cervical Pathology, and American Society for Clinical Pathology screening guidelines for the prevention and early detection of cervical cancer, Am. J. Clin. Pathol. (2012). doi:10.1309/AJCPTGD94EVRSJCG.

3. X. Castellsagué, M. Diaz, S. de Sanjosé, N. Muñoz, R. Herrero, S. Franceschi, R.W. Peeling, R. Ashley, J.S. Smith, P.J.F. Snijders, C.J.L.M. Meijer, F.X. Bosch, M. Plummer,

V. Moreno, P. Alonso de Ruiz, S. Chichareon, C. Ngelangel, J. Eluf-Neto, A. Roló, E. Caceres, C. Santos, N. Chaouki, B. El Gueddari, D. Hammouda, T. Rajkumar, Worldwide human papillomavirus etiology of cervical adenocarcinoma and its cofactors: Implications for screening and prevention, J. Natl. Cancer Inst. (2006). doi:10.1093/jnci/djj067.

4. M.J. Mäkinen, Colorectal serrated adenocarcinoma, Histopathology. (2007). doi:10.1111/j.1365-2559.2006.02548.x.

5. N. Colombo, S. Carinelli, A. Colombo, C. Marini, D. Rollo, C. Sessa, Cervical cancer: ESMO clinical practice guidelines for diagnosis, treatment and follow-up, Ann. Oncol. (2012). doi:10.1093/annonc/mds268.

6. S.P. Raman, Y. Chen, E.K. Fishman, Evolution of imaging in rectal cancer: Multimodality imaging with MDCT, MRI, and PET, J. Gastrointest. Oncol. (2015). doi:10.3978/j.issn.2078-6891.2014.108.

7. R.A. Kruger, P. Liu, Y.R. Fang, C.R. Appledorn, Photoacoustic ultrasound (PAUS)—Reconstruction tomography, Med. Phys. (1995). doi:10.1118/1.597429.

8. L. V. Wang, H-I. Wu, Biomedical optics: Principles and imaging, wiley, New York, 2007.

9. L. V. Wang, Prospects of photoacoustic tomography, Med. Phys. (2008). doi:10.1118/1.3013698.

10. X. Wang, Y. Pang, G. Ku, X. Xie, G. Stoica, L. V. Wang, Noninvasive laser-induced photoacoustic tomography for structural and functional in vivo imaging of the brain, Nat. Biotechnol. (2003). doi:10.1038/nbt839.

11. A.A. Oraevsky, A.A. Karabutov, Ultimate sensitivity of time-resolved optoacoustic detection, in: Proc. SPIE, 2000. doi:10.1117/12.386326.

12. B.T. Cox, P.C. Beard, Fast calculation of pulsed photoacoustic fields in fluids using k -space methods, J. Acoust. Soc. Am. (2005). doi:10.1121/1.1920227.

13. A.A. Karabutov, E. V. Savateeva, N.B. Podymova, A.A. Oraevsky, Backward mode detection of laser-induced wide-band ultrasonic transients with optoacoustic transducer, J. Appl. Phys. (2000). doi:10.1063/1.372127.

14. G. Ku, X. Wang, G. Stoica, L. V. Wang, Multiple-bandwidth photoacoustic tomography, Phys. Med. Biol. (2004). doi:10.1088/0031-9155/49/7/018.

15. L. Yin, Q. Wang, Q. Zhang, H. Jiang, Tomographic imaging of absolute optical absorption coefficient in turbid media using combined photoacoustic and diffusing light measurements, Opt. Lett. (2007). doi:10.1364/OL.32.002556.

16. L. Lin, P. Hu, J. Shi, C.M. Appleton, K. Maslov, L. Li, R. Zhang, L. V. Wang, Single-breath-hold photoacoustic computed tomography of the breast, Nat. Commun. (2018). doi:10.1038/s41467-018-04576-z.

17. N. Weidner, J.P. Semple, W.R. Welch, J. Folkman, Tumor angiogenesis and metastasis--correlation in invasive breast carcinoma., N. Engl. J. Med. (1991). doi:10.1056/NEJM199101033240101.

18. P. Vaupel, F. Kallinowski, P. Okunieff, Blood flow, oxygen and nutrient supply, and metabolic microenvironment of human tumors: a review., Cancer Res. (1989). doi:10.1158/0008-5472.can-07-5575.

19. H.S. Salehi, H. Li, A. Merkulov, P.D. Kumavor, H. Vavadi, M. Sanders, A. Kueck, M. a. Brewer, Q. Zhu, Coregistered photoacoustic and ultrasound imaging and classification of ovarian cancer: ex vivo and in vivo studies., J. Biomed. Opt. (2016). doi:10.1117/1.JBO.21.4.046006.

20. T. Wang, Y. Yang, U. Alqasemi, P.D. Kumavor, X. Wang, M. Sanders, M. Brewer, Q. Zhu, Characterization of ovarian tissue based on quantitative analysis of photoacoustic microscopy images, Biomed. Opt. Express. (2013). doi:10.1364/BOE.4.002763.

21. H. Li, P. Kumavor, U. Salman Alqasemi, Q. Zhu, Utilizing spatial and spectral features of photoacoustic imaging for ovarian cancer detection and diagnosis, J. Biomed. Opt. (2015). doi:10.1117/1.JBO.20.1.016002.

22. T. Wang, S. Nandy, H.S. Salehi, P.D. Kumavor, Q. Zhu, A low-cost photoacoustic microscopy system with a laser diode excitation, Biomed. Opt. Express. (2014). doi:10.1364/BOE.5.003053.

23. V. Neuschmelting, N.C. Burton, H. Lockau, A. Urich, S. Harmsen, V. Ntziachristos, M.F. Kircher, Performance of a Multispectral Optoacoustic Tomography (MSOT) System equipped with 2D vs. 3D Handheld Probes for Potential Clinical Translation, Photoacoustics. (2016). doi:10.1016/j.pacs.2015.12.001.

24. L. Song, K. Maslov, K.K. Shung, L. V. Wang, Ultrasound-array-based real-time photoacoustic microscopy of human pulsatile dynamics in vivo, J. Biomed. Opt. (2010). doi:10.1117/1.3333545.

25. J. Hui, Y. Cao, Y. Zhang, A. Kole, P. Wang, G. Yu, G. Eakins, M. Sturek, W. Chen, J.X. Cheng, Real-Time intravascular photoacoustic-ultrasound imaging of lipid-laden plaque in human coronary artery at 16 frames per second, Sci. Rep. (2017). doi:10.1038/s41598-017-01649-9.

26. P. Wang, T. Ma, M.N. Slipchenko, S. Liang, J. Hui, K.K. Shung, S. Roy, M. Sturek, Q. Zhou, Z. Chen, J.X. Cheng, High-speed intravascular photoacoustic imaging of lipid-laden atherosclerotic plaque enabled by a 2-kHz Barium Nitrite Raman Laser, Sci. Rep. (2014). doi:10.1038/srep06889.

27. W. Wei, X. Li, Q. Zhou, K.K. Shung, Z. Chen, Integrated ultrasound and photoacoustic probe for co-registered intravascular imaging, J. Biomed. Opt. (2011). doi:10.1117/1.3631798.

28. G. S. Sangha, N. J. Hale, C. Goergen, Adjustable photoacoustic tomography probe improves light delivery and image quality, Photoacoustics. (2018). doi:10.1016/j.pacs.2018.08.002.

29. C. Kim, T.N. Erpelding, L. Jankovic, L. V. Wang, Performance benchmarks of an array-based hand-held photoacoustic probe adapted from a clinical ultrasound system for non-invasive sentinel lymph node imaging, Philos. Trans. R. Soc. A Math. Phys. Eng. Sci. (2011). doi:10.1098/rsta.2010.0353.

30. C. Kim, T.N. Erpelding, L. Jankovic, M.D. Pashley, L. V. Wang, Deeply penetrating in vivo photoacoustic imaging using a clinical ultrasound array system, Biomed. Opt. Express. (2010). doi:10.1364/BOE.1.000278.

31. B.L. Bungart, L. Lan, P. Wang, R. Li, M.O. Koch, L. Cheng, T.A. Masterson, M. Dundar, J.X. Cheng, Photoacoustic tomography of intact human prostates and vascular texture analysis identify prostate cancer biopsy targets, Photoacoustics. (2018). doi:10.1016/j.pacs.2018.07.006.

32. Y.-J. Lee, E.-J. Jeong, H.-W. Song, C.-G. Ahn, H.W. Noh, J.Y. Sim, D.H. Song, M.Y. Jeon, S. Lee, H. Kim, M. Zhang, B.K. Kim, Photoacoustic imaging probe for detecting lymph nodes and spreading of cancer at various depths, J. Biomed. Opt. (2017). doi:10.1117/1.JBO.22.9.091513.

33. M. Li, C. Liu, X. Gong, R. Zheng, Y. Bai, M. Xing, X. Du, X. Liu, J. Zeng, R. Lin, H. Zhou, S. Wang, G. Lu, W. Zhu, C. Fang, L. Song, Linear array-based real-time photoacoustic imaging system with a compact coaxial excitation handheld probe for noninvasive sentinel lymph node mapping, Biomed. Opt. Express. (2018). doi:10.1364/BOE.9.001408.

34. P.D. Kumavor, U. Alqasemi, B. Tavakoli, H. Li, Y. Yang, X. Sun, E. Warych, Q. Zhu, Co-registered pulse-echo/photoacoustic transvaginal probe for real time imaging of ovarian tissue, J. Biophotonics. (2013). doi:10.1002/jbio.201200163.

35. H.S. Salehi, P.D. Kumavor, H. Li, U. Alqasemi, T. Wang, C. Xu, Q. Zhu, Design of optimal light delivery system for co-registered transvaginal ultrasound and photoacoustic imaging of ovarian tissue, Photoacoustics. (2015). doi:10.1016/j.pacs.2015.08.003.

36. W.A. Benalcazar, W. Jung, S.A. Boppart, Aberration characterization for the optimal design of high-resolution endoscopic optical coherence tomography catheters, Opt. Lett. (2012). doi:10.1364/OL.37.001100.

37. X. Li, T.H. Ko, J.G. Fujimoto, Intraluminal fiber-optic Doppler imaging catheter for structural and functional optical coherence tomography., Opt. Lett. (2001). doi:10.1364/OL.26.001906.

38. Y. Zhu, N.G. Terry, J.T. Woosley, N.J. Shaheen, A. Wax, Design and validation of an angle-resolved low-coherence interferometry fiber probe for in vivo clinical measurements of depth-resolved nuclear morphology, J. Biomed. Opt. (2011). doi:10.1117/1.3520130.

39. V.X.D. Yang, Y.X. Mao, N. Munce, B. Standish, W. Kucharczyk, N.E. Marcon, B.C. Wilson, I.A. Vitkin, Interstitial Doppler optical coherence tomography., Opt. Lett. (2005). doi:10.1158/0008-5472.CAN-08-1128.

40. M. Zhao, Y. Huang, J.U. Kang, Sapphire ball lens-based fiber probe for common-path optical coherence tomography and its applications in corneal and retinal imaging, Opt. Lett. (2012). doi:10.1364/OL.37.004835.

41. H.S. Salehi, T. Wang, P.D. Kumavor, H. Li, Q. Zhu, Design of miniaturized illumination for transvaginal co-registered photoacoustic and ultrasound imaging, Biomed. Opt. Express. (2014). doi:10.1364/BOE.5.003074.

42. L.I.A. Laser Institute of America, ANSI Z136.1: American National Standard for Safe Use of Lasers, SPIE Med. Imaging. (2007). doi:10.1117/12.2043901.

43. D. Royston, R. Waynant, A. Banks, S. Ramee, C. J. White, Optical properties of fiber optic surgical tips, Appl. Opt. (1989). doi:10.1364/AO.28.000799.

44. E. Hecht, A. Zajac, Optics Addison-Wesley, Reading, Mass. (1974).

45. R.M. Verdaasdonk, C. Borst, Ray tracing of optically modified fiber tips. 1: spherical probes, Appl. Opt. (1991). doi:10.1364/AO.30.002159.

46. S. Nandy, A. Mostafa, I.S. Hagemann, M.A. Powell, E. Amidi, K. Robinson, D.G. Mutch, C. Siegel, Q. Zhu, Evaluation of Ovarian Cancer: Initial Application of Coregistered Photoacoustic Tomography and US, Radiology. (2018). doi:10.1016/j.jretconser.2010.09.009.

47. M. Li, B. Lan, W. Liu, J. Xia, J. Yao, Internal-illumination photoacoustic computed tomography, J. Biomed. Opt. (2018). doi:10.1117/1.JBO.23.3.030506.

Chapter 3: Develop a novel fiber end face illumination diffuser for endo-cavity photoacoustic imaging

3.1 Introduction

Capitalizing on developments in laser and ultrasound detection, our earlier studies reported in vivo transvaginal imaging using co-registered ultrasound and photoacoustic tomography (PAT) [1-4]. To deliver light into the PAT imaging probe, the multimode fiber is a typical choice. However, the available fiber diameters and numerical apertures (NAs) are limited, leading to a small divergence angle and a high light fluence hotspot on the tissue surface. If the fiber is directly in contact with tissue, the light fluence can easily exceed the maximum permissible exposure (MPE) (~28 mJ/cm^2 @ 780 nm) [5]. Although several research papers have reported methods to reduce the fluence and hotspot at the skin surface [6-8], energy loss and manufacturing difficulty still remain as significant challenges.

Diffusion is an excellent method to reduce the fluence on the tissue surface, and a fiber diffuser tip is relatively compact and well suited for endoscopic imaging. Several research papers and patents have described fiber diffuser tips of various kinds. For example, Lee et al, [9] described a conical air-pocket fiber tip made by fusing a section of hollow optical fiber using an electric arc-discharge process. The laser beam entering the air-pocket fiber interface is reflected by total internal reflection that changes its direction multiple times, thus generating a larger laser spot or even side illumination. Reference [10] formed cracks on a fiber tip to generate reflections and refractions, thus diffusing light. Reference [11] described a bullet-shaped tip for deflecting and refracting light. However, these kinds of shape/structure-based fiber diffusers are relatively difficult to make in practice, the customized shape and cracks make fiber fragile, and the scattered light distribution and spot size are difficult to control.

Also, researchers have tried to use particles or air bubbles as scattering medium for light diffusing. In reference [12], the author used a spherical shape radiator composed of adhesive and quartz powder, which is manufactured on the bare fiber core to generate a spherical pattern illumination for photodynamic therapy. However, this structure needed a large size scattering sphere compared with fiber dimension for a good spherical pattern scattering effect. Reference [13] described a diffusive tip for phototherapy in surgery made by optical scattering medium enclosed in a light transmissive cap, which is attached to fiber tip, with 2π steradians illumination. However, for photoacoustic imaging, the large diffusing divergence angle in references [12,13] is undesirable, where the back-scattered light could not be injected into tissue effectively and thus utilized for imaging.

To address these problems, we have developed an effective fiber diffuser tip to reduce the fluence on the target tissue surface, while injecting more laser energy and enhancing the photoacoustic signal generated from the tissue.

3.2 Methods and Materials

The fiber diffuser tip, as depicted in Figure 3.1(a), is made of silica microspheres (10 um diameter, refractive index = 1.458) mixed within ultraviolet (UV) adhesive (Norland Optical Adhesive 63, refractive index = 1.56). By simple steering, the mixture can be made. After that, the mixture is set aside or put into a vacuum chamber for degassing till all the air bubbles in the mixture are gone. Before applying the mixture onto fiber tip, the homogeneity of mixture is inspected under microscope.

After adhesive mixture preparation, the fiber end facet is polished, and then it is dipped into the mixture of microspheres and adhesive. A partial sphere tip is thus formed by the surface tension of the adhesive. After curing for several minutes under UV light exposure, the fiber diffuser tip is complete. The thickness and curvature of the diffuser tip surface will influence the diffusive effect slightly.

In our experiment and simulation, the curvature of the surface is considered as partial sphere, the radius of the surface is around 0.55 mm and the thickness of the diffuser tip between fiber end and tip end is around 0.32 mm as marked in Figure 3.1(a). When photons enter the tip scattering region, they undergo Mie scattering caused by the refractive index difference between the microspheres and the surrounding UV adhesive, thus scattering the photons and reducing the output fluence. This diffuser structure is compact, with the same dimension as the fiber diameter, and is easy to manufacture in lab.

Here, the diffusing mixture concentration is calculated as the ratio between the mass of the UV adhesive and the microspheres. For example, a 20:10 diffuser is a mixture of 0.20 grams UV adhesive and 0.10 grams silica microspheres. On the one hand, with a higher concentration of silica microspheres, the photons experience more scattering events, and thus light is more diffused at the output end. On the other hand, when mixing more and more silica microspheres with the UV adhesive, the solution will eventually become saturated as a clump which is hard to apply onto fiber tip. A 20:10 ratio is the highest microsphere concentration we could make before the clumping of microspheres in the UV adhesive.

The measured output cross-sectional patterns of a normal fiber tip and a 20:10 fiber diffuser tip are shown in Figure 3.1 (b) with the same input laser energy. As can be seen, with the diffuser tip, a larger spot is observed, and the laser intensity distribution is more homogenized than with the normal fiber tip output. Figure 3.1 (c) shows the axial output patterns of a normal fiber tip and a 20:10 fiber diffuser tip. The light is diffused fast at the output of 20:10 fiber diffuser tip, while the laser output of the normal fiber tip is more concentrated to the axis with a smaller divergence angle.

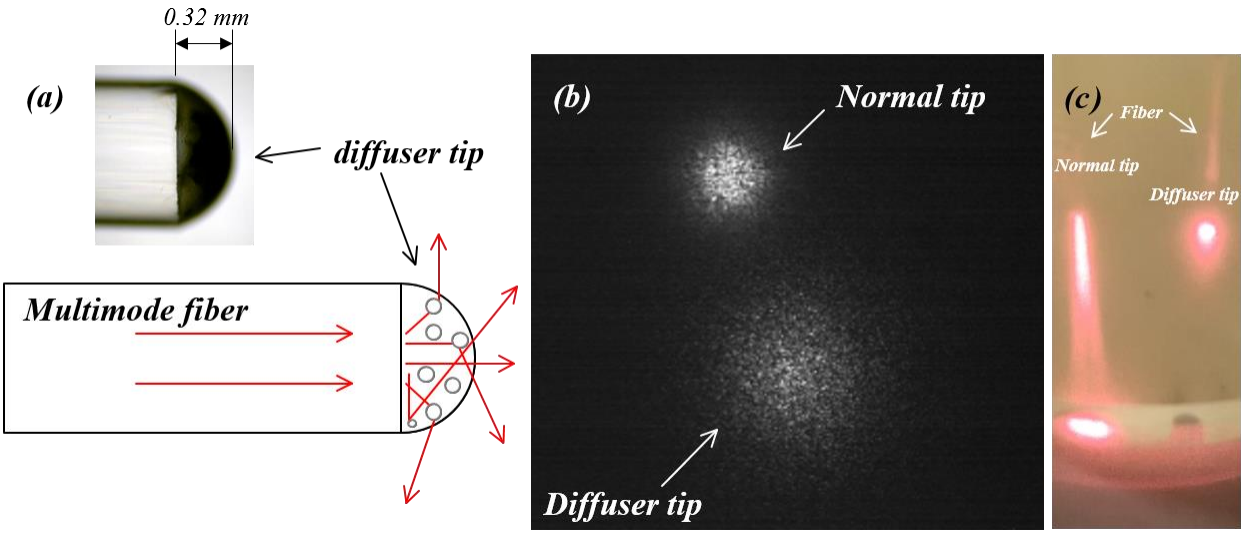

Figure 3.1: (a) Fiber diffuser tip; (b) Fiber tip output cross-sectional pattern recorded by a camera; (c) Fiber tip output axial pattern recorded by a camera.

3.3 Results

Another advantage of this fiber diffuser tip is its controllable scattering effect, with varying microspheres sizes, materials and concentrations. To evaluate the fiber diffuser tip parameters and scattering effect, simulations were performed to examine the influences of the microsphere size and material refractive index, as shown in Figure 3.2 (a) and Figure 3.2 (b). Using Zemax's Mie scattering model, Figure 3.2 (a) shows the output laser patterns in water of different diffuser tips made of different microspheres manufactured on 1 mm core diameter multimode fibers (0.5 N.A., Thorlabs). To determine by simulation the best scattering effect achievable, we examined the maximum 20:10 concentrations of microspheres made of commonly used materials, such as soda-lime glass (n=1.52), methyl methacrylate (PMMA) (n=1.49), and silica (n=1.458).

As expected, different materials and different microsphere sizes had distinct scattering effects. Figure 3.2 (b) depicts the output fluence (blue lines) and energy loss (red lines) of different

materials with varying microsphere diameters in a water medium. The output fluence here is defined as the total energy divided by the cross sectional area at the 1/e points (the points where the fluence has dropped to a value 1/e times the maximum) [5]. The energy loss here is a percentage defined as the back scattered energy (those energy which does not propagate in the forward direction after diffuser tip scattering) over the input energy. With smaller microspheres diameter, the scattering effect is stronger, thus realizing lower output fluence. Meanwhile, energy loss increases with the reduction of microspheres diameter, especially when the diameter is less than 5 *um*. Among all the simulated materials, silica microspheres exhibit the best scattering effects but also have the highest energy loss. By using 10 *um* diameter silica microspheres (grey dash-dotted vertical line), a reasonable scattering effect of 6.5 times fluence reduction with acceptable laser energy loss (< 5%) can be realized.

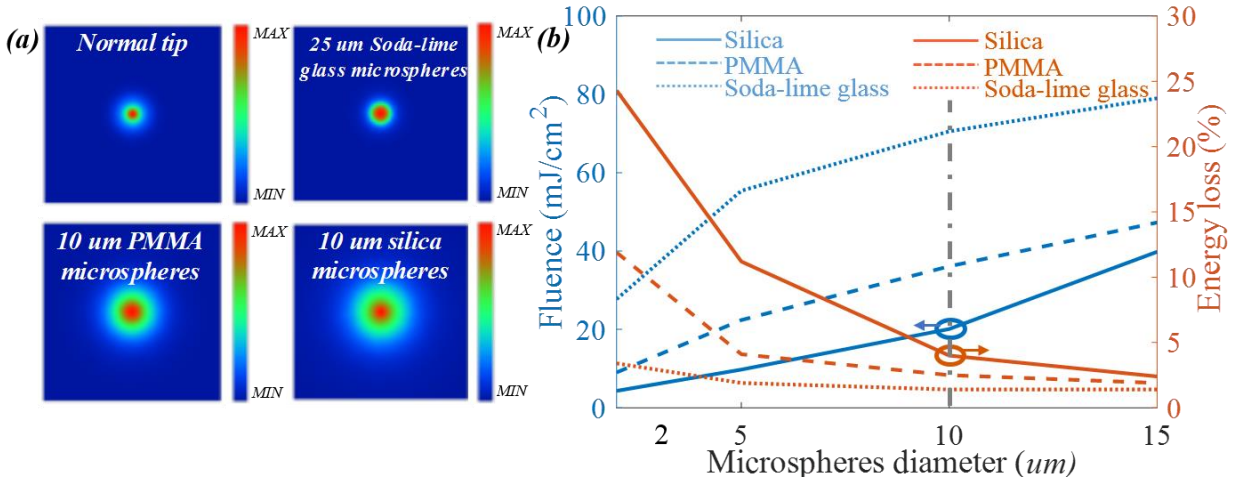

Figure 3.2: (a) Simulation of fiber diffuser tip output pattern: Normal fiber tip (upper-left), soda-lime glass (n = 1.52) (upper-right), PMMA (n = 1.49) (lower-left), silica (n = 1.458) (lower-right); (b) Comparison of fluence and energy loss of different microsphere materials and sizes.

The concentration of silica microspheres is another important parameter, which we studied with both simulations and experiments in water. Figure 3.3 (a) plots fluence (blue lines) and the maximum input laser energy @ MPE (red lines) variations with different fiber diffuser tip microspheres concentrations (from 20:0 to 20:10). At the same input energy level (i.e., 4 *mJ/pulse* in simulation and experiment), the output fluence drops from around 130 mJ/cm^2 for a normal fiber tip to 20 mJ/cm^2 for a 20:10 fiber diffuser tip. On the other hand, with its increased silica microsphere concentration, the maximum input laser energy without exceeding the tissue surface MPE also increases, from 0.9 *mJ/pulse* with a normal fiber tip to 5.7 *mJ/pulse* with a 20:10 fiber diffuser tip. This input energy increase will greatly increase the photoacoustic signal without exceeding the surface MPE due to the diffused laser spot, as will be demonstrated later.

In order to analyze the fiber diffuser tip's light scattering effect within tissue, we conducted simulations and experiments using a calibrated 0.4% intralipid solution with a 4 cm^{-1} reduced scattering coefficient (μ_s') and a 0.02 cm^{-1} absorption coefficient (μ_a).

In the experiments, light scattered quickly in the intralipid solution. To show the average fluence distribution in the intralipid solution, here we defined a parameter, named average energy, as the total detected energy averaged by the entire energy detector sensing area. Based on this definition, a higher average energy corresponds to a higher fluence over the energy detector sensing area. In simulation, the Henyey-Greenstein scattering model in Zemax was applied for simulating biological tissue, and a 25 mm diameter detector area was used to simulate the 25 mm diameter energy detector (Coherent Inc., J-25MB-HE) used in our experiment. Figure 3.3 (b) shows both the simulated and experimental energy distributions at different depths in 0.4% intralipid solution. The performances of a single 20:10 fiber diffuser tip and a normal fiber tip were compared by measuring the fluence propagating through 5-50 *mm* thickness of calibrated intralipid solution.

During the simulation and experiment, both the 20:10 diffuser tip and normal fiber tip were controlled at the MPE input energy at the tissue surface. Both the 20:10 diffuser tip and normal fiber tip showed good agreement between simulation and experiment, with fluence decreasing with increased depth, due to scattering-induced laser spot expansion. And with the lower laser energy input, limited by the MPE, the normal fiber (@ 0.9*mJ/pulse*) shows much weaker average energy at all depths, nearly 1/6 that of the 20:10 diffuser (@ 5.7 *mJ/pulse*).

Figure 3.3 (c) depicts the peak fluence depth distribution along fiber axis when the surface fluence is controlled at the value of MPE. As can be seen in Figure 3.3 (c), with the increase of depth, the fluence of normal fiber and diffuser tip both decrease. However, with normal fiber, the fluence along fiber axis decreases much faster than the circumstance with diffuser tip. As marked with the gray dashed line in Figure 3.3 (c), the peak fluence at 5 cm depth of a diffuser tip is similar to the peak fluence at 3 cm depth of a normal fiber case.

According to the well-established relationship between photoacoustic signal strength and laser fluence [14-16], the initial pressure generated by the photoacoustic effect has a linear relationship with laser fluence and tissue absorption. With a high fluence distribution inside the tissue, a high photoacoustic signal should be generated under the same tissue absorption parameter. Thus, according to Figure 3.3 (b) and (c), a stronger photoacoustic signal is expected using a diffuser with a higher energy input than a normal fiber with limited input energy.

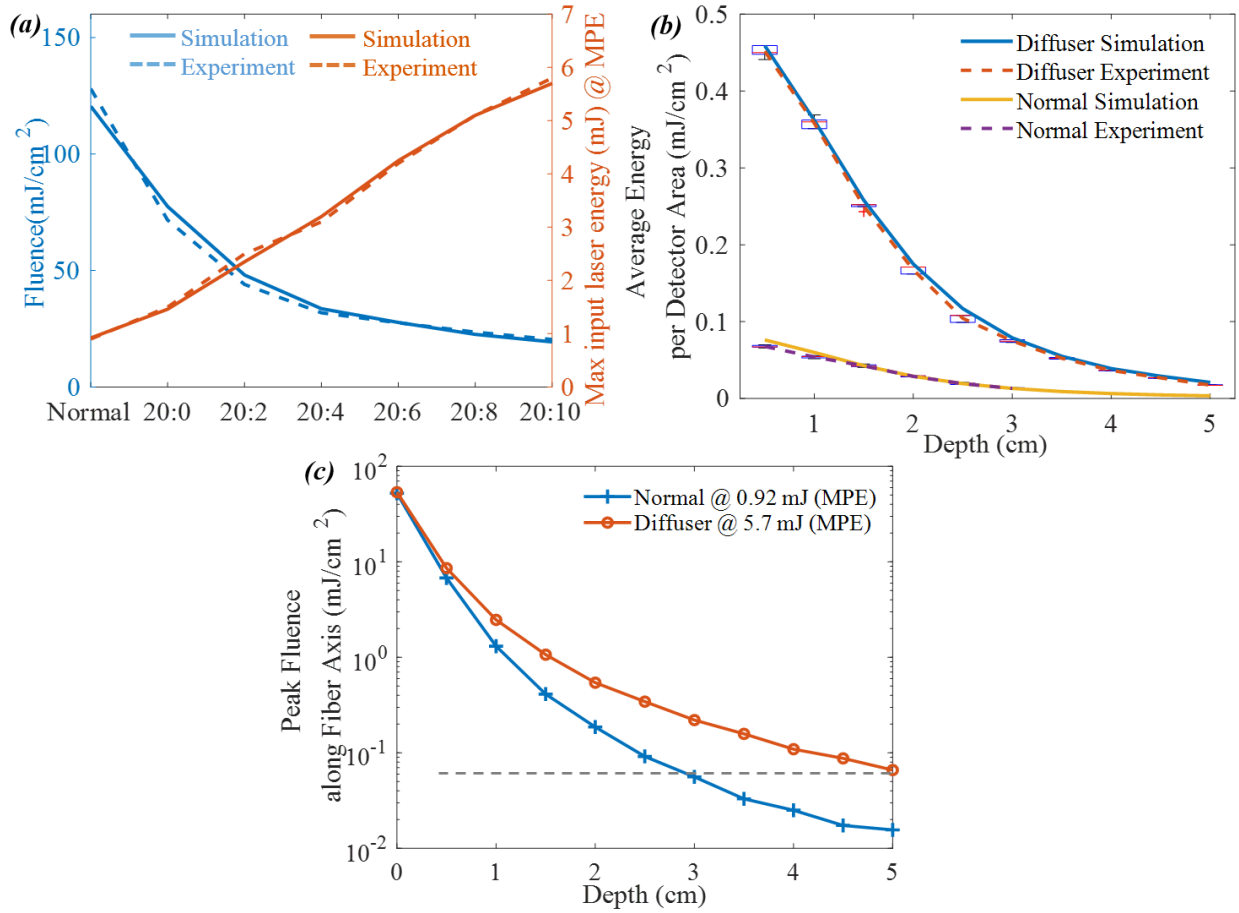

Figure 3.3: (a) Fluence distribution and maximum input energy with different diffuser concentrations; (b) Fluence distribution in calibrated intralipid solution at different depths; (c) Peak fluence along fiber axis at different depths in calibrated intralipid solution.

To demonstrate, we used a 4-fiber transvaginal probe configuration reported in our previous study [7] to perform the experiment and acquire photoacoustic signal in the calibrated 0.4% intralipid emulating biological tissue. A carbon fiber was located in different depths as an imaging target. Also, fluence distribution at different depths was simulated. In this configuration, the horizontal spacing between fibers was 21mm, and the vertical spacing was 12 mm. The ultrasound probe (EC3–10, Alpinion Medical Systems, Republic of Korea) was placed in the center of these four fibers to acquire photoacoustic signal. The fiber tip displacement from the probe base is zero. The

photoacoustic system setup consisted of a fully programmable clinical US system (EC-12R, Alpinion Medical Systems, Republic of Korea), and a Nd:YAG laser (Symphotics-TII, LS-2134, Camarillo, California) pumping a pulsed, tunable (690–900 nm) Ti-sapphire laser (Symphotics TII, LS-2122). Figure 3.4 (a) and (b) show the simulated laser fluence distributions at different depths (5-40 mm) inside the calibrated intralipid solution under surface MPE condition, with (a) the normal fiber and (b) the 20:10 diffuser. Figure 3.4 (c) and (d) depict the normalized fluence distribution along the dashed diagonal line crossing two hotspots in Figure 3.4 (a) and (b), with (c) the normal fiber and (d) the 20:10 diffuser. As can be seen, with the 20:10 diffuser, the four laser spots merged faster than with the normal fiber.

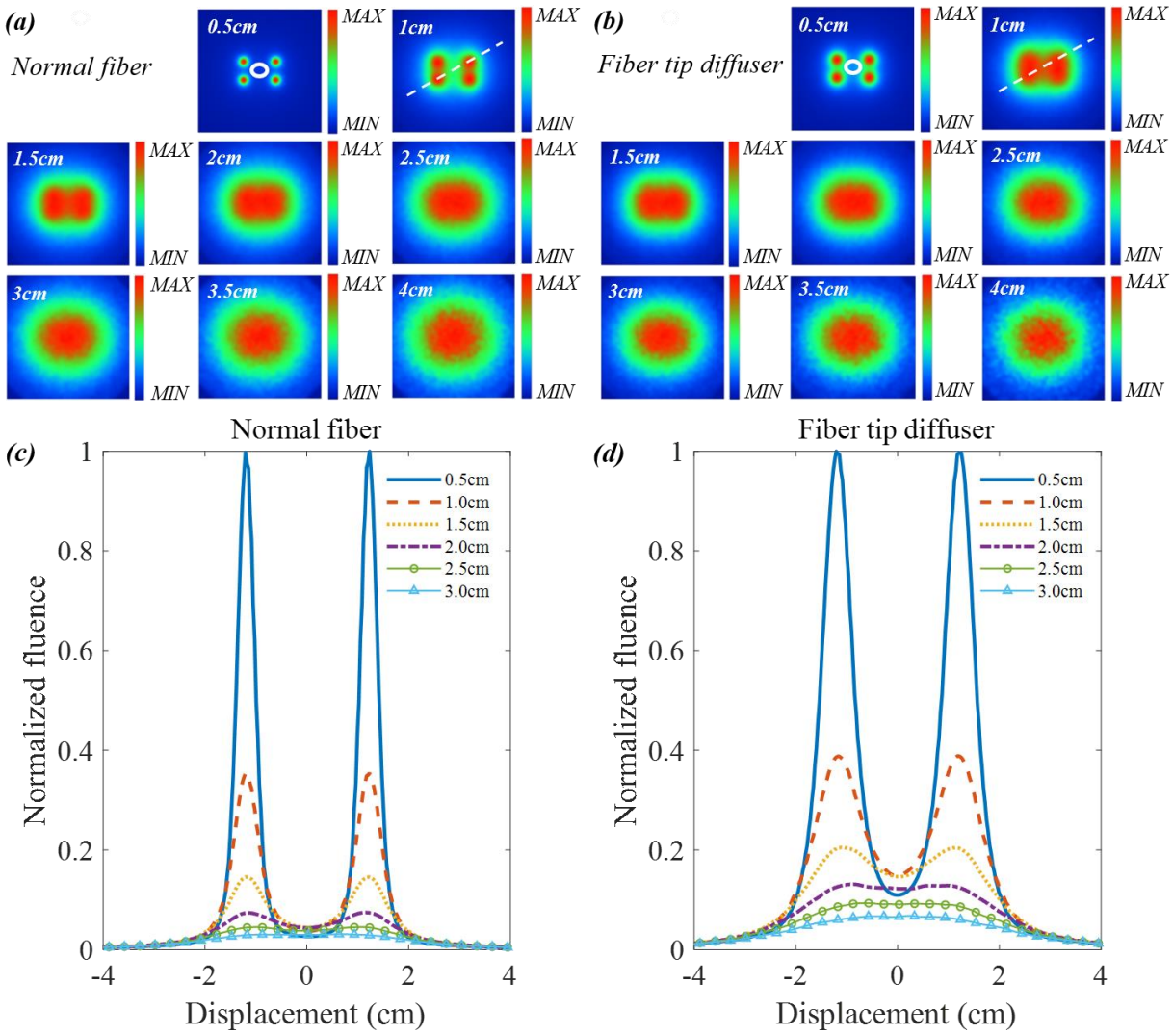

Figure 3.4: (a) Simulation of four-fiber transvaginal probe output fluence in calibrated intralipid solution—normal fiber tip; (b) Four-fiber transvaginal probe output fluence in calibrated intralipid solution—20:10 diffuser tip; (c) Normalized fluence at the diagonal line crossing two hot spots—normal fiber tip; (d) Normalized fluence at the diagonal line crossing two hot spots—20:10 diffuser tip.

Figure 3.5 (a) shows the simulated fluence depth information in 0.4% intralipid solution at the center region of the four fibers, where the imaging target is located, as marked in the white circular

areas in Figure 3.4 (a) and (b). Based on the simulations, the fluence in intralipid first increases and then decreases with increasing depth. For the 20:10 diffuser tip, the fluence peak is around 1 cm -- 1.5 cm. For the normal fiber tip, the peak is at around 1.5 cm -- 2 cm. At 1 cm depth, a 15 *dB* fluence enhancement is observed with the 20:10 diffuser (green line, 5.7 *mJ/pulse*) over that of normal fiber (blue line, 0.9 *mJ/pulse*). On the contrary, with same laser energy input (4 *mJ/pulse*), no big difference is observed in the fluence value distributions of the different diffuser concentrations (purple, orange lines). Figure 3.5 (b) depicts the experimental results of the recorded amplified photoacoustic signal from the commercial ultrasound transducer (EC3–10), we see expected similar trends in the experiments and the simulations.

Figure 3.5 (c) and (d) depict the fluence and photoacoustic signal change with depths in 0.8% calibrated intralipid solution, which has an 8 cm^{-1} reduced scattering coefficient (μ_s') and a 0.02 cm^{-1} absorption coefficient (μ_a). As can be seen, the fluence peak in Figure 3.5 (c) and the photoacoustic signal peak in Figure 3.5 (d) both shifted down to around 1cm depth in 0.8% calibrated intralipid solution, due to increased scattering coefficient. Both 0.4% and 0.8% calibrated intralipid solution experiments show that, with the high concentration 20:10 diffuser tip, more energy can be injected into the tissue without exceeding the tissue surface MPE, while generating a higher photoacoustic signal without damaging the tissue surface. In our experiments, the four-fiber diffuser tips did not reach the MPE energy input level (5.7 mJ/pulse) due to the total energy limitation of our Ti:sapphire laser, which could reach only 4.5 *mJ/pulse* per fiber for four fibers.

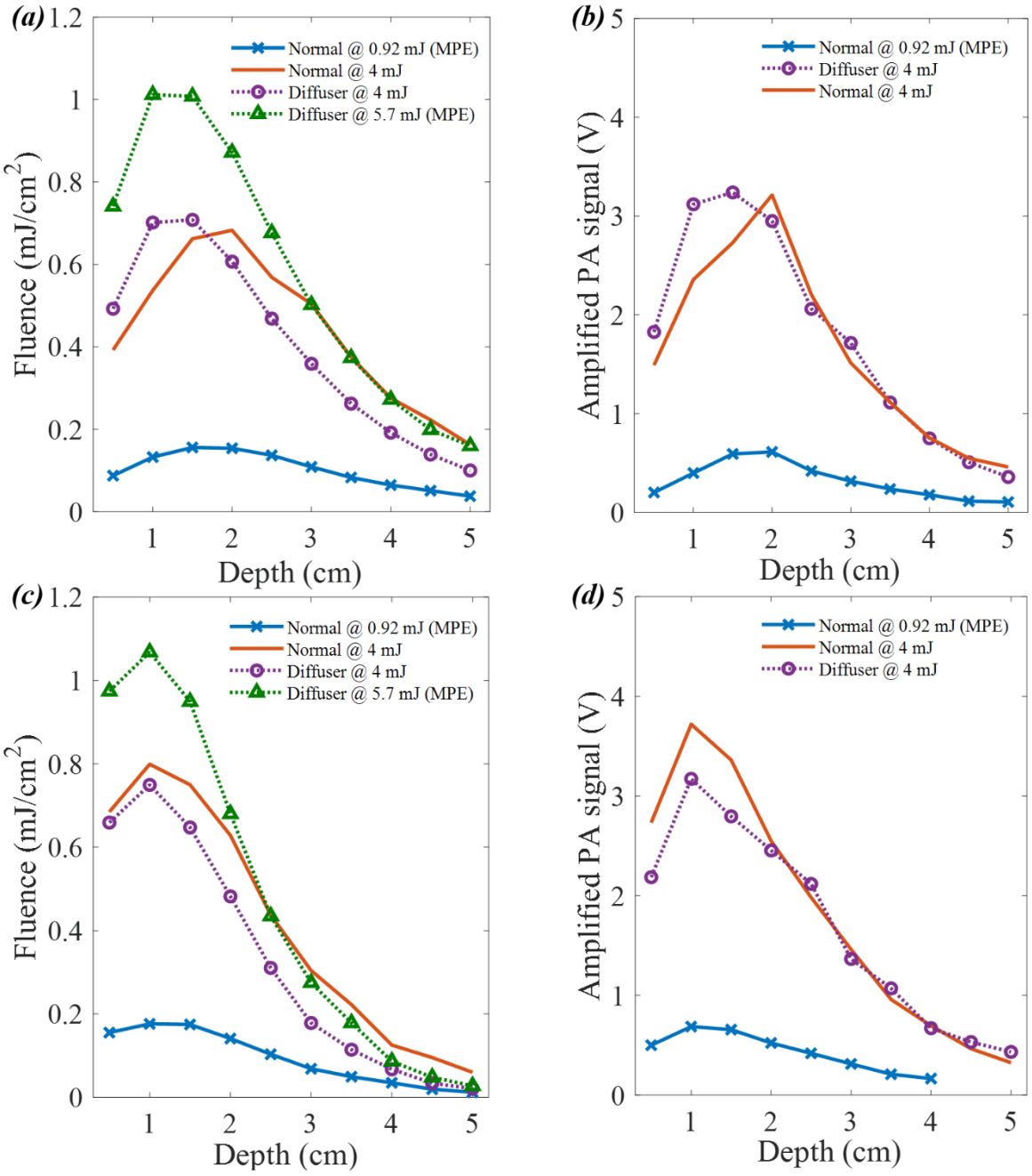

Figure 3.5: (a) Simulation of four-fiber transvaginal probe fluence distribution in 0.4% calibrated intralipid solution at different depths; (b) Experiment photoacoustic signal distribution at different depths in 0.4% calibrated intralipid solution; (c) Simulation of four-fiber transvaginal probe

fluence distribution in 0.8% calibrated intralipid solution at different depths; (d) Experiment photoacoustic signal distribution at different depths in 0.8% calibrated intralipid solution.

3.4 Discussion and Summary

The advantages of this fiber diffuser tip include controllability (different diffusion effects generated by different concentration, material or microsphere size), compactness (same as the dimension of a fiber tip), compatibility (suitable for various fiber tip with different diameters) and high feasibility (easy to make in lab with simple procedures and no requirement for expensive machine). We believe this fiber diffuser tip could be a useful tool for photoacoustic signal enhancement in many endo-cavity photoacoustic imaging applications, such as *in-vivo* colorectal cancer, cervical cancer, and ovarian cancer.

References

1. H. S. Salehi, H. Li, A. Merkulov, P. D. Kumavor, H. Vavadi, M. Sanders, A. Kueck, M. A. Brewer, and Q. Zhu. J. Biomed. Opt. 21, 4, 046006 (2016).

2. S. Nandy, A. Mostafa, I. S. Hagemann, M. A. Powell, E. Amidi, K. Robinson, D. G. Mutch, C. Siegel, and Q. Zhu. Radiology 289, 3 (2018).

3. E. Amidi, A. Mostafa, S. Nandy, G. Yang, W. Middleton, C. Siegel, and Q. Zhu. Biomed. Opt. Express 10, 5 (2019).

4. G. Yang, E. Amidi, W. Chapman Jr, S. Nandy, A. Mostafa, H. Abdelal, Z. Alipour, D. Chatterjee, M. Mutch and Q. Zhu. J. Biomed. Opt. 24, 12, 121913 (2019).

5. American National Standards for the Safe Use of Lasers. ANSI Z136.1 (2014).

6. P. D. Kumavor, U. Alqasemi, B. Tavakoli, H. Li, Y. Yang, X. Sun, E. Warych, and Q. Zhu. J. Biophotonics 6, 6-7 (2013).

7. H. S. Salehi, P. D. Kumavor, H. Li, U. Alqasemi, T. Wang, C. Xu, and Q. Zhu. Photoacoustics 3, 3 (2015).

8. G. Yang, E. Amidi, S. Nandy, A. Mostafa, and Q. Zhu. Photoacoustics 13 (2019).

9. S. H. Lee, Y. T. Ryu, D. H. Son, S. Jeong, Y. Kim, S. Ju, B. H. Kim, and W. T. Han. Opt. Express 23, 16 (2015).

10. J. C. Easley. U.S. Patent 6,829,411 (2004).

11. J. C. Easley. U.S. Patent 5,351,168 (1994).

12. J. S. McCaughan Jr. U.S. Patent 4,693,556 (1987).

13. E. L. Sinofsky, and L. S. Baxter. U.S. Patent 6,071,302 (2000).

14. B. T. Cox, J. G. Laufer, P. C. Beard, and S. R. Arridge. J. Biomed. Opt. 17, 6 (2012).

15. Z. Xu, C. Li, and L. V. Wang. J. Biomed. Opt. 15, 3 (2010).

16. L. V. Wang. IEEE J. Sel. Top. Quantum Electron. 14, 1 (2008).

Chapter 4: Photoacoustic tomography reconstruction using lag-based delay multiply and sum with a coherence factor improves in vivo ovarian cancer diagnosis

4.1 Introduction

Photoacoustic imaging (PAI), also known as optoacoustic imaging (OA), is an emerging biomedical imaging modality that uses the resolution of ultrasound imaging and the contrast of optical imaging to provide structural and functional information [1-2]. PAI has demonstrated its potential for image-based diagnosis in oncology (e.g., breast [3-4], thyroid [5-6], cervical [7], colorectal [8-9], ovarian [10-11], and prostate cancers [12-13]), peripheral vascular diseases (PVDs) [14], joint inflammations [15-17], and skin diseases [18-20].

Ranking fifth among fatal cancers affecting women, ovarian cancer accounts for more deaths than any other cancer of the female reproductive system. According to the American Cancer Society, about 21,750 women received a new diagnosis of ovarian cancer and about 13,940 women died from ovarian cancer in 2020 [21]. Due to the lack of early screening and diagnostic techniques, many women are diagnosed with ovarian cancer when it is already at stages III or IV, where the mortality rates are high (70 to 75%) [22]. Conventional screening tests, including pelvic examination [23, 24], transvaginal ultrasound (TVUS) [25, 26], and blood testing for cancer antigen 125 (CA-125) [26, 27], lack sufficient specificity for early ovarian cancer diagnosis [27]. Imaging modalities such as computed tomography (CT), positron emission tomography (PET), and magnetic resonance imaging (MRI) have been used for surgical guidance. However, all of these modalities have limitations in detecting small lesions. In previous work, to address this

limitation, we developed a co-registered photoacoustic and TVUS technique to improve ovarian cancer diagnosis [10, 11].

Currently, clinical applications of photoacoustic (PA) or ultrasound (US) imaging most commonly use the delay and sum (DAS) beamforming algorithm. This algorithm simply sums the properly delayed and weighted PA/US signal from each channel according to the distances between the focal points and the detectors. However, it has the drawbacks of low resolution and high side lobes, resulting in poor reconstructed image quality. Lim et al. first introduced the delay-multiply-and-sum (DMAS) image reconstruction algorithm for confocal microwave imaging used for breast cancer detection [28]. Subsequently, Matrone et al. proposed an improved version of DMAS to overcome the limitations of DAS in US imaging [29]. Because DMAS improves the coherence of detected channel data, it provides enhanced image quality, with narrower main lobes, and lower side lobes than DAS. These advantages have led several researchers to adopt DMAS in PA imaging and to propose new approaches combining DMAS with other methods. Park et al. combined DMAS with synthetic aperture focusing and applied it to PA microscopy [30]. Alshaya et al. applied DMAS to PA imaging, employing a linear array transducer and introducing a subgroup DMAS method to improve the SNR and processing speed [31]. Matrone et al. combined filtered DMAS (F-DMAS) with multi-line transmission to achieve high frame-rate and high resolution [32]. Mozaffarzadeh et al. combined the minimum variance (MV) beamforming algorithm with DMAS [33]. The MV adaptive beamformer [34] can dynamically calculate the signal weights of the received signals instead of using a fixed apodization function. However, it is very computationally demanding.

While all the above approaches are based on the single-stage DMAS method, Mozaffarzadeh et al. [35] proposed a double-stage DMAS (DS-DMAS) beamforming algorithm. They literally

divided the process of beamforming into two stages. First, the signals are processed by DMAS, that is, the right side of the DMAS equation is expanded to the summations of the separate terms, and these summations are treated as several new synthesized signals. Second, the new synthesized signals are processed by the F-DMAS beamformer again to generate the final output. Same as DMAS, DS-DMAS further improves the image resolution and reduces the side lobes, and is less sensitive than DMAS to high noise levels at deeper depths. Since the DS-DMAS approach was proposed, it has been adopted in photoacoustic imaging [36-38]. Very recently, Song et al. proposed a modified version of DS-DMAS for ultrasound imaging [39]. In the first phase of DMAS beamforming, they combined pairs of signals with the same spatial lag into a new signal. Then they processed the new signal with F-DMAS beamforming to produce the final output. They showed that combining the autocorrelation signals with the DMAS, the image quality of DS-DMAS is slightly improved as compared with the DS-DMAS.

Several groups have proposed a nonlinear beamformer based on p-th root compression (NL-p-DAS) and applied it to PA and US imaging [40-42]. The results have showed that compared with DAS, and DMAS, the NL-p-DAS (p>2) leads to lower side lobes. However, different than DMAS family of algorithms which is based on autocorrelation approach to improve PA and US signal coherence, the p-th root compression may compress both signal and artifacts depending on the relative strengths of the two parts. The p-th power applied to the coherent beam sum may or may not compensate the signal loss depending on the constructive and destructive interferences. Thus, the optimal choice of p-th root is tricky and highly depends on the imaging medium. Recently, Cho el al. modified the NL-p-DAS technique and performed p-th root operation on the spectral domain data (NL-p-SMS) instead of the temporal domain data, which could reduce the grainy

speckles and frequency distortion caused by p-th root in temporal domain data, and dark area artifacts [43]. The algorithm remains to be tested on more clinical data.

The coherence factor (CF) [44] is widely used for aberration correction and side lobe suppression in PA and US imaging. Jeon et al. combined the DMAS algorithm with CF for clinical PA imaging [45]. Mozaffarzadeh et al. combined MV with CF to achieve better resolution in PA imaging [46]. Spadin et al. compared the frequency-domain and delay-and-sum PA image reconstruction with CF weighting [47]. Mukaddim et al. applied spatiotemporal CF to in vivo cardiac PA image beamformation [48]. Bell et al. applied short-lag spatial coherence beamforming to cardiac ultrasound imaging [49].

Here we propose an improved beamformer, named DMAS-LAG-CF which combines lag-based DMAS (DMAS-LAG) [39] with CF to improve spatial resolution and image contrast for better in vivo ovarian cancer diagnosis. To our best knowledge, this is the first time that DMAS-LAG-CF has been implemented and applied to photoacoustic imaging, especially for clinical cancer studies. Due to the nonlinear process of DMAS-LAG-CF, the reconstructed image intensity is not linearly proportional to the initial PA pressure. Therefore, the typical linear unmixing method for calculating the relative total hemoglobin concentration and oxygen saturation is not suitable. However, the proposed DMAS-LAG-CF can achieve better image contrast using a single wavelength in near real-time imaging.

4.2 Materials and methods

4.2.1 Proposed Reconstruction Algorithm

The improved version of DMAS [29] is formulized as

$$s_{ij}(t) = sign\left(s_i(t)s_j(t)\right).\sqrt{|s_i(t)s_j(t)|} \quad \text{Eq. (5.1)}$$

$$y_{DMAS}(t) = \sum_{i=1}^{N-1}\sum_{j=i+1}^{N} s_{ij}(t), \quad \text{Eq. (5.2)}$$

where s_i and s_j are the delayed signals received by the i^{th} and j^{th} elements, respectively. N is the number of elements used to receive signals. y_{DMAS} is the DMAS beamformed output. In this algorithm, due to the multiplication and summation, the central frequency, f_0, of the original signals is shifted to DC and $2f_0$ in the output. Thus, the output is filtered by a bandpass filter, centered at $2f_0$, to recover frequency components while removing DC components. Eqn. 2 can be expanded as

$$y_{DMAS} = [\bar{s}_1\bar{s}_2 + \bar{s}_2\bar{s}_3 + \cdots + \bar{s}_{N-2}\bar{s}_{N-1} + \bar{s}_{N-1}\bar{s}_N] + [\bar{s}_1\bar{s}_3 + \bar{s}_2\bar{s}_4 + \cdots + \bar{s}_{N-3}\bar{s}_{N-1} + \bar{s}_{N-2}\bar{s}_N] + \cdots + [\bar{s}_1\bar{s}_{N-1} + \bar{s}_2\bar{s}_N] + [\bar{s}_1\bar{s}_N], \quad \text{Eq. (5.3)}$$

where $\bar{s}_i = sign(s_i)\sqrt{|s_i|}$, for $\mathbf{1 \le i \le N}$. In this equation, signal pairs with the same lag are grouped in separate brackets [39]. We consider the output of each of these brackets as a new signal and call it ss_i, which is defined as

$$ss_i = \sum_{k=1}^{N-i} \bar{s}_k \cdot \bar{s}_{k+i}, \text{ for } \mathbf{1 \le i \le N-1}. \quad \text{Eq. (5.4)}$$

We combine each ss_i with the CF, and obtain a new parameter, defined as

$$ccs_i = \sum_{k=1}^{N-i} \overline{cs}_k \cdot \overline{cs}_{k+i}, \text{ for } \mathbf{1 \le i \le N-1}, \quad \text{Eq. (5.5)}$$

where $cs_i = \frac{\left(\sum_{i=1}^{N} s_i\right)^2}{N\sum_{i=1}^{N}(s_i)^2} \cdot s_i$, $\overline{cs}_i = sign(cs_i)\sqrt{|cs_i|}$. Then the final DMAS-LAG-CF can be formulated as

$$y_{DMAS-LAG-CF} = \sum_{i=1}^{N-2} \sum_{j=i+1}^{N-1} \overline{ccs}_i \cdot \overline{ccs}_j \, . \qquad \text{Eq. (5.6)}$$

The schematic diagram of DMAS-LAG-CF is shown in Figure 4.1. All the symbols used in the diagram are the same as those in the Eq. 5.5 and 5.6. This diagram depicts how to synthesize new signals in terms of different lags which are discriminated by different colors in Figure 4.1. To compare the performance of DMAS-LAG-CF with DMAS-CF, we also implemented the DMAS-CF algorithm which is formulized as

$$y_{DMAS-CF} = \sum_{i=1}^{N-1} \sum_{j=i+1}^{N} sign(cs_i \cdot cs_j) . \sqrt{|cs_i \, cs_j|} . \qquad \text{Eq. (5.7)}$$

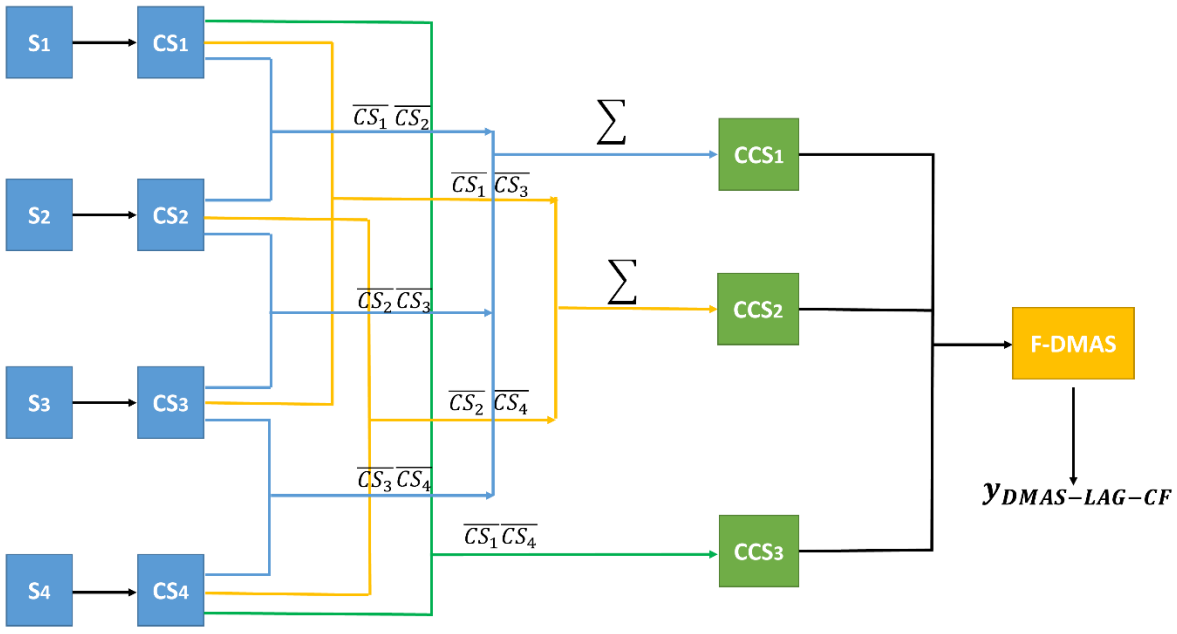

Figure 4.1: Schematic diagram of DMAS-LAG-CF.

4.2.2 Co-registered PAT/US Imaging System

Our co-registered PAT/US imaging system, described in detail in [10, 50], consists of a Ti: sapphire (Symphotics TII, LS-2122) optically pumped with a Q-switched Nd: YAG laser (Symphotics TII, LS-2134) to deliver pulsed laser light (10 – 30 ns pulse duration, 15 Hz pulse repetition rate), a commercial ultrasound system (EC-12R, Alpinion Medical Systems), and a 128 channel curved transvaginal ultrasound transducer (central frequency: 6 MHz, 80% bandwidth). For each imaging position, the system is programmed to record data sequentially at wavelengths of 730, 780, 800, and 830 nm. The pulsed laser light output at tissue surface is below the ANSI safety limit [51]. Note that, due to the nonlinear process of DMAS-LAG-CF, we use only a single wavelength (730 nm) for the following data processing.

4.2.3 Ovarian Cancer Patients

A total of 28 patients enrolled from May 2017 to November 2018, were evaluated in this study. Among these patients, both ovaries were imaged in 12 patients; for the remaining 16 patients, only one suspicious ovary with pathological evaluation was imaged. Among 40 ovaries, 10 had invasive serous or endometroid ovarian cancer, one had a serous borderline tumor, and the rest were benign/normal ovaries. The borderline tumor was included in the cancerous group in the analysis. This study protocol was approved by the Institution Review Board of Washington University Medical School in St. Louis and all patients signed the informed consent.

4.2.4 Feature Selection and Classification

Histograms of PAT image envelopes were computed from the malignant and benign/normal groups, and three features--variance, skewness, and kurtosis, (see Appendix A)--were extracted quantitatively from the histograms to characterize these two groups. The mean values of PAT

image envelopes (PAT_mean) within the regions of interest (ROIs) and the corresponding histogram features were tested using two-sample two-sided Student's t tests. A feature with a p-value equal to or less than 0.05 ($p \leq 0.05$) was considered significant.

Next, we performed a regression analysis on our data to find the best logistic regression model. Models were developed for three sets of independent features extracted from all the patients: PAT_mean alone, PAT_mean and kurtosis combined, and PAT_mean and skewness. Skewness and kurtosis were not evaluated as a set because they are highly correlated by Spearman's cross correlation. For each model, the receiver operating characteristic (ROC) curve and the area under the curve (AUC) were calculated, and the best model was determined by the highest AUC value.

4.2.5 Performance Evaluation

First, we compared the spatial resolution and side lobe performance of the DAS, DMAS, DMAS-CF, DMAS-LAG, and DMAS-LAG-CF beamforming algorithms, using a simulated numerical phantom. The raw data consisted of seven equidistant pairs of point targets located at seven different depths. The transducer array geometry used in the simulation was linear, with 64 elements (element pitch, 231 μm; kerf, 38.5 μm; element height and width, 14 mm and 192.5 μm; lambda, 385 μm). The full width at half maximum (FWHM) was calculated from the fitted Gaussian curve after deconvolution with the transfer function of the transducer, and this value is used as a measure of the spatial resolution throughout the paper. We compared the performance of DAS, DMAS, DMAS-CF, DMAS-LAG, and DMAS-LAG-CF by imaging a 200 μm diameter black thread perpendicular to the imaging plane and submerged in a water tank filled with calibrated intralipid solution (Fresenius Kabi, USA) with a reduced scattering coefficient ($\boldsymbol{\mu_s'}$) of 4 $\mathbf{cm^{-1}}$ and an absorption coefficient ($\boldsymbol{\mu_a}$) of 0.02 $\mathbf{cm^{-1}}$.

Next, we compared the contrast ratios (CRs) of a simulated contrast phantom as reconstructed by the DAS, DMAS, DMAS-CF, DMAS-LAG, and DMAS-LAG-CF beamforming algorithms. Following the same procedure as in [52, 53], we modeled a benign cyst as a 15-mm-diameter sphere within a tissue mimicking medium (the cube size was 84 * 84 * 70 mm) at a depth of 20 mm. The tissue mimicking background medium's $\boldsymbol{\mu_a}$ was set as 0.1 $\mathbf{cm^{-1}}$, and $\boldsymbol{\mu_s'}$ was set as 5 $\mathbf{cm^{-1}}$. As the positive contrast (higher than the background $\boldsymbol{\mu_a}$), the cyst's $\boldsymbol{\mu_a}$ was set as 0.9 $\mathbf{cm^{-1}}$ and $\boldsymbol{\mu_s'}$ was set as 0.0001 $\mathbf{cm^{-1}}$ to mimic an aqueous medium without scattering. The CR index is defined as CR = $\mathbf{20\ log_{10}}\ \boldsymbol{I_{target}/I_{background}}$, where $\boldsymbol{I_{target}}$ and $\boldsymbol{I_{background}}$ are the PAT_mean in the target and background areas. The ideal CR based on $\boldsymbol{\mu_a}$ ratio is 19dB.

We then applied the DAS, DMAS, DMAS-CF, DMAS-LAG, DMAS-LAG-CF algorithms to ovarian cancer patient data to improve the image contrast between the PAT image envelopes of the cancerous masses and those of the benign/normal lesions. We calculated the PAT_mean in each ROI and extracted the histogram features from the corresponding PAT image envelopes. Ultrasound images were employed to select an ROI corresponding to the lesion. Note that we selected only one normal or cancer area for each ovary. Thus, a total of 11 cancer areas and 29 normal areas were obtained for quantitative feature extraction and classification.

4.3 Results

As shown in Figure 4.2 (a), the simulated point target pairs reconstructed by DMAS-LAG-CF are smaller than those reconstructed by the other algorithms. Based on the 1-D profile from DMAS-LAG-CF in Figure 4.2 (b), the two peaks corresponding to the two point targets are sharpest and the side lobes are lowest. Also, from the lateral resolution calculated at three different depths (49,

59, 69 mm) shown in Figure 4.2 (c), the lateral resolution for DMAS-LAG-CF is around 1.70, 1.52, 1.10, and 1.20 times better than the values for DAS, DMAS, DMAS-CF and DMAS-LAG.

In Figure 4.3, the black thread cross-section reconstructed by DMAS-LAG-CF is thinnest. Based on 1-D profiles across the black thread, the lateral resolution of DMAS-LAG-CF is respectively around 1.39, 1.30, 1.07, and 1.15 times better than those of DAS, DMAS, DMAS-CF, and DMAS-LAG. The theoretical value of the spatial resolution is around 0.20 mm.

The geometry of the simulated contrast phantom is shown in Figure 4.4 (a). We selected two background areas for fair judgement (the dashed square marked as 2 and 3 in Figure 4.4 (b), Figure 4.4 (c), Figure 4.4 (d), Figure 4.4 (e), and Figure 4.4 (f)), with corresponding contrast ratios of CR1 and CR2. Comparing Figure 4.4 (b), Figure 4.4 (c), Figure 4.4 (d), Figure 4.4 (e), and Figure 4.4 (f), we can see that the image reconstructed by DMAS-LAG-CF has the best contrast between the target and background area. Quantitatively, the CR1 of DMAS-LAG-CF was around 12.19 dB, 8.81 dB, 7.47 dB, and 4.10 dB higher than those of DAS, DMAS, DMAS-CF, and DMAS-LAG, based on the mean values of the image intensity calculated in the target and background areas. Also the CR2 of DMAS-LAG-CF was around 9.35 dB, 6.83 dB, 5.85 dB, and 2.96 dB higher than those of DAS, DMAS, DMAS-CF, and DMAS-LAG. On average, the CR of DMAS-LAG-CF was around 10.77 dB, 7.82 dB, 6.66 dB, and 3.53 dB higher than those of DAS, DMAS, DMAS-CF, and DMAS-LAG. In Figure 4.4 (c), Figure 4.4 (d), Figure 4.4 (e), and Figure 4.4 (f), one small dot appears underneath the chosen target area because the scattering coefficient of the cyst target is very low, and a small portion of light propagates through the target area with higher light fluence than background to illuminate the region underneath. Also, one red area appears right on top of the chosen target area close to the transducer face, because the light has traveled only a very short distance and has not yet been fully diffused.

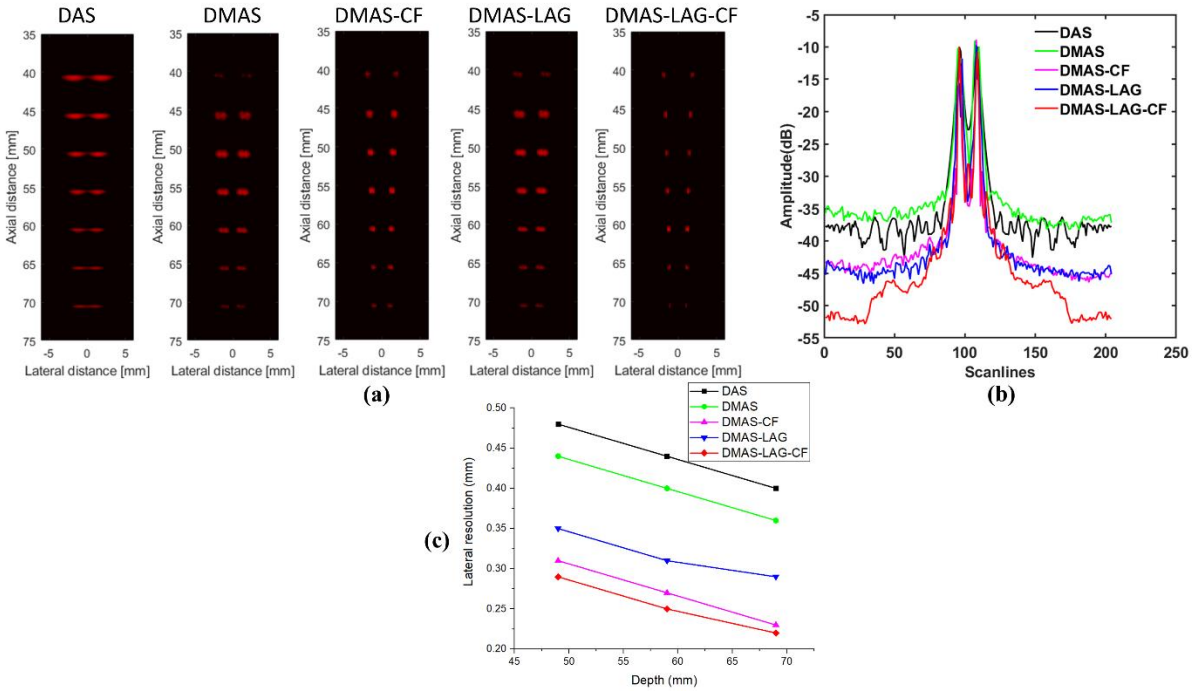

Figure 4.2: (a) Simulated point target pairs reconstructed by DAS, DMAS, DMAS-CF, DMAS-LAG, and DMAS-LAG-CF (dynamic range, 15 dB). (b) The corresponding 1-D profiles of the images in (a) at a depth of 49 mm. (c) The lateral resolution performance for DAS, DMAS, DMAS-CF, DMAS-LAG, and DMAS-LAG-CF at depths of 49 mm, 59 mm, and 69 mm.

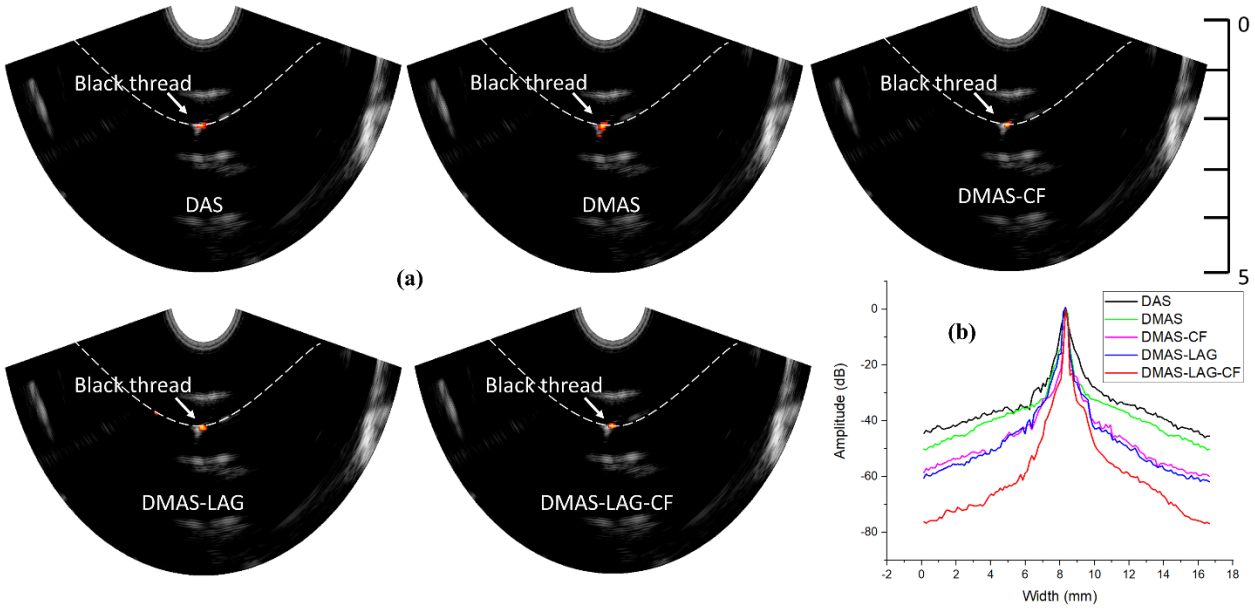

(c)

	DAS	DMAS	DMAS-CF	DMAS-LAG	DMAS-LAG-CF
Lateral resolution (mm)	0.46	0.43	0.35	0.38	0.33

Figure 4.3: (a) Black thread images reconstructed by the DAS, DMAS, DMAS-CF, DMAS-LAG, and DMAS-LAG-CF algorithms (dynamic range, 10 dB; scale, cm). (b) The corresponding 1-D profiles across the black thread (averaged from 20 consecutive envelopes along the depth). (c) Calculated spatial resolution results based on the 1-D profiles across the black thread.

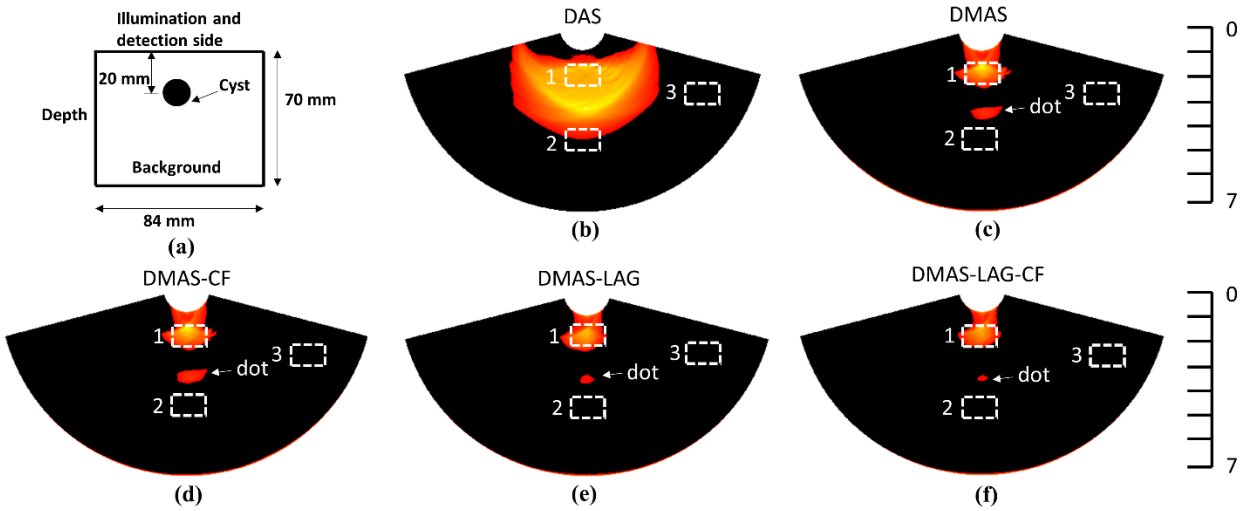

	DAS	DMAS	DMAS-CF	DMAS-LAG	DMAS-LAG-CF
CR1 (dB)	10.74	14.12	15.46	18.83	22.93
CR2 (dB)	14.52	17.04	18.02	20.91	23.87

(g)

Figure 4.4: (a) Phantom geometries used for simulations. Simulated contrast phantom images reconstructed by the DAS (b), DMAS (c), DMAS-CF (d), DMAS-LAG (e), and the DMAS-LAG-CF (f) algorithms (dynamic range, 10 dB; scale bar, cm). (e) Calculated CR results based on the mean values of the image intensity in the target and background areas (target areas: dashed square areas 1 of (b), (c), (d), (e), and (f); background areas: dashed square areas 2 and 3 of (b), (c), (d), (e), and (f)). CR1 and CR2 correspond to the dashed square areas 2 and 3.

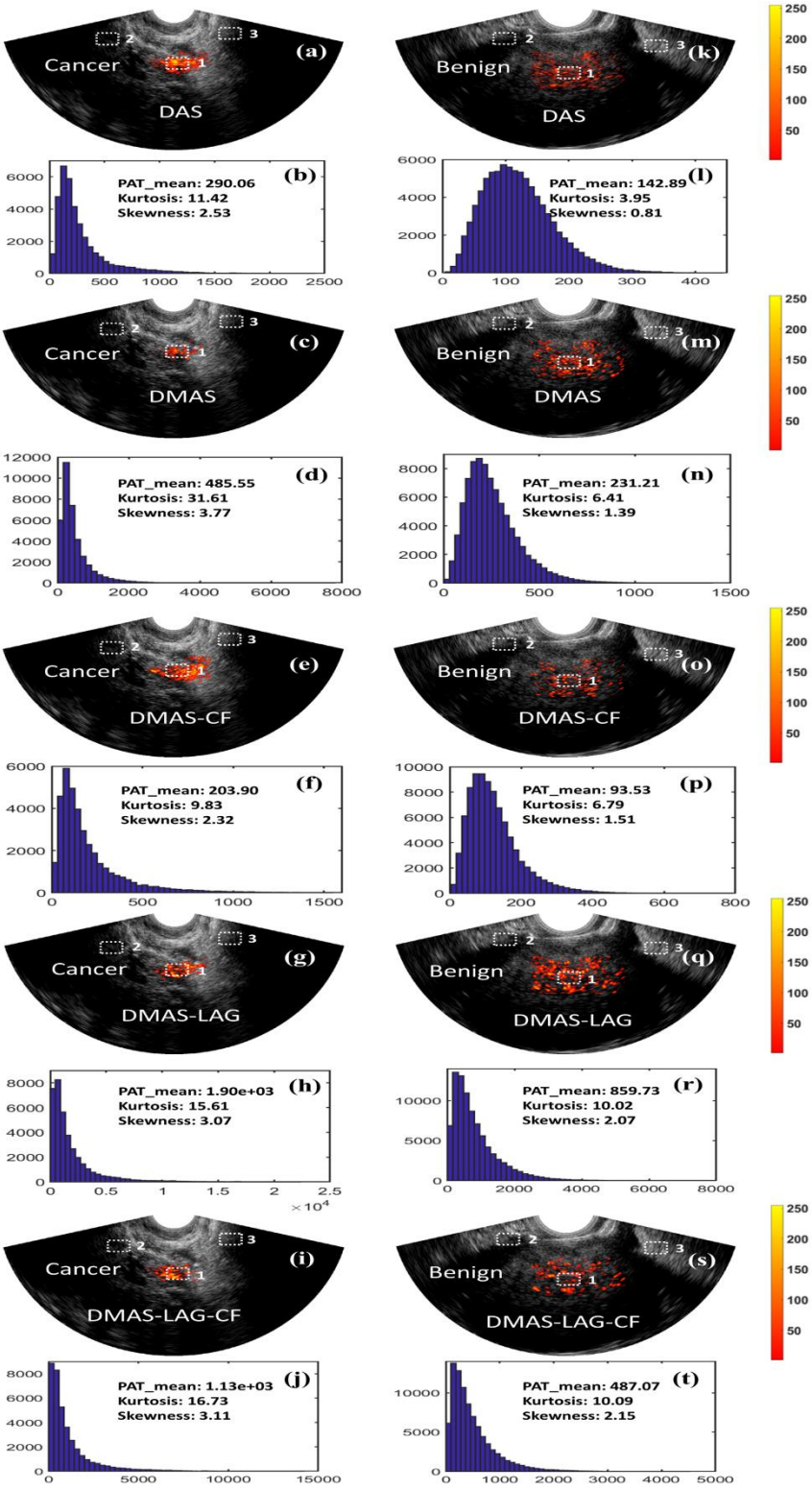

	DAS	DMAS	DMAS-CF	DMAS-LAG	DMAS-LAG-CF
Average CR (dB, cancer)	17.93	19.74	22.27	23.61	24.80
Average CR (dB, benign)	3.43	6.67	7.98	9.76	11.29

(u)

Figure 4.5: PAT images (730 nm) and corresponding histogram features extracted from an ovarian cancer (a)-(j) and a benign ovary (k)-(t). All PAT images are displayed with 15dB dynamic range.

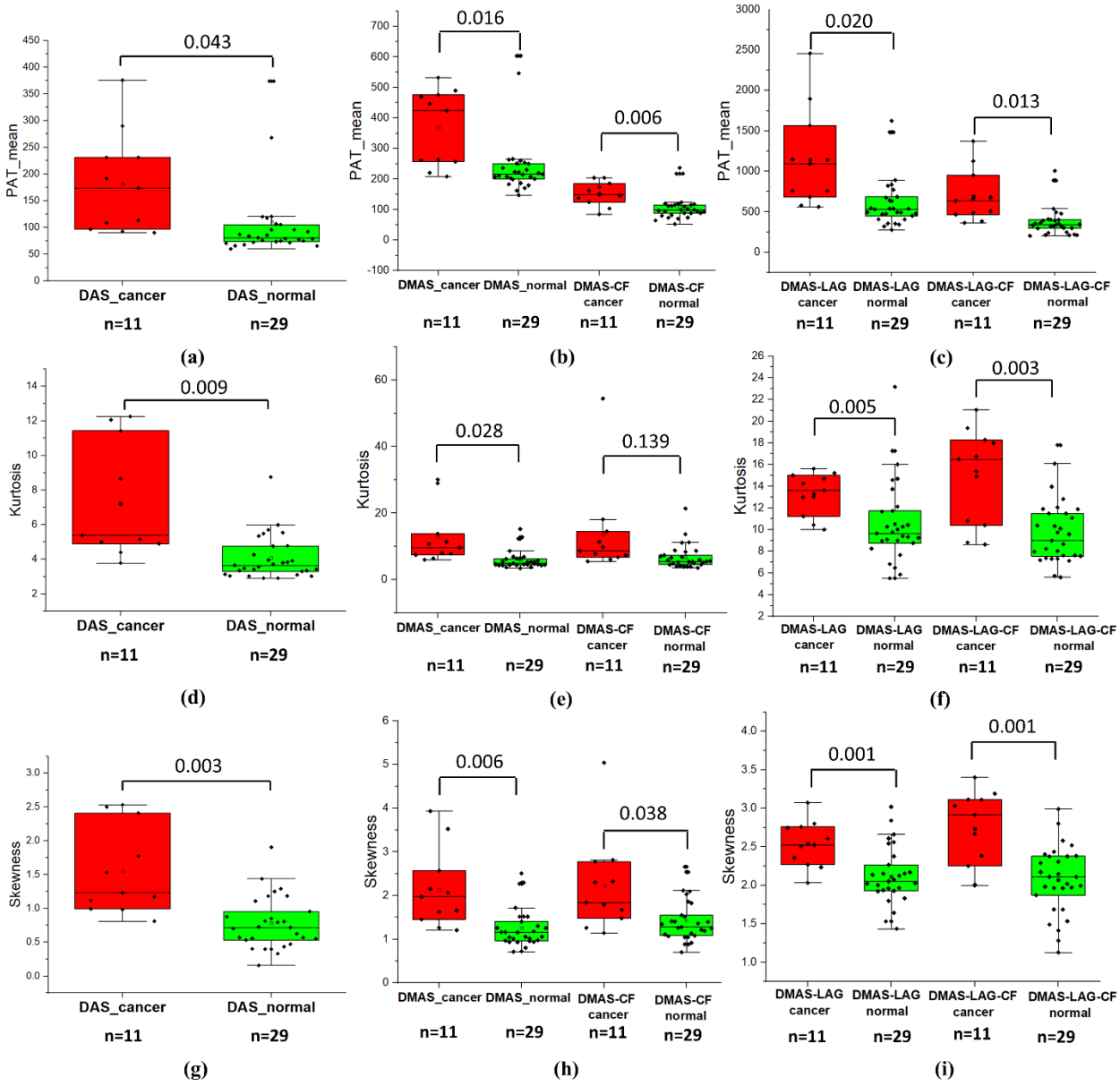

Figure 4.6: (a)-(c): Boxplots of mean values of PAT envelopes using (a) DAS, (b) DMAS (left) and DMAS-CF (right), and (c) DMAS-LAG (left) and DMAS-LAG-CF (right). (d)-(f): Boxplots of kurtosis using (d) DAS, (e) DMAS (left) and DMAS-CF (right), and (f) DMAS-LAG (left) and

DMAS-LAG-CF (right). (g)-(i): Boxplots of skewness using (g) DAS, (h) DMAS (left) and DMAS-CF (right), and (i) DMAS-LAG (left) and DMAS-LAG-CF (right). The *p*-value is shown in the associated plot. The number of samples in each group is also shown in the x-axis of each plot.

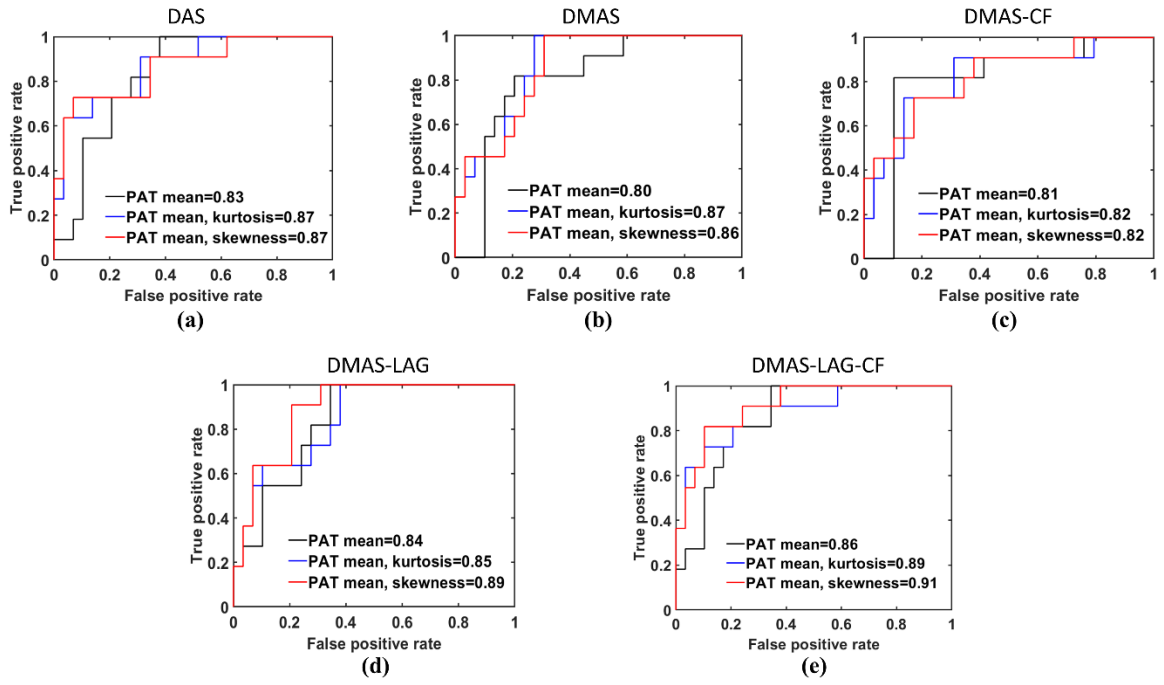

Figure 4.7: ROC curves and associated AUC values of five regression models developed to fit the data extracted from all patients. Regression model of DAS (a), DMAS (b), DMAS-CF (c), DMAS-LAG (d), and DMAS-LAG-CF (e).

Figure 4.5 shows one example PAT image (730 nm) from an ovarian cancer, calculated by DAS, DMAS, DMAS-CF, DMAS-LAG, and DMAS-LAG-CF. The CRs were computed from the two background regions and the target central region as marked by the white boxes in the images. The average CRs computed from the two background regions were given in the table. For the cancer case, the DMAS-LAG-CF improved CR of DAS, DMAS, DMAS-CF and DMAS-LAG by 6.9 dB,

5.1 dB, 2.5dB and 1.2 dB, respectively. For the benign case, the corresponding improvements of CR were 7.6 dB, 4.6 dB, 3.4 dB, 1.5 dB, respectively. Thus, DMAS-LAG-CF performs the best on improving CR. However, since the clinical significance is the diagnostic accuracy between cancer and benign/normal ovarian lesions, we have evaluated PAT-mean ratios of the two examples. The PAT-mean ratios of the cancer to benign lesions are 2.32, 2.21, 2.16, 2.11, and 2.03 for DMAS-LAG-CF, DMAS-LAG, DMAS-CF, DMAS, and DAS, respectively. DMAS-LAG-CF improves PAT-mean ratio by 5%, 7%, 10% and 14% compared with DMAS-LAG, DMAS-CF, DMAS, and DAS.

Figure 4.6 shows boxplots for the PAT_mean and histogram features (kurtosis, skewness), across the entire set of 28 patients between the benign/normal and cancer areas for DAS, DMAS, DMAS-CF, DMAS-LAG, and DMAS-LAG-CF. The variance feature, not shown here, is not significant for all five algorithms. The number n in the plots corresponds to the total number of areas. In terms of three extracted histogram features (PAT-mean, kurtosis, and skewness), the p values between cancers and benign/normal lesions obtained from DMAS-LAG and DMAS-LAG-CF were lower than those of the standard DAS beamforming algorithm.

Figure 4.7 shows the ROC curves and AUC values of the fitting data sets, using regression models for DAS (Figure 4.7 (a)), DMAS (Figure 4.7 (b)), DMAS-CF (Figure 4.7 (c)), DMAS-LAG (Figure 4.7 (d)), and DMAS-LAG-CF (Figure 4.7 (e)). When skewness and PAT_mean are included in the feature set, the best performances (the highest AUC values for the data set) are 0.87, 0.86, 0.82, 0.89, and 0.91 for DAS, DMAS, DMAS-CF, DMAS-LAG, and DMAS-LAG-CF, respectively.

4.4 Discussion and Summary

In this paper, we implemented an improved beamformer, named DMAS-LAG-CF, which combines lag-based delay multiply and sum with coherence factor.

We first compared the spatial resolution and contrast performance of the DAS, DMAS, DMAS-CF, DMAS-LAG, and DMAS-LAG-CF beamforming algorithms using a simulated numerical phantom. Compared to the performances of DAS, DMAS, DMAS-CF, and DMAS-LAG, the lateral resolution for DMAS-LAG-CF was around 1.70, 1.52, 1.10, 1.20 times better. Then we imaged a 200 μm diameter black thread perpendicular to the imaging plane and submerged in a water tank filled with calibrated intralipid solution and found that the lateral resolution of DMAS-LAG-CF was around 1.39, 1.30, 1.07, 1.15 times better than those of DAS, DMAS, DMAS-CF, and DMAS-LAG. Afterwards, we compared the CR performance of DAS, DMAS, DMAS-CF, and DMAS-LAG, and DMAS-LAG-CF using a simulated contrast phantom. On average, the CR for DMAS-LAG-CF was around 10.77 dB, 7.82 dB, 6.66 dB, and 3.53 dB higher than those of DAS, DMAS, DMAS-CF, and DMAS-LAG. Thus, the improvement of DMAS-LAG-CF over other algorithms is in image contrast. The two clinical examples have demonstrated similar improvement in computed CRs. The corresponding CRs for the cancer case were 6.9dB, 5.1dB, 2.5dB and 1.2 dB, and CRs for the benign case were 7.6, 4.6,3.4 and 1.5dB.

Since the clinical value of diagnostic accuracy is between cancer and benign/normal lesions, we applied the DMAS-LAG algorithm without and with the coherence factor, to patient data to enhance the contrast between PAT images of cancerous masses and that of benign/normal ovarian lesions. In terms of three extracted histogram features (PAT_mean, kurtosis, and skewness), the p values between cancers and benign/normal lesions were lower than those of the standard DAS

beamforming algorithm. The best DMAS-LAG-CF regression model achieved an AUC of 0.91, when PAT_mean and skewness were included in the feature set. This is significant in offering diagnosis to patients using photoacoustic imaging co-registered with ultrasound.

The three PAT features are related to the distribution of absorbers inside the ovaries. For example, a cancerous ovary has large clusters of highly absorbing micro-vessels, and it is expected that its PAT histogram should be more skewed towards higher mean values. DMAS-LAG and DMAS-LAG-CF improve PA signal coherence over DAS, and thus these algorithms enhance the contrast between highly absorbing cancerous tissue and benign/normal lesions. Kurtosis measures how close the distribution's tail is to the tail of a normal distribution. If there are many outliers in the histogram, the distribution is heavily tailed. Therefore, kurtosis can be a good measure of the number of absorbers that are considered as outliers. Again, DMAS-LAG and DMAS-LAG-CF improve PA signal coherence and therefore increase the deviation of cancerous tissue, with large clusters of highly absorbing micro-vessels, from that of a normal distribution.

DMAS-LAG [39] is essentially the same as the DS-DMAS which improves DMAS by improving off-axis noise levels at deeper depths [35]. Thus, the contrast improvements of DMAS-LAG over DMAS and DMAS-LAG-CF over DMAS-CF are expected. However, both DMAS and DMAS-CF should also improve the diagnostic performance of DAS because they both improve PAT signal coherence by reducing off-axis noise. Only PAT_mean computed from DMAS between cancer and benign/normal groups has a lower p value than that of DAS. We were supervised that the ROC analysis of patient data did not show improvement of DMAS and DMAS-CF over DAS, which warrants further investigation.

Note that, compared with the computational complexity of DAS ($O(N)$, where N is the number of elements), DMAS-LAG-CF has an exponentially higher computational complexity ($O(N^2)$). Also, the bandpass filters involved in the post-processing of the DMAS-LAG-CF rely on two computationally intensive Fourier transforms. In processing a single frame from a patient dataset, the average runtime of our DMAS-LAG-CF algorithm was about 10 times longer than that of DAS. The reconstruction was performed by running MATLAB R2018 on a Windows 10 operating system using an i3-6100 CPU (Intel, Santa Clara, CA, USA) and 16 GB memory. To achieve near real-time clinical application, the processing speed can be improved with a better computational platform and GPU processing. Also, the two-stage signum, absolute, and square root operations slowed down DMAS-LAG-CF. In some application situations, we can perform only one stage of the above operations to improve the processing speed at the expense of slightly lower resolution and higher side lobes. Moreover, we can reduce the lag number for combinational multiplication in the second stage to improve the processing speed at the cost of a decreased effective aperture (spatial resolution).

Overall, this initial study shows that the proposed beamforming algorithm can achieve valuably better image contrast for improved diagnosis of ovarian cancer with a cohort of 28 patients.

DMAS and DMAS-LAG are nonlinear beamformers and the linear unmixing method to compute the relative hemoglobin contrast from multi-wavelength data cannot be implemented directly. This is an inherent limitation of DMAS based beamforming methods. However, the methods can be readily implemented in single wavelength PA imaging for near real time ovarian cancer diagnosis as well as other oncology applications.

Appendix A: Histogram features extraction

The three histogram features can be computed from Eq. (5.8) to (5.10), where x_i is the pixel gray level and N is the total number of pixels.

$$\text{Variance } (\sigma^2) = \frac{1}{N}\sum_{i=1}^{N}(x_i - \mu)^2 \qquad \text{Eq. (5.8)}$$

$$\text{Skewness} = \frac{1}{N}\sum_{i=1}^{N}\left[\frac{x_i-\mu}{\sigma}\right]^3 \qquad \text{Eq. (5.9)}$$

$$\text{Kurtosis} = \frac{1}{N}\sum_{i=1}^{N}\left[\frac{x_i-\mu}{\sigma}\right]^4 - 3. \qquad \text{Eq. (5.10)}$$

References

1. Wang, L. V., & Hu, S., "Photoacoustic tomography: in vivo imaging from organelles to organs," Science, 335(6075), 1458-1462, (2012).

2. Wang, L. V., & Yao, J., "A practical guide to photoacoustic tomography in the life sciences," Nature methods, 13(8), 627, (2016).

3. Oraevsky, A. A., Clingman, B., Zalev, J., Stavros, A. T., Yang, W. T., & Parikh, J. R., "Clinical optoacoustic imaging combined with ultrasound for coregistered functional and anatomical mapping of breast tumors," Photoacoustics, 12, 30-45, (2018).

4. Lin, L., Hu, P., Shi, J., Appleton, C. M., Maslov, K., Li, L., ... & Wang, L. V., "Single-breath-hold photoacoustic computed tomography of the breast," Nature communications, 9(1), 1-9, (2018).

5. Roll, W., Markwardt, N. A., Masthoff, M., Helfen, A., Claussen, J., Eisenblätter, M., ... & Ntziachristos, V., "Multispectral Optoacoustic Tomography of Benign and Malignant

Thyroid Disorders: A Pilot Study," Journal of Nuclear Medicine, 60(10), 1461-1466, (2019).

6. Yang, M., Zhao, L., He, X., Su, N., Zhao, C., Tang, H., ... & Zhang, B., "Photoacoustic/ultrasound dual imaging of human thyroid cancers: an initial clinical study," Biomedical optics express, 8(7), 3449-3457, (2017).

7. Peng, K., He, L., Wang, B., & Xiao, J., "Detection of cervical cancer based on photoacoustic imaging—the in-vitro results," Biomedical optics express, 6(1), 135-143, (2015).

8. Yang, G., Amidi, E., Chapman, W. C., Nandy, S., Mostafa, A., Abdelal, H., ... & Zhu, Q., "Co-registered photoacoustic and ultrasound imaging of human colorectal cancer," Journal of biomedical optics, 24(12), 121913, (2019).

9. Leng, X., Chapman, W., Rao, B., Nandy, S., Chen, R., Rais, R., ... & Zhu, Q., "Feasibility of co-registered ultrasound and acoustic-resolution photoacoustic imaging of human colorectal cancer," Biomedical optics express, 9(11), 5159-5172, (2018).

10. Nandy, S., Mostafa, A., Hagemann, I. S., Powell, M. A., Amidi, E., Robinson, K., ... & Zhu, Q., "Evaluation of ovarian cancer: initial application of coregistered photoacoustic tomography and US," Radiology, 289(3), 740-747, (2018).

11. Amidi, E., Mostafa, A., Nandy, S., Yang, G., Middleton, W., Siegel, C., & Zhu, Q., "Classification of human ovarian cancer using functional, spectral, and imaging features obtained from in vivo photoacoustic imaging," Biomedical optics express, 10(5), 2303-2317, (2019).

12. Liu, C., Xing, M., Cong, B., Qiu, C., He, D., Wang, C., ... & Ma, T., "In vivo transrectal imaging of canine prostate with a sensitive and compact handheld transrectal array photoacoustic probe for early diagnosis of prostate cancer," Biomedical optics express, 10(4), 1707-1717, (2019).

13. Dogra, V. S., Chinni, B. K., Valluru, K. S., Joseph, J. V., Ghazi, A., Yao, J. L., ... & Rao, N. A., "Multispectral photoacoustic imaging of prostate cancer: preliminary ex-vivo results," Journal of clinical imaging science, 3, (2013).

14. Wang, Y., Zhan, Y., Harris, L. M., Khan, S., & Xia, J., "A portable three-dimensional photoacoustic tomography system for imaging of chronic foot ulcers," Quantitative imaging in medicine and surgery, 9(5), 799, (2019).

15. Jo, J., Xu, G., Cao, M., Marquardt, A., Francis, S., Gandikota, G., & Wang, X., "A functional study of human inflammatory arthritis using photoacoustic imaging," Scientific reports, 7(1), 1-9, (2017).

16. van den Berg, P. J., Daoudi, K., Moens, H. J. B., & Steenbergen, W., "Feasibility of photoacoustic/ultrasound imaging of synovitis in finger joints using a point-of-care system," Photoacoustics, 8, 8-14, (2017).

17. Jo, J., Tian, C., Xu, G., Sarazin, J., Schiopu, E., Gandikota, G., & Wang, X., "Photoacoustic tomography for human musculoskeletal imaging and inflammatory arthritis detection," Photoacoustics, 12, 82-89, (2018).

18. Aguirre, J., Schwarz, M., Garzorz, N., Omar, M., Buehler, A., Eyerich, K., & Ntziachristos, V., "Precision assessment of label-free psoriasis biomarkers with ultra-broadband optoacoustic mesoscopy," Nature Biomedical Engineering, 1(5), 1-8, (2017).

19. Kim, J., Kim, Y. H., Park, B., Seo, H. M., Bang, C. H., Park, G. S., ... & Kim, C., "Multispectral ex vivo photoacoustic imaging of cutaneous melanoma for better selection of the excision margin," British Journal of Dermatology, 179(3), 780-782, (2018).

20. Attia, A. B. E., Chuah, S. Y., Razansky, D., Ho, C. J. H., Malempati, P., Dinish, U. S., ... & Tan, M. W. P., "Noninvasive real-time characterization of non-melanoma skin cancers with handheld optoacoustic probes," Photoacoustics, 7, 20-26 (2017).

21. American Cancer Society. Cancer facts and figures, 2019, American Cancer Society, Atlanta, GA (2019).

22. Clarke-Pearson, D. L., "Screening for ovarian cancer," New England Journal of Medicine, 361(2), 170-177, (2009).

23. Finkler, N. J., Benacerraf, B. E. R. Y. L., Lavin, P. T., Wojciechowski, C. A. R. O. L., & Knapp, R. C., "Comparison of serum CA 125, clinical impression, and ultrasound in the preoperative evaluation of ovarian masses," Obstetrics and gynecology, 72(4), 659-664, (1988).

24. Jacobs, I., Oram, D., Fairbanks, J., Turner, J., Frost, C., & Grudzinskas, J. G., "A risk of malignancy index incorporating CA 125, ultrasound and menopausal status for the accurate preoperative diagnosis of ovarian cancer," BJOG: An International Journal of Obstetrics & Gynaecology, 97(10), 922-929, (1990).

25. Van Calster, B., Timmerman, D., Bourne, T., Testa, A. C., Van Holsbeke, C., Domali, E., ... & Valentin, L, "Discrimination between benign and malignant adnexal masses by specialist ultrasound examination versus serum CA-125," JNCI: Journal of the National Cancer Institute, 99(22), 1706-1714, (2007).

26. Nossov, V., Amneus, M., Su, F., Lang, J., Janco, J. M. T., Reddy, S. T., & Farias-Eisner, R., "The early detection of ovarian cancer: from traditional methods to proteomics. Can we really do better than serum CA-125?" American journal of obstetrics and gynecology, 199(3), 215-223, (2008).

27. Di-XIA, C. H. E. N., SCHWARTZ, P. E., Xinguo, L., & ZHAN, Y., "Evaluation of CA 125 levels in differentiating malignant from benign tumors in patients with pelvic masses," Obstetrics & Gynecology, 72(1), 23-27, (1988).

28. Lim, H. B., Nhung, N. T. T., Li, E. P., & Thang, N. D., "Confocal microwave imaging for breast cancer detection: Delay-multiply-and-sum image reconstruction algorithm," IEEE Transactions on Biomedical Engineering, 55(6), 1697-1704, (2008).

29. Matrone, G., Savoia, A. S., Caliano, G., & Magenes, G., "The delay multiply and sum beamforming algorithm in ultrasound B-mode medical imaging," IEEE transactions on medical imaging, 34(4), 940-949, (2014).

30. Park, J., Jeon, S., Meng, J., Song, L., Lee, J. S., & Kim, C., "Delay-multiply-and-sum-based synthetic aperture focusing in photoacoustic microscopy," Journal of biomedical optics, 21(3), 036010, (2016).

31. Alshaya, A., Harput, S., Moubark, A. M., Cowell, D. M., McLaughlan, J., & Freear, S., "Spatial resolution and contrast enhancement in photoacoustic imaging with filter delay multiply and sum beamforming technique," In IEEE International Ultrasonics Symposium (IUS) (pp. 1-4), (2016).

32. Matrone, G., Ramalli, A., Savoia, A. S., Tortoli, P., & Magenes, G., "High frame-rate, high resolution ultrasound imaging with multi-line transmission and filtered-delay multiply and sum beamforming," IEEE transactions on medical imaging, 36(2), 478-486, (2016).

33. Mozaffarzadeh, M., Mahloojifar, A., Orooji, M., Kratkiewicz, K., Adabi, S., & Nasiriavanaki, M., "Linear-array photoacoustic imaging using minimum variance-based delay multiply and sum adaptive beamforming algorithm," Journal of biomedical optics, 23(2), 026002, (2018).

34. Capon, J., "High-resolution frequency-wavenumber spectrum analysis," Proceedings of the IEEE, 57(8), 1408-1418, (1969).

35. Mozaffarzadeh, M., Mahloojifar, A., Orooji, M., Adabi, S., & Nasiriavanaki, M., "Double-stage delay multiply and sum beamforming algorithm: Application to linear-array photoacoustic imaging," IEEE Transactions on Biomedical Engineering, 65(1), 31-42, (2017).

36. Mozaffarzadeh, M., Hariri, A., Moore, C., & Jokerst, J. V., "The double-stage delay-multiply-and-sum image reconstruction method improves imaging quality in a led-based photoacoustic array scanner," Photoacoustics, 12, 22-29, (2018).

37. Miri Rostami, S. R., Mozaffarzadeh, M., Ghaffari-Miab, M., Hariri, A., & Jokerst, J., "GPU-accelerated double-stage delay-multiply-and-sum algorithm for fast photoacoustic tomography using LED excitation and linear arrays," Ultrasonic Imaging, 41(5), 301-316, (2019).

38. Mozaffarzadeh, M., Varnosfaderani, M. H., Sharma, A., Pramanik, M., de Jong, N., & Verweij, M. D., "Enhanced contrast acoustic-resolution photoacoustic microscopy using double-stage delay-multiply-and-sum beamformer for vasculature imaging," Journal of biophotonics, 12(11), e201900133, (2019).

39. Song, K., Liu, P., & Liu, D. C., "Combining autocorrelation signals with delay multiply and sum beamforming algorithm for ultrasound imaging," Medical & Biological Engineering & Computing, 57(12), 2717-2729, (2019).

40. Polichetti, M., Varray, F., Bera, J. C., Cachard, C., & Nicolas, B., "A nonlinear beamformer based on p-th root compression-application to plane wave ultrasound imaging," Applied Sciences, 8(4), 599, (2018).

41. Mozaffarzadeh, M., Periyasamy, V., Pramanik, M., & Makkiabadi, B., "Effcient nonlinear beamformer based on P'th root of detected signals for linear-array photoacoustic tomography: application to sentinel lymph node imaging," Journal of biomedical optics, 23(12), 121604, (2018).

42. Polichetti, M., Varray, F., Matrone, G., Savoia, A. S., Bera, J. C., Cachard, C., & Nicolas, B., "A computationally efficient nonlinear beamformer based on p-th root signal compression for enhanced ultrasound b-mode imaging," In 2017 IEEE IUS, 1-4, (2017).

43. Cho, S., Jeon, S., Choi, W., Managuli, R., & Kim, C., "Nonlinear pth root spectral magnitude scaling beamforming for clinical photoacoustic and ultrasound imaging." Optics Letters, 45(16), 4575-4578, (2020).

44. Mallart, R., & Fink, M., "Adaptive focusing in scattering media through sound-speed inhomogeneities: The van Cittert Zernike approach and focusing criterion," The Journal of the Acoustical Society of America, 96(6), 3721-3732, (1994).

45. Jeon, S., Park, E. Y., Choi, W., Managuli, R., jong Lee, K., & Kim, C., "Real-time delay-multiply-and-sum beamforming with coherence factor for in vivo clinical photoacoustic imaging of humans," Photoacoustics, 15, 100136, (2019).

46. Mozaffarzadeh, M., Makkiabadi, B., Basij, M., & Mehrmohammadi, M., "Image improvement in linear-array photoacoustic imaging using high resolution coherence factor weighting technique," BMC Biomedical Engineering, 1(1), 10, (2019).

47. Spadin, F., Jaeger, M., Nuster, R., Subochev, P., & Frenz, M., "Quantitative comparison of frequency-domain and delay-and-sum optoacoustic image reconstruction including the effect of coherence factor weighting," Photoacoustics, 17, 100149, (2020).

48. Al Mukaddim, R., & Varghese, T., "Spatiotemporal Coherence Weighting for In Vivo Cardiac Photoacoustic Image Beamformation," IEEE Transactions on Ultrasonics, Ferroelectrics, and Frequency Control (2020).

49. Bell, M. A. L., Goswami, R., Kisslo, J. A., Dahl, J. J., & Trahey, G. E., "Short-lag spatial coherence imaging of cardiac ultrasound data: Initial clinical results," Ultrasound in medicine & biology, 39(10), 1861-1874, (2013).

50. Yang, G., Amidi, E., Nandy, S., Mostafa, A., & Zhu, Q., "Optimized light delivery probe using ball lenses for co-registered photoacoustic and ultrasound endo-cavity subsurface imaging," Photoacoustics, 13, 66-75, (2019).

51. Newcomer, E., Yang, G., Sun, B., Luo, H., Shen, D., Achilefu, S., ... & Zhu, Q., "Photoacoustic Laser Effects in Live Mouse Blastocysts: Pilot Safety Studies of DNA Damage from Photoacoustic Imaging Doses," F&S Science (2020).

52. Akhlaghi, N., Pfefer, T. J., Wear, K. A., Garra, B. S., & Vogt, W. C., "Multidomain computational modeling of photoacoustic imaging: verification, validation, and image quality prediction," Journal of biomedical optics, 24(12), 121910, (2019).

53. Heijblom, M., Piras, D., Maartens, E., Huisman, E. J., van den Engh, F. M., Klaase, J. M., ... & Manohar, S., "Appearance of breast cysts in planar geometry photoacoustic mammography using 1064-nm excitation," Journal of biomedical optics, 18(12), 126009, (2013).

Chapter 5: Assess human colorectal cancer, using a co-registered photoacoustic and ultrasound tomography system

5.1 Introduction

Photoacoustic imaging (PAI) is an emerging technique which can provide high optical absorption contrast images at reasonable microscale resolution and clinically relevant depths [1]. Several studies have established that optical absorption parameters are important biomarkers directly related to the tissue microvasculature, tumor angiogenesis or tumor hypoxia [2-4]. In general, PAI is classified into photoacoustic microscopy (PAM) and photoacoustic tomography (PAT) [1]. Previously, PAM or Photoacoustic endoscopy (PAE) have demonstrated the capability of detecting human colorectal cancer [5-6]. However, the low imaging speed (limited by the laser repetition rate and scanning scheme), small imaging area, and shallow penetration depth (<7 mm) created obstacles for clinical applications.

Compared with PAM, PAT is able to penetrate deeper with a faster data acquisition speed and a larger field of view due to the use of ultrasonic arrays and a wide optical beam. Several studies have demonstrated that PAT/US dual-modality imaging system can provide anatomical and functional information in tumors [7-13], but no prior applications in the human distal GI tract have been reported using PAT/US dual-modality imaging.

Adenocarcinoma of the colon and rectum is the second most common malignancy diagnosed globally and the 4th leading cause of cancer mortality, with more than 100,000 new cases diagnosed annually in the US [14-15]. Accurate staging and post-treatment surveillance of this prevalent

disease are critical because treatment strategies are predicated upon the stage at presentation and response to therapy – in some instances, detailed imaging allows certain patients to avoid surgery altogether. While colonoscopy and biopsy are the gold-standard diagnostic tests for colorectal cancers [16], multiple imaging modalities including optical imaging [17-18], endoscopic ultrasound (EUS), pelvic magnetic resonance imaging (MRI), computed tomography (CT) and positron emission tomography (PET) are also utilized.

Unfortunately, each of these modalities have critical weaknesses when evaluating colorectal tumors. White light endoscopy (WLE) only detects macroscopic morphology and provides no functional assessment of the imaged tissue. MRI has limited between-slice resolution and is often unable to differentiate early tumors from benign neoplasia, committing patients to potentially more invasive treatment regimens than needed [19-20]. Monitoring of tumors after chemotherapy and radiation with MRI is often confounded by fibrotic reaction and edema, which can appear similar to residual tumor [21]. CT has poorer resolution of the bowel wall layers in comparison to MRI, subsequently limiting its ability to describe circumferential resection margin (CRM) status or serosal invasion in locally advanced cases. Additionally, CT also cannot distinguish induration or peritumoral fibrosis from frank malignant disease with a high degree of specificity, further limiting its application in local tumor staging [19]. PET imaging is also plagued by poor resolution, and EUS remains highly user-dependent and unable to resolve small islands of tumor [19]. Therefore, critical need exists for precise imaging modalities of colorectal tumors for both staging and therapeutic response evaluations.

PAT, in contrast, uniquely provides functional imaging at high resolution by using hemoglobin as an endogenous contrast agent. By detecting the abnormal vasculature that accompanies colorectal malignancies, we hypothesized that this modality might be able to identify malignant or residual tumors otherwise undetectable by current clinical imaging. We therefore performed the following pilot study to test a real-time co-registered PAT/US system prototype and assess its ability to delineate differences between benign and malignant tissue. To the best of our knowledge, this study is the first utilizing co-registered PAT/US to evaluate human colon samples.

5.2 Methods

5.2.1 Human Sample Preparation

Freshly resected colon and rectum samples obtained from patients undergoing surgery at Washington University School of Medicine were imaged immediately after surgery. Patients with known benign neoplasia (polyps) as well as malignancies (adenocarcinoma) were eligible for imaging. Cancer patients who had received preoperative treatment with chemotherapy and /or radiation were also included. The study was approved by the Institutional Review Board (IRB) at Washington University (#201707066). Informed consent was obtained from all patients. Specimens were obtained from the operating room as previously described [6].

A total of 23 tissue samples were imaged in the pilot study using the PAT/US system. This included untreated colorectal adenocarcinomas (n=12), precancerous polyps (n=6), colorectal cancer following chemotherapy or radiation and chemotherapy (n=4), and post polypectomy (n=1). Two treated patients have achieved complete pathological response and two partial response. The majority of patients underwent hemicolectomy for cancer and were found to have malignancy on histologic analysis (Table 5.1).

Table 5.1: Summary of Specimens

Patient ID	Surgery	Pathology
1	Total colectomy	Moderately differentiated adenocarcinoma (T3)
2	Right Hemicolectomy	Tubular adenoma (precancerous polyp)
3	Right Hemicolectomy	Moderately differentiated adenocarcinoma (T2)
4	Sigmoid colectomy	Treated moderately differentiated adenocarcinoma (T3); post chemotherapy
5	Right Hemicolectomy	Tubular adenoma (precancerous polyp)
6	Low anterior resection	Complete pathologic response-no residual tumor after radiation and chemotherapy
7	Left colectomy	Moderately differentiated adenocarcinoma (T2)
8	Low anterior resection	Complete pathologic response-no residual tumor following radiation and chemotherapy
9	Low anterior resection	Tubulovillous adenoma (precancerous polyp)
10	Right hemicolectomy	Moderately differentiated adenocarcinoma (T3)
11	Right hemicolectomy	Moderately differentiated adenocarcinoma (T2)
12	Right hemicolectomy	Moderately differentiated adenocarcinoma (T4)
13	Right hemicolectomy	Tubular adenoma (precancerous polyp)
14	Left colectomy	Moderately differentiated adenocarcinoma (T4)
15	Left Hemicolectomy	Tubulovillous adenoma (precancerous polyp)
16	Low anterior resection	No residual tumor following prior polypectomy* Moderately differentiated adenocarcinoma (T3)
17	Sigmoidectomy	Moderately differentiated adenocarcinoma (T2)
18	Transverse colectomy	Treated moderately differentiated adenocarcinoma (T3); post radiation and chemotherapy
19	Low anterior resection	Moderately differentiated adenocarcinoma (T3) Moderately to poorly differentiated adenocarcinoma (T3)
20	Low anterior resection	Moderately differentiated adenocarcinoma (T3)
21	Total colectomy	Differentiated adenocarcinoma (mixed polyp and adenocarcinoma)
22	Right hemicolectomy	
23	Right hemicolectomy	

Note: T is the primary tumor depth of invasion, per TNM guidelines.

* No residual tumor was found after polypectomy. We have grouped this case with the complete responders.

5.2.2 Co-registered Ultrasound-guided Photoacoustic Tomography System

As shown in Figure 5.1, the system [11, 22] consists of three main parts: a Ti:sapphire laser (Symphotics TII, LS-2134, Symphotics, Camarillo, California) optically pumped with a Q-switched Nd:YAG laser (Symphotics TII, LS-2122), an optimized optical fiber-based light

delivery system [23], and a commercial US system (EC-12R, Alpinion Medical System, Republic of Korea) used for acquiring the corresponding US and PAT data. With this system, pulsed laser light (pulse duration: 10 ns, pulse repetition rate: 15Hz, 20 mJ/pulse at 750 nm wavelength) was delivered to tissue placed on a 2D motorized scanning stage. B-scan images were acquired for four wavelengths (730, 780, 800, 830 nm) at each area of imaged tissue among the 23 specimens. The overall scanning area varied from 1 to 3 cm, while image acquisition time for a region of interest (ROI) was 12-15 seconds with a frame rate of 15 frames per second. Care was taken to acquire images from abnormal tissues as well as corresponding normal areas, as marked by a trained pathologist.

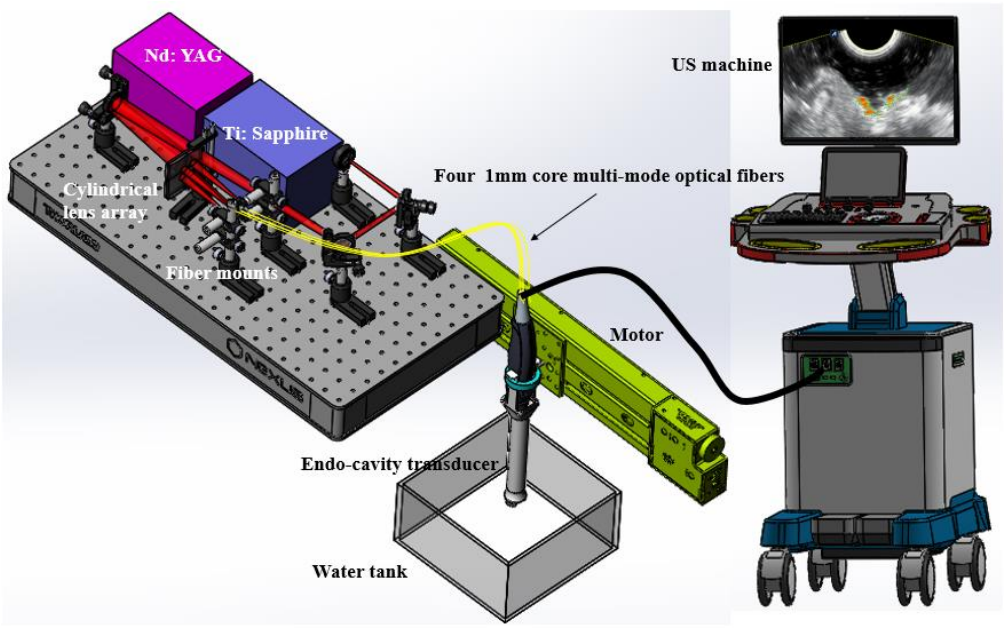

Figure 5.1: Schematic diagram of co-registered ultrasound-guided photoacoustic tomography system.

5.2.3 Extraction of Functional, Spectral, and Textural features

Several functional, spectral, and textural features were extracted from the PAT and US data and images as given in Table 5.2.

Table 5.2: Abbreviations

Abbreviation	Description
rHbT	relative total hemoglobin
SS (PAT)	mean PAT spectral slope
0.5MHz SI (PAT)	0.5 MHz spectral intercept from PAT spectra
MBF (PAT)	mid-band fit from PAT spectra
SS (US)	mean US spectral slope
0.5MHz SI (US)	0.5 MHz spectral intercept from US spectra
MBF (US)	mid-band fit from US spectra
Sig_rad	standard deviation of the mean radon transform
Homogeneity	the homogeneity of image textures
Energy	the grayscale distribution homogeneity of images and texture crudeness
Contrast	the sharpness of images and the depth of texture grooves
Correlation	the consistency of image texture

Functional features

The relative oxy-hemoglobin ($rHbO_2$) and deoxy-hemoglobin (rHb) at each pixel can be calculated using the following equations:

$$rHbO_2(r,\theta) = \overline{C(r,\theta)}HbO_2(r,\theta) \quad \text{Eq. (5.1)}$$

$$rHb(r,\theta) = \overline{C(r,\theta)}Hb(r,\theta), \quad \text{Eq. (5.2)}$$

where $\overline{C(r,\theta)}$=$\Gamma C_0(r,\theta)\emptyset(r,\theta)$, Γ is the tissue's Grüneisen parameter, $C_0(r,\theta)$ is the system acoustic operator, $\emptyset(r,\theta)$ is the local fluence which can be approximated as wavelength independent at the narrow wavelength window we have used. Based on these equations, deriving $rHbO_2$ and rHb requires a known tissue fluence distribution. Since this distribution is difficult to

determine in human tissue due to wide variation in composition, we computed relative $rHbO_2$ and rHb values instead. By summing the $rHbO_2$ and rHb at each pixel, the relative total hemoglobin (rHbT) for each pixel is computed; the average rHbT for a ROI was then calculated by averaging the rHbTs of all pixels in that ROI with a value at least half of the maximum rHbT. All PAT images in the co-registered US and PAT images were rHbT without any normalization.

Spectral features

Ultrasound images were employed to select a proper ROI corresponding to the lesion for PAT spectral feature calculations [9, 24]. First, PAT beam lines with a maximum value close to the background noise level of our co-registered US/PAT system (60 mV) were ignored. The rest of the beam lines were gated by a hamming window, and then their FFT in -10dB frequency range were calculated. Moreover, to cancel the frequency response of the transducer and electrical receiving system [24], the spectra of PAT beams were normalized to the spectra of an approximate point-like target (a 250-μm black thread orthogonal to PAT imaging place with a varied distance to transducer from 0.5 cm to 7 cm and a step of 0.25 cm).

After calibrating our data, each of the calibrated PAT spectra was fitted linearly. The mean spectral slope (SS), midband fit (MBF), and 0.5 MHz spectral intercept (0.5 MHz SI (PAT)) were then calculated (Figure 5.2). We chose 0.5 MHz spectral intercept as a feature instead of 0 MHz because the lower bound of our transducer in PAT mode is approximately 0.5 MHz.

US spectral features were also calculated. To do this, similar method as PAT spectral features extraction was followed. The only differences were: first, the analysis was performed in the frequency range of 3.5 to 7 MHz, which is the -10dB frequency range of the transducer in US

mode. Second, the calibration was performed using a reference gelatin-based phantom constructed in our lab [25].

PAT image features

After visual inspection of PAT frames of malignant and normal colon samples, we noticed that the textures of these images looked different between the two types of samples. To confirm our observation, we extracted PAT image features from available image frames. To do so, a proper ROI was first chosen. To find the center of this ROI, the region surrounding the lesion was determined based on the US image, and the Radon transforms at the two angles of 0 and 90 degrees of the PAT image in this region were calculated. Each of these Radon transforms was then normalized to its own maximum values and a Gaussian curve was fitted to each of them. The center of the square ROI where the image analysis was performed was determined by the means of these two Gaussian curves and its size was assumed to be 1 cm for all cases (Figure 5.3).

Textural features of the normalized PAT images were calculated in the specified ROI [24]. The first step in calculating these features is to construct a gray-level co-occurrence matrix (GLCM) [26]. GLCM quantifies how the pixels are connected in the image. The size of this matrix was chosen as 16*16 pixels. The value of pixel (i,j) of this matrix was chosen to be the number of times that gray levels i and j are adjacent to each other in the PAT image. Note that we assumed that the two gray levels g1 and g2 are adjacent if g1 is positioned at the immediate left of g2. After constructing the GLCM matrix, four textural features were calculated for each PAT image frame using the following equations:

$$Contrast = \sum_{|i-j|=0}^{N-1} |i-j|^2 \sum_{i=1}^{N}\sum_{j=1}^{N} c(i,j) \qquad \text{Eq. (5.3)}$$

$$Correlation = \frac{\sum_{i=1}^{N}\sum_{j=1}^{N}(i-\mu_i)(j-\mu_j)c(i,j)}{\sigma_i\sigma_j} \quad \text{Eq. (5.4)}$$

$$Energy = \sum_{i=1}^{N}\sum_{j=1}^{N}c(i,j)^2 \quad \text{Eq. (5.5)}$$

$$Homogeneity = \sum_{i=1}^{N}\sum_{j=1}^{N}\frac{c(i,j)^2}{1+|i-j|} \quad \text{Eq. (5.6)}$$

where c(i,j) is the value of the (i,j) pixel of the GLCM, N is the dimension of this matrix, and σ and μ are the standard deviation and mean for row i or column j of the GLCM.

The standard deviation of the mean radon transform (Sig_rad) was the last image feature that was calculated in this study. To calculate this feature, the radon transform of the non-normalized PAT image at angles 0 to 90 degrees with a step of 1 degree were calculated and an average was taken over these transforms. Then a Gaussian curve was fitted to this mean radon transform and the standard deviation of this curve was measured.

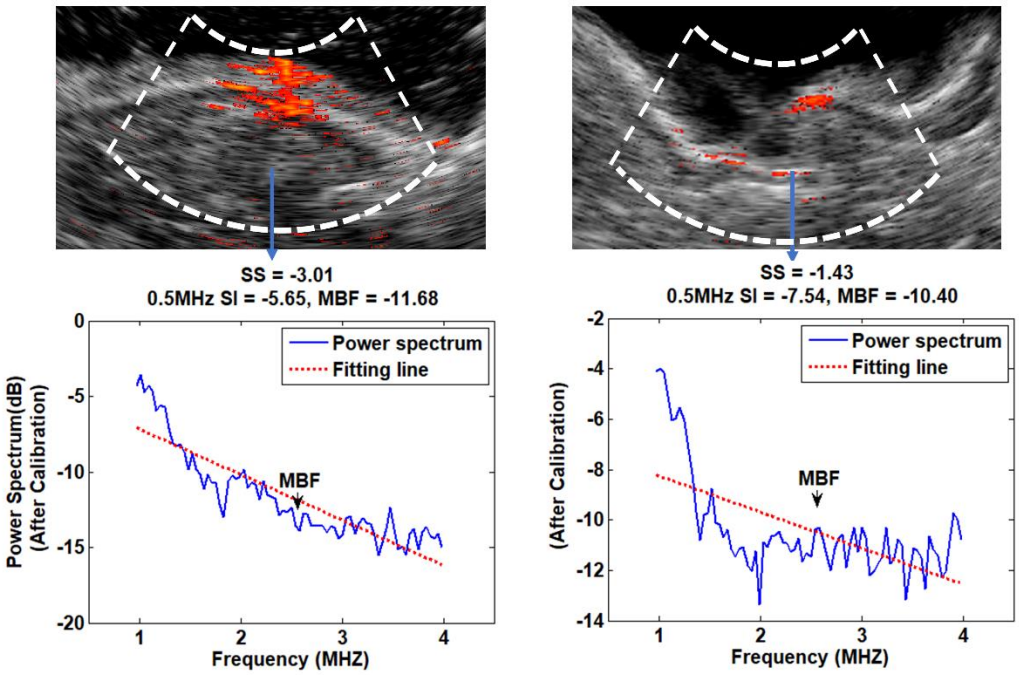

Figure 5.2: Top row: co-registered rHbT and US images of a cancerous (left) and a normal (right) colon sample. Bottom row: the calibrated PAT power spectra along with their fitted lines in the regions marked with the angular dashed lines in each image.

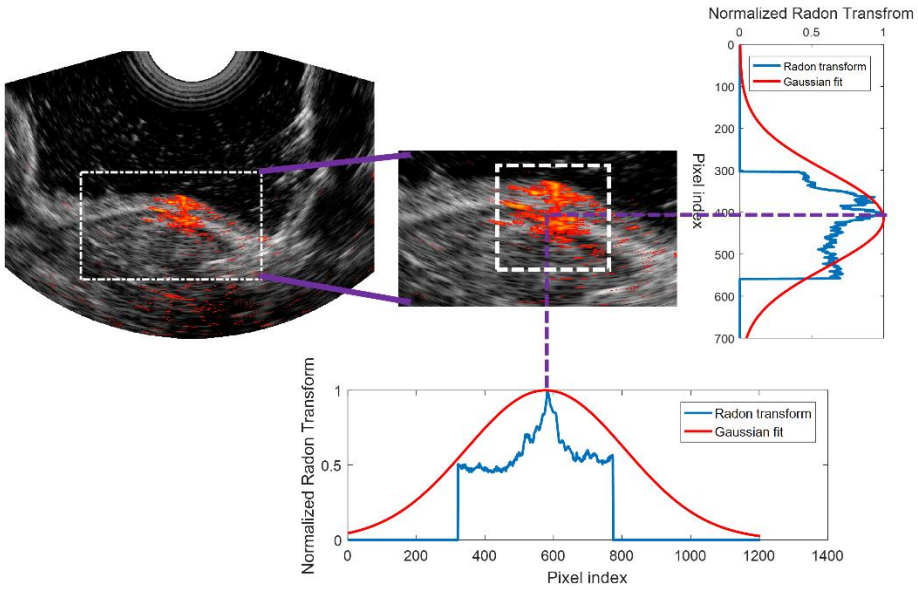

Figure 5.3: ROI selection for image analysis. The region covering the lesion is determined (left), and the normalized Radon transforms at 0 and 90 degrees are calculated. A Gaussian curve is then fitted to each Radon transform. The center of the square ROI where the image analysis is performed is determined by the means of these two Gaussian curves and its size is 1 cm.

5.2.4 Feature Selection and Classification

A two-step approach was used to select features most likely to differentiate normal from untreated malignant tissue. In the first step, all previously discussed PAT/US features were tested in univariate analysis between untreated cancer and normal regions, and *p* values were generated by two-sample two-sided Student's *t* tests. The features where $p > 0.05$ – which we concluded *a priori* not to be significantly associated with malignancy – were excluded from the classification model (Table 5.3).

Table 5.3: Significance testing of individual covariates as related to tissue diagnosis

Feature	p-value
rHbT	<0.001
SS (PAT)	<0.001
0.5 MHz SI (PAT)	0.002
0.5 MHz SI (US)	0.01
Homogeneity	0.01
Energy	0.02
Sig_rad	0.03
MBF (PAT)	0.12
MBF (US)	0.23
SS (US)	0.55

Next, logistic a general logistic mode (GLM) and a support vector machine (SVM) were used to evaluate the strength of association of each feature with the ultimate tissue diagnosis, and a prediction model was then constructed with significant covariates. In total, 18 areas selected from 18 specimens and 12 malignant areas from 12 untreated cancer specimens were used to construct and evaluate the prediction models. Out of these, 12 normal and 8 malignant areas were used for prediction model derivation and the rest (6 normal and 4 malignant areas) for internal model validation. The receiver operating curve (ROC) and the area under the curve (AUC) were used to evaluate the accuracy of the model. Finally, a second prediction model was constructed without rHbT to determine how limiting the PAT/US device to a single wavelength would affect identification of malignancies.

5.3 Results

5.3.1 Qualitative Analysis: Baseline Characteristics of US and PAT Images

Colorectal tissues are composed primarily of fluid, lipid, collagen, and muscle. The general architecture (from superficial to deep) in a normal specimen is mucosa (fluid-filled cells surrounded by lipid bilayers), submucosa (largely composed of extracellular collagen matrix and

some muscle fibers), muscularis propria (muscle), and adipose tissue (lipid). In malignancy, the individual cell types are similar but the architecture is distorted because cancerous cells of mucosal origin penetrate into the deeper layers of the organ. As these cells invade, the organized structure of the tissue is lost.

Figure 5.4 shows specimen photographs, US images, and co-registered PAT/US rHbT maps as well as histologic images from a representative region of normal colon samples (5.4 a - 5.4 d), and a colorectal malignancy (5.4 e - 5.4 h). The white arrows indicate the scanning direction along which B-scans were recorded at four different wavelengths (the imaging plane is perpendicular to the scanning direction). In the standalone ultrasound images, the normal layered structure of the colorectal wall is clearly delineated (5.4 b). In the presence of malignancy, however, this organized structure is distorted by the tumor and loses the clear delineation of mucosal, submucosal, and muscular layers. These findings mirror the differences in histology among the specimens; in contrast to the ordered layering of the normal colonic wall (images 5.4 d), the tumors appear disorganized with destruction of the underlying colonic architecture (images 5.4 h).

Additionally, the rHbT maps computed from coregistered PAT/US images of benign regions show significantly lower rHbT signals (5.4 c) than maps from the malignant lesions (5.4 g). As demonstrated in these representative images, normal tissue was found to have almost no detectable rHbT signal. In contrast, malignant tissue showed much higher concentrations of hemoglobin around the tumor bed. Again, these findings appear corroborated by histologic examination. In comparison to the relative paucity of large blood vessels in normal tissue, the malignancies were more vascular and contained large blood vessels (red arrows in images 5.4 h).

It is interesting to note that fatty tissues have limited PAT signals in the outer portions of the specimens. This is not surprising since we are specifically targeting hemoglobin – which is not concentrated in fatty tissue – as our chromophore of interest, and therefore we image within the 730-830 nm wavelength range. Additionally, all PAT images are displayed with the same dynamic range of -10 dB, so anything below this level is not displayed. The fatty tissue, due to its lack of vascular structures, falls below this range.

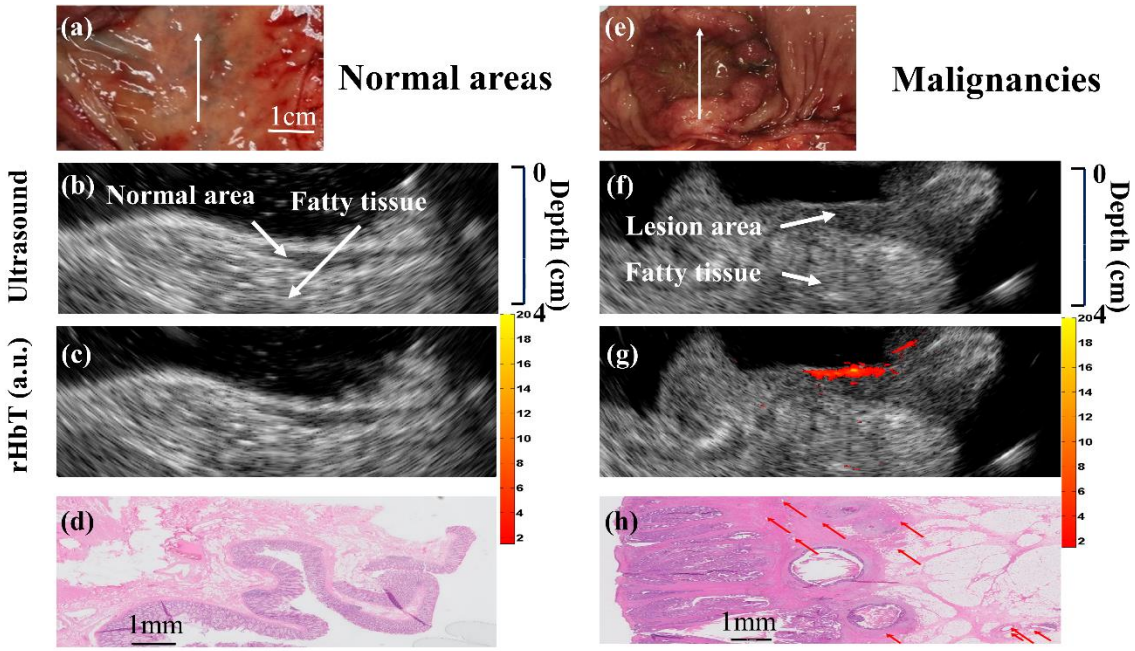

Figure 5.4: Color photograph, US image, rHbT map, and H&E image from representative areas of (a)-(d) a normal region and (e)-(h) a malignant region of pretreatment colorectal cancer tissue. Red arrows identify blood vessels within the histologic images.

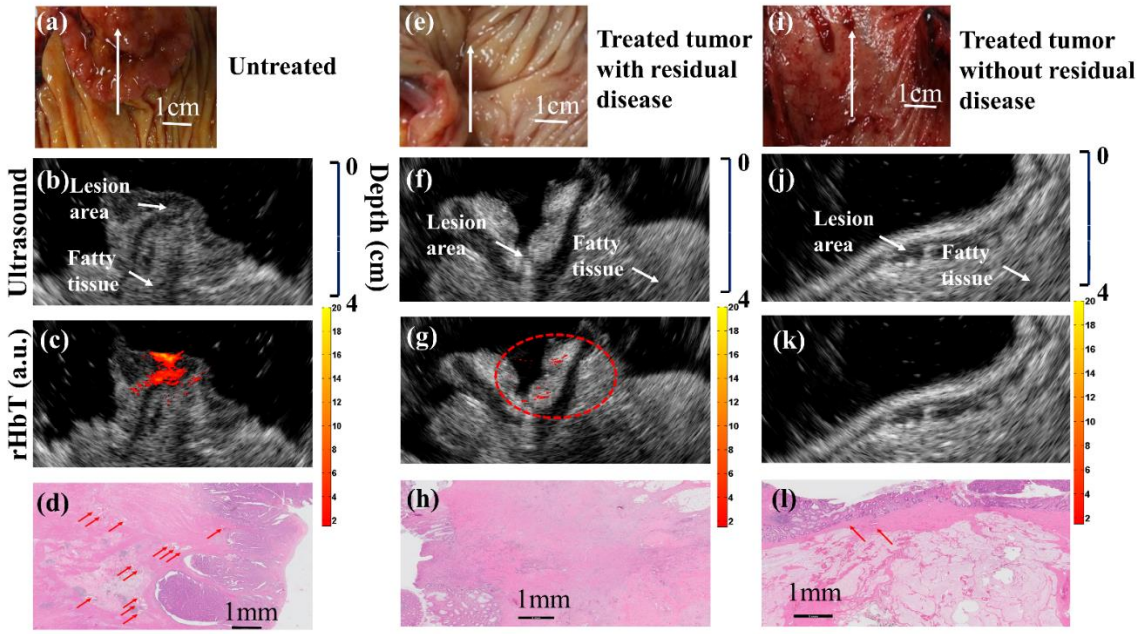

Figure 5.5: Color photograph, US image, rHbT map, and H&E image from representative areas of (a)-(d), a pretreatment colorectal cancer, (e)-(h) a post-treatment colorectal cancer tissue with residual disease, and (i)-(l) a post-treatment colorectal cancer tissue without residual disease.

5.3.2 Evaluation of Treated Tumors

Figure 5.5 shows corresponding images from a representative untreated colon cancer sample (5.5 a - 5.5 d), a colon tumor treated with preoperative chemotherapy (5.5 e – 5.5 h), and a rectal malignancy that received radiation and chemotherapy prior to surgical resection (5.5 i - 5.5 l). The untreated tumor displays findings consistent with other untreated colorectal cancers: loss of layered wall structure, increase in rHbT signal, and increased vascularity throughout the tumor bed. However, treatment appears to reverse these changes. For example, the PAT signal appears to diminish with chemotherapy (5.5 g) and even disappear altogether with complete destruction of the tumor (5.5 k). Additionally, ultrasound imaging demonstrates a return to the normal wall structure with complete tumor destruction (5.5 j). Histologic comparison among specimens also

correlates with these findings; a reduction in vasculature along with return to a semi-organized mucosal structure is noted throughout the treated specimens.

5.3.3 Quantitative Analysis

In addition to the above qualitative comparisons, we extracted features from 23 non-overlapping areas obtained from 12 untreated malignant tumors, 6 polyps, 3 post-treatment complete responders or patients with no residual tumor following prior polypectomy, and 2 post-treatment non-responders. We also extracted features from 18 normal non-overlapping areas from specimens of normal regions. Thus a total of 41 non-overlapping regions were used. Note that each non-overlapping area was obtained from each separate sample. These regions were identified by the attending pathologist.

Figure 5.6 (a-g) shows the boxplots of the seven features calculated from the functional, spectral and image differences between the different types of colorectal tissue. The n number given in the plots corresponds to the total number of areas. The malignant regions demonstrated elevated rHbT, 0.5MHz SI (PAT) and 0.5MHz SI (US) score smaller (less negative) compared to normal and precancerous regions. For SS (PAT), the malignant regions score below normal and precancerous polyps. Treated tumors with complete response were found to have similar scores to normal tissue, while treated regions with residual cancer have scores similar to untreated cancers. Due to the limited number of treated cancers, statistics were not performed for these two treated categories.

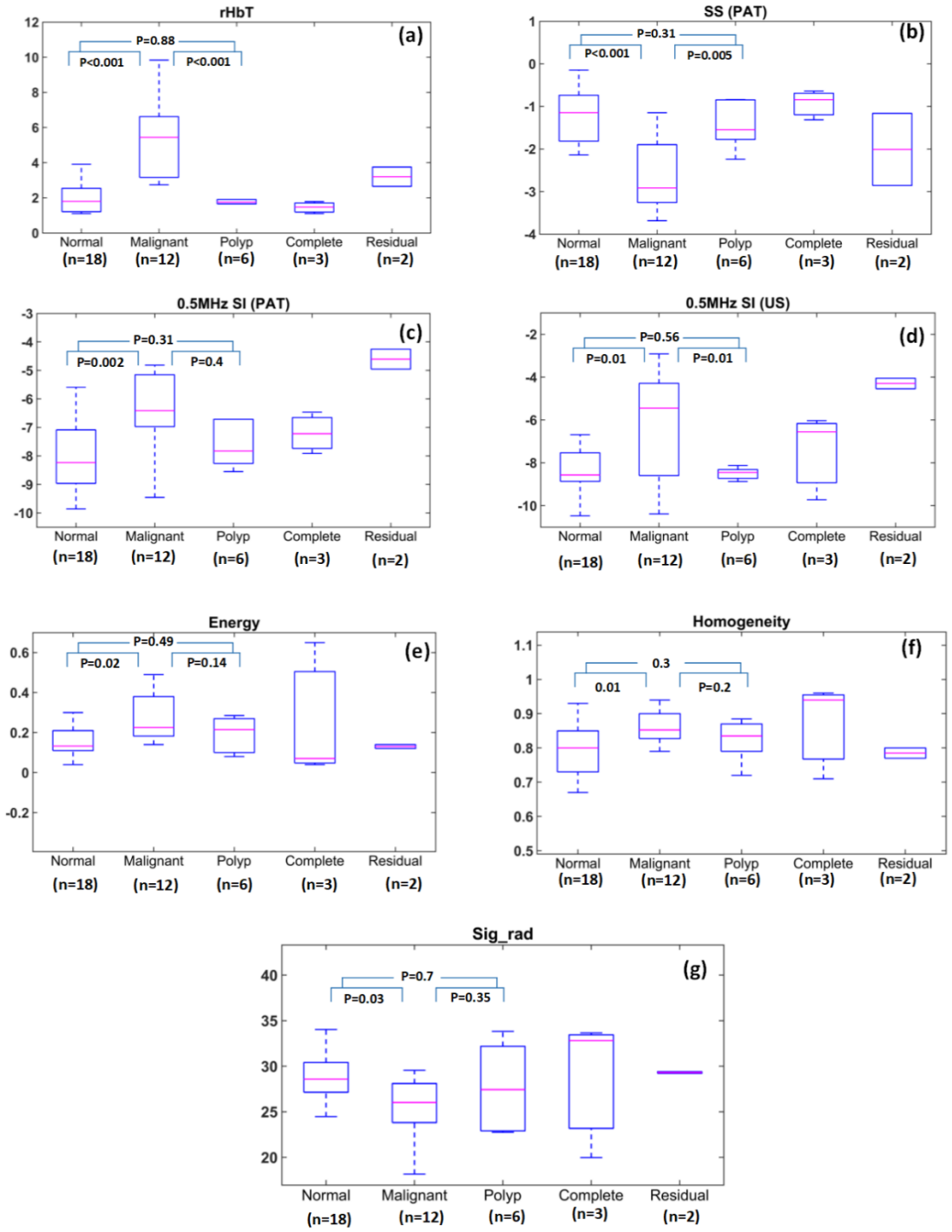

Figure 5.6: Boxplots of (a) total hemoglobin; (b) the mean spectral slope from PAT spectra; (c) 0.5 MHz spectral intercept from PAT spectra; (d) 0.5 MHz spectral intercept from US spectra; (e)

energy from the second order statistics of PAT images; (f) homogeneity from the second order statistics of PAT images; (g) standard deviation of the mean radon transform.

To distinguish untreated malignant from normal colon tissues, GLM and SVM classifiers were established. These classifiers were developed using the independent features with a p-value less than 0.05 between malignant and normal colon tissues. To determine if two features are independent, Spearman's correlation was calculated between each pair of features (Table 5.4). To train each classifier, we first used the feature with the lowest p-value and then added other features to the feature set one by one. We continued to include features to the feature set until no increase in the AUC value for the testing data set was observed. We found that when rHbT was included in the feature set, the best performance of both the GLM and SVM classifiers (the highest AUC value for the testing data set) was achieved when rHbT and 0.5MHz SI (PAT) were employed to train the classifier, although SS (PAT) has a lower p-value than 0.5MHz SI (PAT). Adding other features did not improve the AUC for the testing data set.

Table 5.4: The correlation between significant features used in this study

	SS (PAT)	**0.5MHz SI (PAT)**	**0.5MHz SI (US)**	**Homogeneity**	**Energy**	**Sig_rad**
rHbT	0.65	0.45	0.27	0.34	0.41	0.37
SS (PAT)		0.67	0.23	0.42	0.46	0.29
0.5MHz SI (PAT)			0.21	0.49	0.41	0.4
0.5MHz SI (US)				0.41	0.37	0.31
Homogeneity					0.79	0.91
Energy						0.82

Figure 5.7 shows the ROC curves and AUC values of the training (left) and testing (right) data sets using GLM (top row) and SVM (bottom row) classifiers. As shown in this figure, when the features set include just rHbT, the AUC values for the training and testing data sets are 0.95 and 0.93 for

both classifiers, respectively. Adding 0.5MHz SI (PAT) to the features set results in a significant improvement in the AUC values for both the training and testing data sets (0.97 and 0.95 for the training and testing data sets for both classifiers, respectively). The three image features (Sig_rad, Homogeneity, and Energy) did not improve the AUC values for either the training or testing data sets.

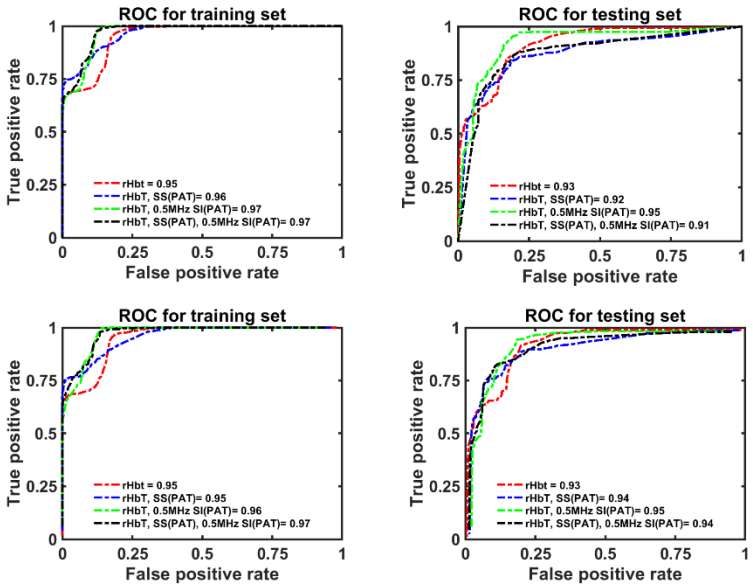

Figure 5.7: ROC curves and their associated AUC values for the training and testing data sets in the presence of rHbT in the feature set. (a), (b) GLM classifier performance. (c), (d) SVM classifier performance.

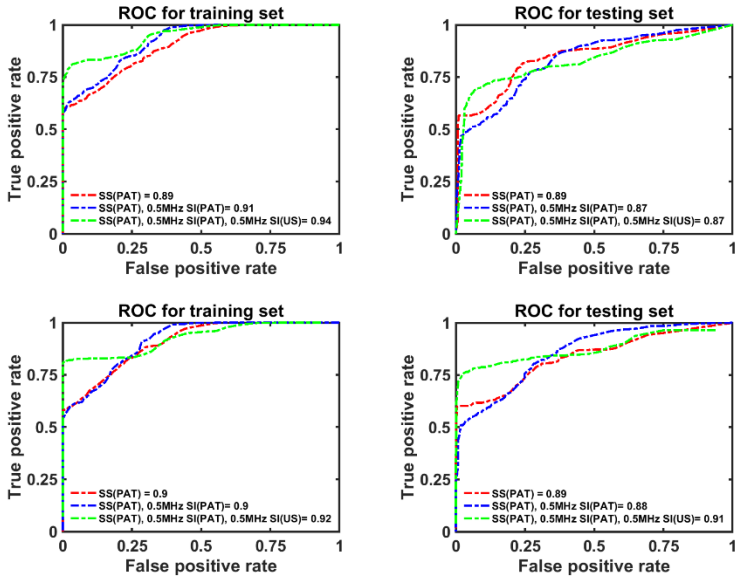

Figure 5.8: ROC curves and their associated AUC values for the training and testing data sets in the absence of rHbT in the feature set. (a), (b) GLM classifier performance. (c), (d) SVM classifier performance.

Finally, the performance of the GLM (top row) and SVM (bottom row) classifiers without rHbT (the single-wavelength model) are presented in Figure 5.8. Note that although the difference between some of the PAT image features in malignant and normal samples is statistically significant, none of these features improve the AUC for the testing data sets. The best performance of GLM classifier is achieved when the only spectral feature SS(PAT) is included in the feature set. The best performance of SVM classifier is achieved when the spectral features SS(PAT), 0.5MHz SI(PAT), and 0.5 MHz SI(US) are included in the feature set. The testing AUC in this case is 0.89 for the GLM classifier and 0.91 for the SVM classifier.

5.4 Discussion and Summary

In this pilot study of co-registered ultrasound and photoacoustic tomography, we found significant qualitative and quantitative differences between malignant tumors and normal tissue within human colorectal specimens. Specifically, the parameters rHbT, 0.5MHz SI (PAT), 0.5MHz SI (US), and SS (PAT) differ between the two tissue types imaged, suggesting that PAT may be able to differentiate malignant from normal tissue in the colon and rectum. Combined with the PAT system's tissue penetration depth of over 4 to 5 cm (depending on the background tissue optical properties), these findings suggest that PAT may be able to augment extant radiographic technology in the diagnosis, management, and surveillance of colorectal cancer.

As demonstrated by Guan et al [27] and Ronald [28], PAT spectral features are related to the size and concentration of the optical absorbers. The slope decreases (more negative) as PA absorber sizes increase and the intercept increases (less negative) as the sizes and concentrations of the absorbers increase. We believe that malignant lesions have larger absorber sizes and higher concentrations compared with normal colorectal tissues due to their increased microvessel networks. As introduced by Lizzi and co-workers [29], US spectral slope depends on acoustic scatter size while spectral intercept depends on scatter sizes, concentrations and acoustic impedances of tissue scatter matrix. These parameters have been found valuable to characterize liver, eye [29], prostate [30], and breast lesions [31]. We believe that the distorted tissue architecture and abundance of cancerous cells are the source of the US spectral contrast between malignant and normal colorectal tissues. However, the findings of the PAT and US spectral features of colorectal diseases may or may not be applicable to diseases of other organs.

Several technical limitations must be considered with our data. First, we imaged colorectal specimens obtained from routine surgeries and these tissues were typically with large pathologic components that often appeared malignant by visual inspection after specimens were open. These lesions may or may not need advanced PAT and US features for diagnosis. However, these lesions are excellent examples for identifying PAT and US feature characteristics that differ between cancerous and normal tissue. With this information known, we can target less obvious lesions as we look to test the utility of the device in identifying cancer margins and residual tumors after chemo-radiation treatment in patient.

The second limitation of this study is the low image resolution of our prototype. The image resolution is only ~250 μm due to the commercial endo-cavity ultrasound transducer array (6 MHz central frequency, 80% bandwidth). Because this resolution will impact future clinical applications of the device, we plan to upgrade the ultrasound system with a transducer array of more than 15 MHz to address this problem in future studies. Third, hemoglobin oxygen saturation (sO2) was not calculated in this study since all specimens were imaged after resection, resulting in significantly altered oxygen saturation compared to normal living tissue. sO2 is a significant biomarker for characterization of cancer [11] and assessment of treatment response.

Thirdly, the limited sample size could lead to overfitting of the classifiers if enough care is not taken to develop the classifiers. As a rule of thumb, overfitting is least possible to occur if the number of samples is 10 times or higher than the number of independent predictors [32]. Based on this rule, as we have a total of 30 samples (18 normal colorectal tissues and 12 untreated malignant colorectal tissues) for ROC analysis, the maximum number of the predictors that should be used to avoid overfitting would be three. Figure 5.7 shows that when rHbT is present in the feature set, the best performances of both GLM and SVM are achieved when rHbT and 0.5MHz SI (PAT) are

the only features used to train the classifiers. Adding SS (PAT) to these feature set neither changes the value of the AUC for training data sets, nor increases the AUC for the testing data set. Moreover, when rHbT is not included in the feature set, employing the combination of SS (PAT), 0.5MHz SI (PAT), and 0.5MHz SI (US) features for developing the classifiers would result in the best performance of SVM classifier and SS (PAT) only would result in the best performance of GLM classifier (Figure 5.8). While adding Sig_rad increases the AUC value for the training data set, it decreases the AUC values for the testing data set in both classifiers. This would mean that our classifiers have most probably been overfitted when four features have been used. In this study, to further protect our classifiers from overfitting, repeated rounds (100 times) of cross validation were applied by randomly selecting 2/3 of the samples for training and 1/3 of the samples for testing. The average ROC and AUC values were reported as the results.

In summary, a real-time co-registered PAT/US system was used to image and characterize colorectal masses *ex vivo* in this pilot study. 23 colon and rectum samples (19 colon and 4 rectum) were imaged, rHbT was computed from 4 wavelength data, and seven quantitative features were extracted from PAT and US power spectra and images. In pre-treated malignant colorectal tumors, we found the cross-section structure to be highly disorganized with a significantly higher rHbT concentration compared to normal and precancerous regions. We performed classifications on the malignant and normal colon regions using GLM and SVM classifiers both with and without tHb in the feature set. When rHbT was employed to construct the classifiers with 0.5 MHz SI (PAT), GLM and SVM classifiers achieved optimal AUC values for the training and testing data sets (0.97 and 0.95, respectively). The small number of treated tumors included in this dataset limits the statistical power of the analysis, but the functional, spectral and image parameters do appear more similar to normal colorectal tissue in tumors that have experienced complete responses

compared to partial responders. These results indicate potential of using PAT/US for future cancer screening and post-treatment surveillance of the colon and rectum. Moving forward, we plan to increase the resolution of our system by using a high frequency US array and then adapt the technology to an endo-rectal probe, which will allow us to test the functional and spectral feature differences in in *vivo* human tissue.

5.5 Develop a High-frequency Ultrasound Transducer Array based PAT/US Imaging System to Improve Spatial Resolution

5.5.1 Significance

Previously, we have performed a pilot assessment of human colorectal masses, using a co-registered PAT/US imaging system. These results indicate potential of using PAT/US for future cancer screening and post-treatment surveillance of colon and rectum. The image resolution of the current system is low (~ 250 μm axial resolution) due to the commercial endo-cavity ultrasound transducer array (6 MHz central frequency, 80% bandwidth). To solve the problem of image resolution, we decoded the pin configuration of a high-frequency transducer array (15 MHz central frequency, 9-18 MHz bandwidth) and adapted it to our home-made 128 channels ultrasound pulsing and receiving system (sampling rate: 40 MHz) to perform high frequency PAT/US imaging. To futhter improve the performance of photoacoustic data acquisition suitable for high-frequency transducer array, we are building a 64-channel FPGA based high frequency photoacoustic imaging system with a sampling rate of 80 MHz and signal-to-noise ratio (SNR) of

40 dB, and adapting this system to an endo-rectal probe with a side-firing fiber tip for *in-vivo* patient study.

5.5.2 Approach

Figure 5.9 shows the setup of the high-frequency PAT/US system. A single Nd:YAG and Ti:Sapphire 2-in-1 tunable laser was used to deliver pulsed laser light (Symphotic TII, LS-2145, 10 Hz repetition rate, 8-30 ns pulse duration, output fluence < 25 mJ/cm^2 in the 700-800 nm wavelength range). The single output light beam passed through a cylindrical lens array and was split into four beams and finally coupled into four 1-mm core multi-mode fibers for tissue illumination. A 3D-printed fiber holder was mounted to the high-frequency linear transducer array (Fujifilm, VisualSonics MS-200, 15 MHz central frequency, 9-18 MHz bandwidth) with a dark-field scheme. One stepper motor was used to acquire several sequential B-Scans with a step size of 2.5 mm. For each position, we mechanically tuned four wavelengths (730, 780, 800, 830 nm) and recorded corresponding PAT/US images to calculate the relative total hemoglobin concentration of regions of interest (ROIs). A home-made 128 channel US pulsing and receiving system was used to acquire the images [33].

We also evaluated the spatial resolution of this high-frequency PAT/US imaging system, as shown in Figure 5.10. The lateral and axial resolution were measured using a 250 μm black thread and 780 nm light. The black thread was placed perpendicular to the imaging plane at the zero degree position and worked as a point source. The PAT signal coming from the black thread was measured after the thread was put inside a water tank at ~ 2 cm depth. Then, the FWHM was calculated from the fitted Gaussian curve after deconvolution with the transfer function of the transducer.

As shown in Figure 5.10, we achieved a lateral resolution of ~ 150 μm and axial resolution of ~ 120 μm. Also we imaged a post-treated human rectal tissue (non-responder, grade 3, 1.5 cm cancer, more tumor at deep margin), as shown in Figure 5.11. From the pure ultrasound image, a clear layer structure of the rectum wall in the normal area is observed, although we still cannot differentiate the sublayers, such as the mucosa and submucosa, due to the low sampling rate of the current US system (40 MHz sampling rate). From the PA image, there is a relatively dense hemoglobin distribution within the rectum wall structure area. These findings appear correlated with the histology exam. The H&E shows the ordered rectum wall layer structures in that location. We are working on upgrading the ultrasound pulsing and receiving system with a higher sampling rate (≥ 80 MHz).

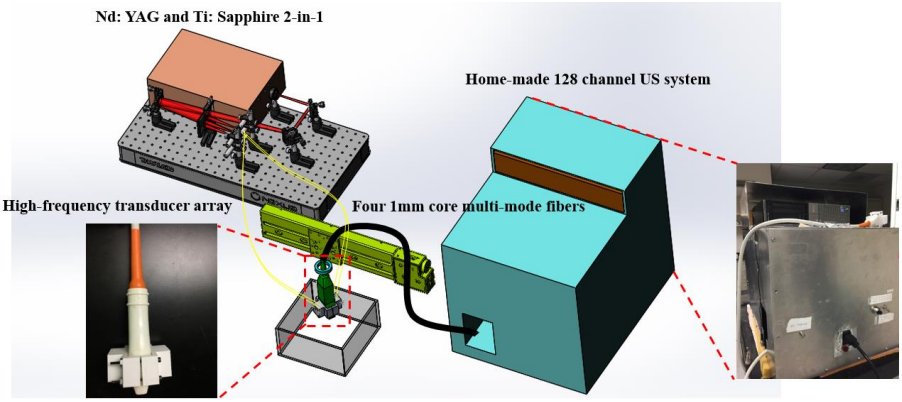

Figure 5.9: Setup of high-frequency PAT/US imaging system.

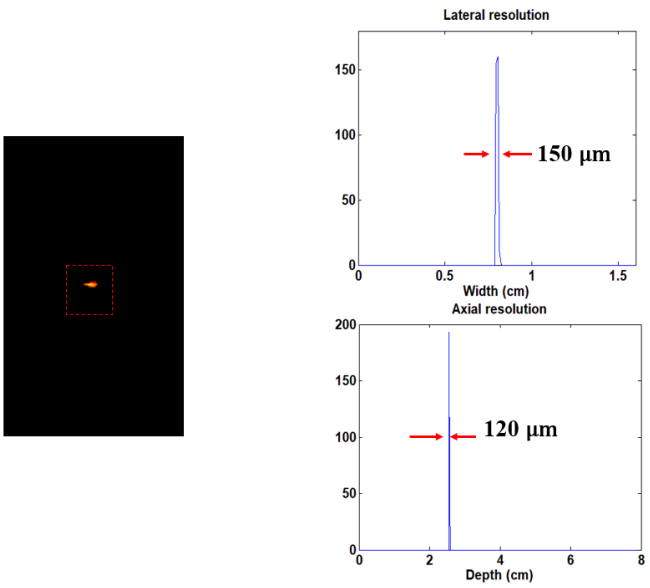

Figure 5.10: Spatial resolution evaluation.

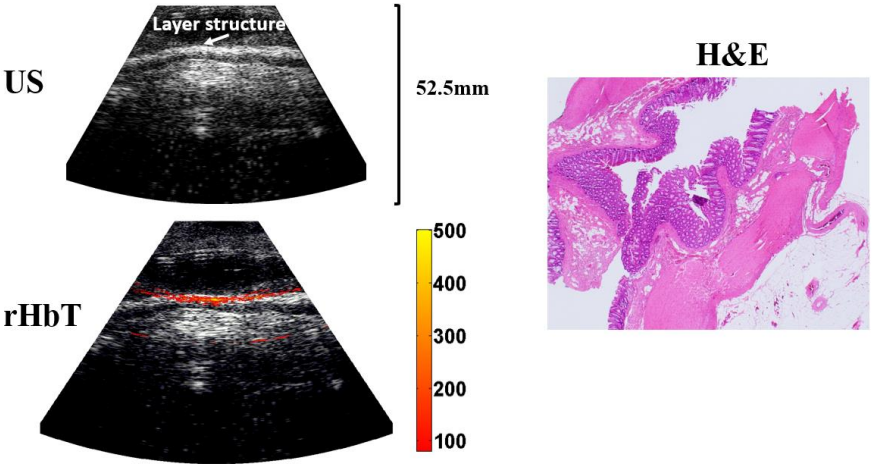

Figure 5.11: Post-treated human rectum sample imaging (normal area).

For the FPGA based high frequency photoacoustic imaging system part (Figure 5.12), 8 ADC boards (AFE5807EVM) and 2 FPGA control boards (Xilinx Artix 7) were employed. We used another FPGA board (Intel Cyclone V) to generate an external 80 MHz clock to trigger the sampling of the ADC boards. To move to an *in-vivo* patient study, a commercial endo-rectal probe (BK Medical 8836) was sandwiched between two side firing fiber tips. To make the side firing

fiber tip, we used a buffer wheel to polish the 1 mm core multi-mode fiber. We could adjust the curvature of the concave surface to adjust the length of the side illumination area. We also designed a 3D hand-held rotating platform combined with the rectal probe to perform volumetric PAT/US imaging.

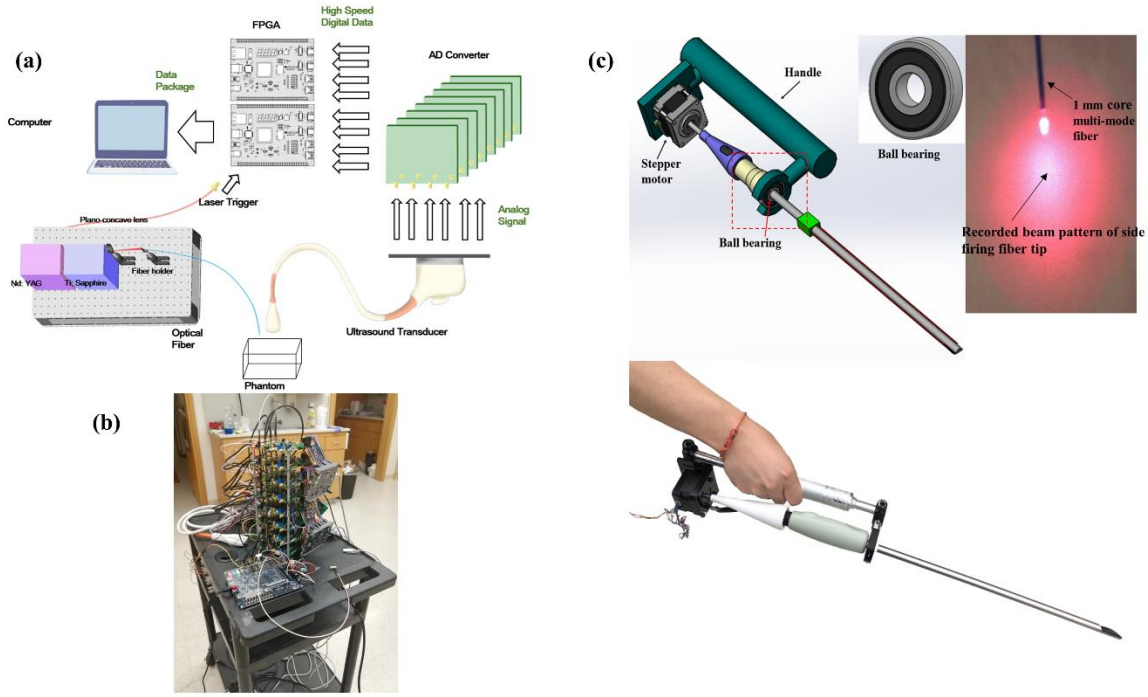

Figure 5.12: (a) Schematic diagram of FPGA based high-frequency photoacoustic imaging system; (b) photograph of the system; (c) volumetric endo-rectal imaging probe with side-firing fiber tips.

Figure 5.13 also shows the LABVIEW based control software for the high-frequency photoacoustic imaging system. We control probe rotation through LABVIEW interface for Arduino toolkit and control the data acquisition from two FPGA boards to PC by controlling FTDI USB chip inside the FPGA boards through FTD2XX.dll API. With this control software, we can automatically rotate the probe to several positions and acquire the PA raw data from 64 channels simultaneously for each position.

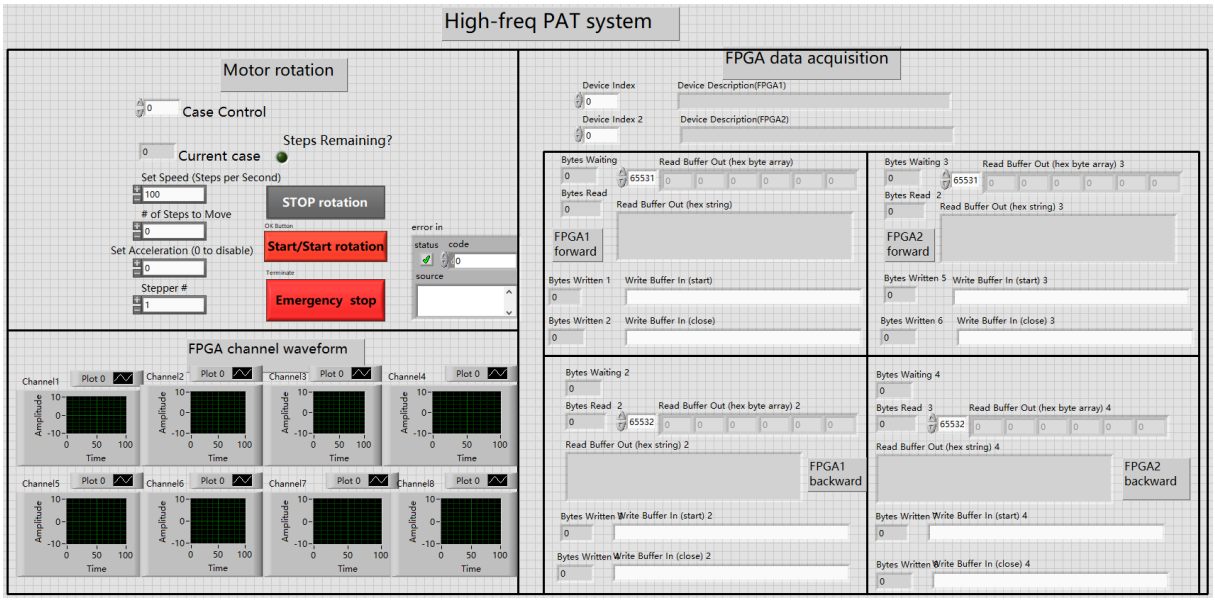

Figure 5.13: LABVIEW based control software for the high-frequency photoacoustic imaging system.

References

1. L. V. Wang et al., “Photoacoustic tomography: in vivo imaging from organelles to organs,” science, 335(6075), 1458-1462 (2012).

2. N. Weidner et al., “Tumor angiogenesis and metastasis—correlation in invasive breast carcinoma,” New England Journal of Medicine, 324(1), 1-8 (1991).

3. P. Vaupel et al., “Blood flow, oxygen and nutrient supply, and metabolic microenvironment of human tumors: a review,” Cancer research, 49(23), 6449-6465 (1989).

4. M. Hockel et al., “Tumor hypoxia: definitions and current clinical, biologic, and molecular aspects,” Journal of the National Cancer Institute, 93(4), 266-276 (2001).

5. Y. Yuan et al., “Preclinical photoacoustic imaging endoscope based on acousto-optic coaxial system using ring transducer array. Optics letters, 35(13), 2266-2268 (2010).

6. X. Leng et al., “Feasibility of co-registered ultrasound and acoustic-resolution photoacoustic imaging of human colorectal cancer,” Biomedical optics express, 9(11), 5159-5172 (2018).

7. H. S. Salehi et al., “Coregistered photoacoustic and ultrasound imaging and classification of ovarian cancer: ex vivo and in vivo studies,” Journal of biomedical optics, 21(4), 046006 (2016).

8. T. Wang et al., “Characterization of ovarian tissue based on quantitative analysis of photoacoustic microscopy images,” Biomedical optics express, 4(12), 2763-2768 (2013).

9. H. Li et al., “Utilizing spatial and spectral features of photoacoustic imaging for ovarian cancer detection and diagnosis,” Journal of biomedical optics, 20(1), 016002 (2015).

10. T. Wang et al., “A low-cost photoacoustic microscopy system with a laser diode excitation,” Biomedical optics express, 5(9), 3053-3058 (2014).

11. S. Nandy et al., “Evaluation of ovarian cancer: initial application of coregistered photoacoustic tomography and US,” Radiology, 289(3), 740-747 (2018).

12. G. Yang et al., “Optimized light delivery probe using ball lenses for co-registered photoacoustic and ultrasound endo-cavity subsurface imaging,” Photoacoustics, 13, 66-75 (2019).

13. G. Yang, “Co-registered photoacoustic and ultrasound real-time imaging of colorectal cancer: ex-vivo studies,” in Photons Plus Ultrasound: Imaging and Sensing 2019, Proc. SPIE 108784K, (2019) [doi:10.1117/12.2510914].

14. R. L. Siegel et al., “Colorectal cancer statistics, 2017,” CA: a cancer journal for clinicians, 67(3), 177-193 (2017).

15. American Cancer Society, “Cancer Facts & Figures,” American Cancer Society, Atlanta, Ga, USA (2014-2016).

16. J. Pan et al., “Colonoscopy reduces colorectal cancer incidence and mortality in patients with non-malignant findings: a meta-analysis,” The American journal of gastroenterology, 111(3), 355 (2016).

17. Y. Zeng et al., “The Angular Spectrum of the Scattering Coefficient Map Reveals Subsurface Colorectal Cancer,” Scientific reports, 9(1), 2998 (2019).

18. T. Wang et al., “Label-free biomolecular imaging using scanning spectral interferometry,” Chinese Optics Letters, 11(11), 111102 (2013).

19. S. P. Raman et al., “Evolution of imaging in rectal cancer: multimodality imaging with MDCT, MRI, and PET,” Journal of gastrointestinal oncology, 6(2), 172 (2015).

20. E. Al-Sukhni et al., “Diagnostic accuracy of MRI for assessment of T category, lymph node metastases, and circumferential resection margin involvement in patients with rectal cancer: a systematic review and meta-analysis,” Annals of surgical oncology, 19(7), 2212-2223 (2012).

21. S. P. Hiotis et al., “Assessing the predictive value of clinical complete response to neoadjuvant therapy for rectal cancer: an analysis of 488 patients,” Journal of the American College of Surgeons, 194(2), 131-135 (2002).

22. A. Mostafa, “Dual-mode photoacoustic and ultrasound system for real-time in-vivo ovarian cancer imaging,” in Photons Plus Ultrasound: Imaging and Sensing 2018, Proc. SPIE 104944K, (2018) [doi:10.1117/12.2291055].

23. H. S. Salehi et al., “Design of miniaturized illumination for transvaginal co-registered photoacoustic and ultrasound imaging,” Biomedical optics express, 5(9), 3074-3079 (2014).

24. E. Amidi et al., “Classification of human ovarian cancer using functional, spectral, and imaging features obtained from in vivo photoacoustic imaging,” Biomedical optics express, 10(5), 2303-2317 (2019).

25. E. Amidi, “Low-cost ultrasound and optical gelatin-based phantoms,” in Photons Plus Ultrasound: Imaging and Sensing 2019, Proc. SPIE 108784A, (2019) [doi:10.1117/12.2507938].

26. R. M. Haralick et al., “Textural features for image classification,” IEEE Transactions on systems, man, and cybernetics, (6), 610-621 (1973).

27. G. Xu et al., “Photoacoustic spectrum analysis for microstructure characterization in biological tissue: A feasibility study,” Applied Physics Letters, 101(22), 221102 (2012).

28. R. Kumon, “Frequency-domain analysis of photoacoustic imaging data from prostate adenocarcinoma tumors in a murine model,” Ultrasound in Medicine & Biology, 37(5), 834-839 (2011).

29. FL. Lizzi et al., “Relationship of ultrasonic spectral parameters to features of tissue microstructure,” IEEE Transactions on ultrasonics, ferroelectrics, and frequency control, 34(3), 319-329 (1987).

30. E. Feleppa et al., “Ultrasonic spectral-parameter imaging of the prostate,” imaging systems and technology, 8(1), 1098 (1997).

31. H. Tadayyon et al., “Quantitative ultrasound characterization of locally advanced breast cancer by estimation of its scatterer properties,” Med Phys, 41(1), 012903 (2014).

32. J. Concato et al., “The risk of determining risk with multivariable models,” Ann Intern Med, 118 (3), 201-210 (1993).

33. Alqasemi, Umar, et al. "FPGA-based reconfigurable processor for ultrafast interlaced ultrasound and photoacoustic imaging." IEEE transactions on ultrasonics, ferroelectrics, and frequency control 59.7 (2012): 1344-1353.

Chapter 6: Photoacoustic laser effects in live mouse blastocysts: pilot safety studies of DNA damage from photoacoustic imaging doses

6.1 Introduction

The photoacoustic effect – the conversion of light to sound – was first described by Bell in the late 1800's [1]. With the advances of lasers, ultrasound transducers, and tomographic reconstruction techniques, photoacoustic imaging (PAI) has become one of the fastest growing fields in biomedical imaging [2, 3]. In PAI, nanosecond laser pulses are used as probing energy. The laser induces photon absorption and thermoelastic expansion in the examined tissue, which results in ultrasound waves. Thus, PAI reveals biological tissue optical contrast with ultrasound resolution. Of significance, physiological parameters, such as relative total hemoglobin concentration and oxygen saturation, could be defined with PAI.

The potential use of PAI on reproductive organs such as the ovary and uterus raises a question about the effect of its exposure on embryos. The effects of a photoacoustic laser on preimplantation embryos, to our knowledge, have not been reported. Previous studies have reported that intense lasers can induce alterations in DNA, mitochondria, spindle apparatus as well as cell metabolism and survival [4-8]. Yet, the laser parameters used in those studies differ significantly from the laser parameters used in photoacoustic imaging systems. In addition, responses of cell lines to the laser used in these studies are expected to differ from the responses of embryos. In order to establish a stage-specific safety threshold of PAI on early embryos, studies need to be done with photoacoustic laser parameters during specific stages of preimplantation embryo development

such as the blastocyst stage. To the best of our knowledge, this study is the first to examine laser-induced DNA damage on pre-implantation mouse embryos using photoacoustic imaging lasers.

6.2 Methods

6.2.1 Mouse Embryo Sources

Frozen two-cell mouse embryos were purchased from Embryotech Laboratories. Embryos were thawed according to the manufacturer's protocol and subsequently cultured for 72 hours in vitro in 50-μL drops of Continuous Single Culture-NX complete medium (Fujifilm Irvine Scientific) under light mineral oil (Fujifilm Irvine Scientific). Embryos were group cultured at a maximum density of 10 embryos per drop of medium in ASTEC IVF Cube low oxygen incubators (ASTEC Co. Ltd.) at 37°C and 6% CO_2, 5% O_2, and 89% N_2. Our average mouse blastocyst formation rate is approximately 89%. The study was exempted by the Institutional Animal Care and Use Committee.

6.2.2 Laser Exposure

The embryos were suspended in 30 μL of medium in Eppendorf polymerase reaction (PCR) tubes for laser exposure. The 5-minute 15-Hz and 10-minute 15-Hz laser doses represent the expected doses in typical human reproductive tissue imaging studies. The 1-minute 1-kHz dose represents a level of exposure that is significantly above that which may be used clinically. None of the control blastocysts were exposed to the laser. Test samples were exposed to the laser at 780 nm for 5 minutes or 10 minutes by delivering pulsed laser light through one 1.5-mm core multimode optical fiber (FP1500ERT, 0.5 NA, Thorlabs) as shown in Figure 6.1. The light photons penetrate through the Intralipid fat emulsion (Baxter) solution layer inside the three-dimensionally printed water tank and the culture medium in the PCR tubes, and finally reach the embryos on the bottom

of the tubes as shown in Figure 6.1. The 10-mm-thick calibrated Intralipid solution layer with an absorption coefficient (μ_a) of 0.02 cm^{-1} and reduced scattering coefficient (μ_s') of 4 cm^{-1} is used to mimic a soft tissue layer between the probe and the embryos. One plastic film without optical attenuation on the bottom of water tank is sandwiched by the Intralipid solution layer and the culture medium layer with good contact on both sides. The laser used for illumination consists of a Ti: Sapphire (LS-2134, Symphotics TII Corp.) optically pumped with a Q-switched Nd: YAG laser (LS-2122, Symphotics TII Corp., 10-ns pulse duration, 15-Hz pulse repetition rate) [9,10]. The fiber tip output power is 0.55 mJ, which corresponds to the maximum permissible exposure (MPE) (~ 28 mJ/cm^2 at 780 nm) [11] based on simulations and measurements. The fluence level delivered to the Intralipid solution layer surface was experimentally measured as follows: The beam output from the fiber tip was Gaussian shaped and its diameter at the point where its peak intensity drops to 1/e was measured using a variable iris diaphragm and energy meter which corresponds to approximately 63.2% of the energy from the fiber tip. The beam area used for calculating the fluence was measured to be the iris aperture that allowed 63.2% of the light energy to pass through it, when the beam was centered on the iris [12]. Fluence equals the total input energy divided by the circular area calculated by the detector radius. In experiments, the required laser input energy reaching surface MPE (~ 28 mJ/cm^2 at 780 nm) is 0.55mJ. We also used another Nd:YAG laser with a much faster repetition rate (DPS-1064-Q, CNI Laser.com; 1064 nm, 1-kHz repetition rate, 7-ns pulse duration) . The fiber tip output power is 2 mJ, which corresponds to the MPE (~ 100 mJ/cm^2 at 1064 nm) [11] based on simulations and measurements.

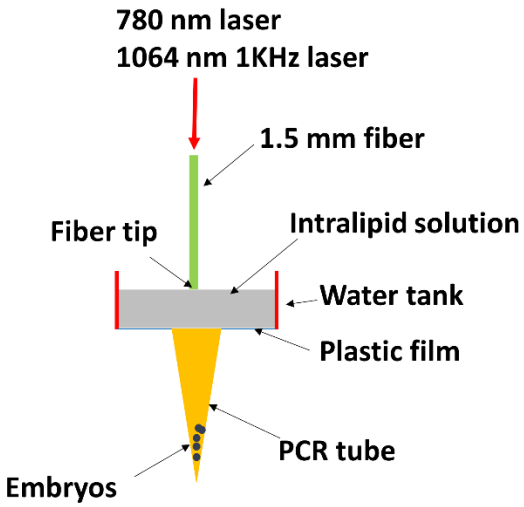

Figure 6.1: Light path from the fiber tip to the embryos. Embryos inside the polymerase chain reaction tube were exposed to the 15-Hz laser at 780 nm for 5 minutes and 10 minutes, and 1-kHz laser at 1064 nm for 1 minute by delivering pulsed laser light through one 1.5-mm optical fiber.

6.2.3 Staining Procedure

After the test groups were exposed to the laser, all groups of embryos were stained for imaging. Embryos were suspended on negatively charged microscope slides within a hydrophobic PAP pen circle. Embryo presence was verified using an Olympus SZX12 microscope (Olympus).

Medium was drawn off the slides, and the embryos were subsequently fixed in a 4% paraformaldehyde (PFA) solution and incubated at room temperature in a humidified chamber for 25 minutes. The slides were stored in a -20°C freezer overnight after fixation.

Slides were warmed and embryos were resuspended in 1xPBS. Embryos were incubated in a 1% Triton solution for 25 minutes at room temperature in a humidified chamber to allow

permeabilization of the cellular membranes. One slide was then treated with DNase and incubated for 10 minutes at 37°C in a humidified chamber to generate the positive control slide. The negative control slide was not exposed to the laser, but underwent the same terminal deoxynucleotidyl transferase dUTP nick end labeling (TUNEL) staining protocol as the other groups.

A TUNEL assay kit was used to identify locations of DNA damage within the blastocysts. The assay solution was prepared according to the manufacturer's specifications. Slides were incubated with TUNEL reagent in the dark for 1 hour in a 37°C incubator in a humidified chamber. The embryos were also incubated in a 4 μM To-Pro-3-Iodide nuclear staining solution at room temperature for 25 minutes in a humidified chamber.

After all staining procedures, excess liquid was removed and slides were sealed with a coverslip. Slides were stored at -4°C until imaging.

6.2.4 Blastocyst Microscopic Imaging

The mounted blastocysts were imaged by a confocal laser-scanning microscope (FV 1000, Olympus). The embryos were first located using the 10X objective, and then the 60X objective was used for imaging. The upper and lower bounds were found by adjusting the focus, and then five slices were taken to ensure that all cells contained within the embryo could be counted. The excitation wavelengths for TUNEL stain (TMR red) and To-Pro-3-Iodide are 589nm and 642nm, respectively, and the lasers available for use had wavelengths of 543nm and 633nm. The emission wavelengths of TMR red and To-Pro-3-Iodide are 615nm and 661nm, and the emissions were read at 568nm and 633nm, respectively.

6.2.5 Laser Damage Calculation

The cells with damaged DNA were then counted using the manual cell counter extension of ImageJ software (National Institutes of Health), which allows for moving between slices while maintaining one constant count and leaving tic marks to track previously counted cells. An example of how the cells were counted in the positive control can be seen in Figure 6.2. The To-Pro-3-iodide stain produced overexposed images, so the total number of cells could not be counted from the nuclear stain.

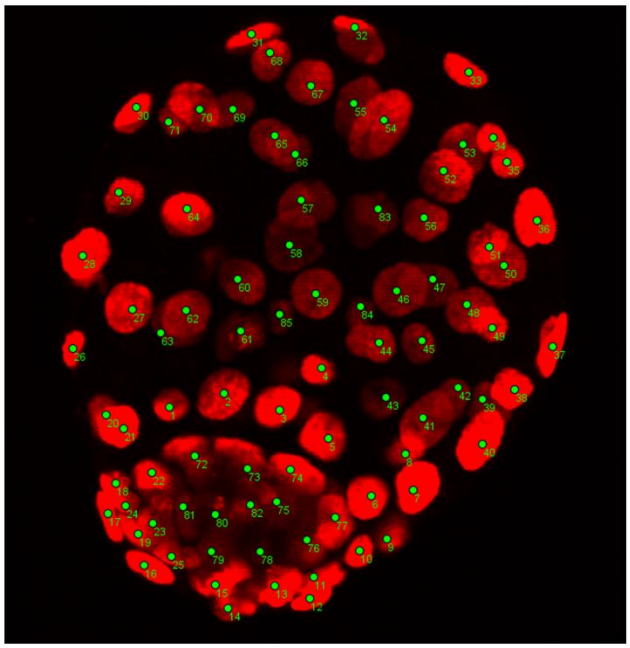

Figure 6.2: A positive control embryo showing the counting tick marks provided by ImageJ software.

6.2.6 Statistical Analysis

The mean and standard deviation of each of the five treatment groups were calculated based on the number of damaged cells counted using ImageJ. Since some cells had weak nuclear stains,

it was difficult to obtain the actual total cells to calculate the percentage of cell death, we counted total number of damaged cells from each group. A two-tailed, independent t-test was conducted to compare the total number of TUNEL positive nuclei in embryos that were or were not exposed to the laser. A value of $P < .05$ was considered statistically significant.

6.3 Results

6.3.1 Embryo Microscopic Imaging

The images shown in Figure 6.3 are examples of all three groups examined using the confocal microscope. Since the positive control embryos were treated with DNase, the cells within each embryo were damaged and were visualized as strong red fluorescence under the microscope. The gain on the TMR Red color of the TUNEL stain was left the same for all embryos in all trials, and used to determine if embryos incurred any DNA damage. The nuclear stain gain was also left the same between different embryos.

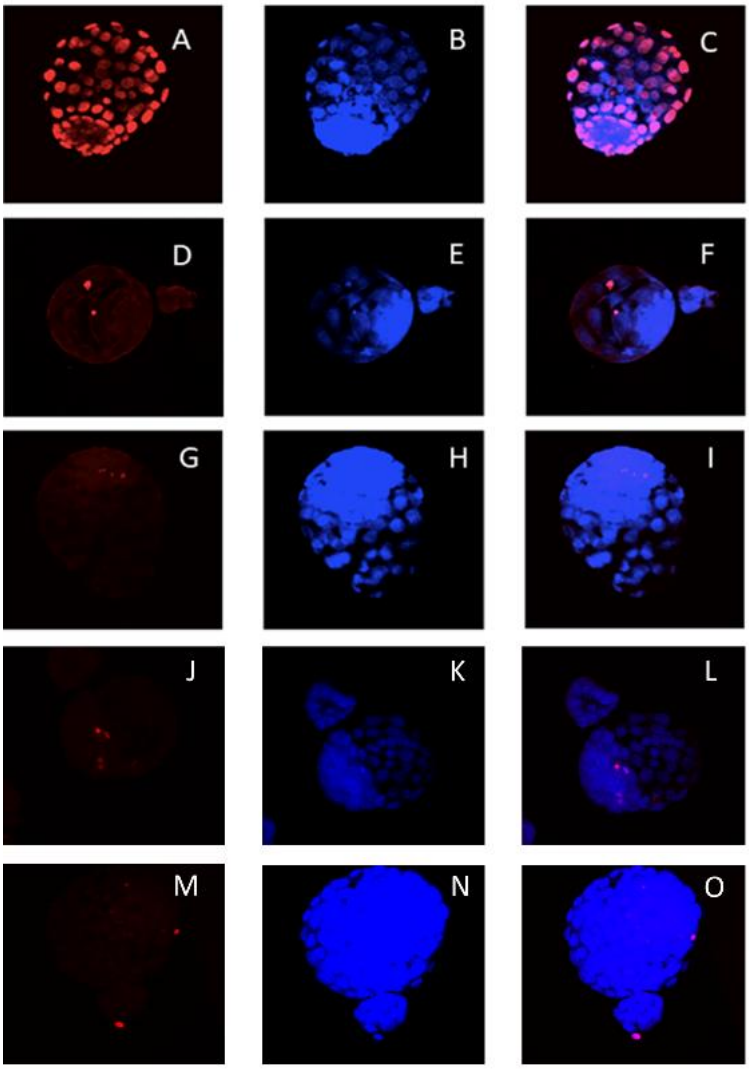

Figure 6.3: Stained images of (A) positive control (DNase Treated), TUNEL stain only; B) positive control, nuclear stain only; C) positive control, both stains; D) negative control (no laser exposure), TUNEL stain only; E) negative control, nuclear stain only; F) negative control, both stains; G) 5-minute 15-Hz laser-exposed, TUNEL stain only; H) 5-minute 15-Hz laser exposed, nuclear stain only; I) 5-minute 15-Hz laser-exposed, both stains; J) 10-minute 15-Hz laser exposed, TUNEL stain only; K) 10-minute 15-Hz laser exposed, nuclear stain only; L) 10-minute 15-Hz laser exposed, both stains; M) 1-kHz laser-exposed, TUNEL stain only; N) 1-kHz laser-exposed, nuclear stain only; O) 1-kHz laser-exposed, both stains.

6.3.2 Quantitative Analysis of Effects of Different Laser Doses

Once the embryo images were acquired, they were imported into and processed using ImageJ. The ImageJ manual cell counter was used to count the number of cells with DNA damage stained by TUNEL, and those counts were used for the statistical analysis.

The negative control blastocyst group (no laser exposure) (n=10) had 10.7 +/- 6.56 (mean +/- SD) TUNEL positive nuclei (Figure 6.4). The 5-minutes (n=16) and 10-minutes (n=9) 15-Hz laser-exposed groups had 11.25 +/- 5.66 and 12.89 +/- 4.26 TUNEL positive nuclei. The embryos exposed to the 1-kHz laser for 1 minute (n=14) had an average of 12.0 +/- 6.51 TUNEL-positive nuclei (P=not significant for all comparisons).

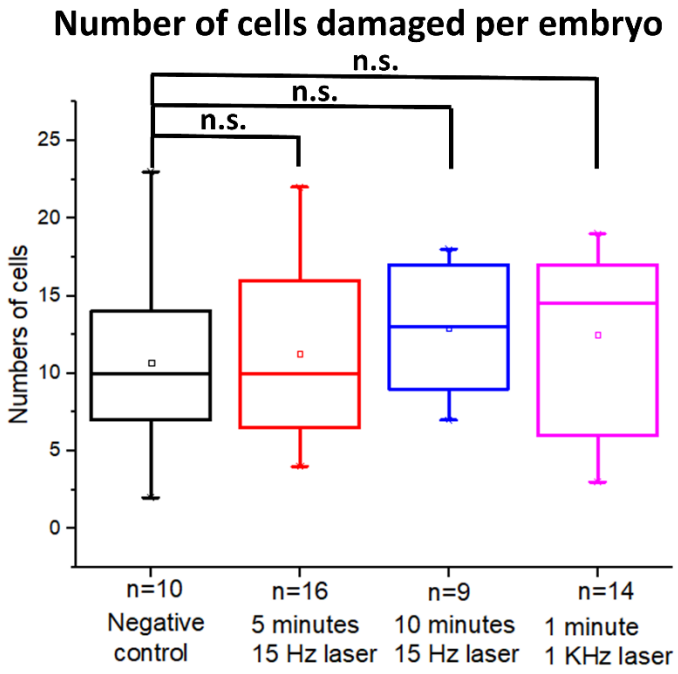

Figure 6.4: Number of cells per embryo with damaged DNA in all embryo groups. N it the number of embryos in each group.

6.4 Discussion

The results provide a preliminary safety assessment of PAI on mouse embryonic cells. We demonstrated that typical laser exposure times used for photoacoustic imaging do not induce increased cell death in mouse blastocysts. Our study targeted blastocysts with a defined set of laser parameters typically used in photoacoustic imaging clinical examinations. For example, in our transvaginal photoacoustic imaging study of ovarian cancer [9], the 15-Hz Q-switched Nd: YAG laser delivered laser energy transvaginally through optical fibers to illuminate ovarian tissue. An ultrasound transducer detected the photoacoustic signals and mapped out lesion relative total hemoglobin concentration and oxygen saturation. These measurements were successfully used to differentiate normal/benign ovarian masses from invasive epithelial cancers. Using this method, the laser fluence was controlled under MPE and the total scanning time to obtain the data was typically about 5 to 10 minutes. The results reported in this article suggest that the laser energy used and the scanning duration of 5 to 10 minutes are safe for a pregnancy during transvaginal PAI evaluation. In a rectal cancer study, the 1-kHz Nd:YAG laser delivered the laser energy endoscopically via an optical fiber to illuminate the rectum. The imaging head, consisting of the fiber and an ultrasound transducer, was used to screen for residual rectal cancer after neoadjuvant treatment. Within a 1-minute period of time, 60 imaging frames was acquired safely.

PAI's noninvasiveness, ease of integration with an ultrasound imaging system, and the potential of functional imaging have resulted in increasing interest from physicians to incorporate it into clinical practice. So far, human in vivo pilot studies using PAI have been mainly in the areas of oncology [9, 13-21] and inflammatory diseases [22, 23]. The largest clinical trial thus far was a 3-year prospective, multicenter study focused on breast cancer diagnosis. The study concluded that

combined ultrasound and photoacoustic imaging helps radiologists assess breast masses with increased specificity compared to gray scale ultrasound imaging alone [19].

To date, the use of PAI in the field of reproductive medicine has not been reported. The ability of PAI to be coupled with an ultrasound system will provide complementary information, such as vascular distribution and blood oxygen saturation, to the detailed imaging of the reproductive organ structures. This additional information may prove beneficial during in vitro fertilization (IVF) cycles. For example, during controlled ovarian stimulation, ultrasound is used to monitor follicular development. Also, during the oocyte retrieval procedure, physicians use ultrasound guidance to locate and to subsequently aspirate ovarian follicles. PAI, if incorporated, offers information beyond the location, size and number of follicles such as the degree of follicular vascularization. Studies have shown that follicles that appear similar in size and location can be surrounded by a drastically different vascular environment [24]. The additional information can be recorded and correlated with the developmental potential of eggs and thus serve as a potential biomarker of egg quality. Furthermore, PAI could be used to measure the uterine endometrium during IVF cycles, which might better define the optimal window of implantation of both fresh and frozen embryo transfer cycles.

The use of PAI in clinical settings will result in exposure of reproductive organs to photoacoustic laser rays. Current laser safety guidelines, however, are established based on ocular and skin damage [11, 25, 26]. Photoacoustic lasers affect sensitive organs beyond the eyes and skin, as in recent studies involving ovarian tissue [9]. To establish robust safety thresholds for PAI, studies using photoacoustic laser parameters on specific biological targets are necessary. A typical photoacoustic laser system consists of pulsed tunable near-infrared wavelength lasers with pulse width (<10 nanoseconds), fluence (20-100 mJ/cm^2 in the range of 700-1024 nm), and pulse

repetition frequency (several Hz to a few kHz) to achieve high-quality real-time images of tissue [27, 28]. In safety studies, tissues should be exposed to these laser parameters at time intervals that reflect the duration of laser exposure in clinical settings. Post-laser exposure tissue measurements such as cell death can help researchers and clinicians establish more informative safety thresholds for PAI. These thresholds are critical for successful translation of PAI into clinical use.

Although the pilot study gives a preliminary safety data of PAI on pre-implantation embryos, experiments need to be performed to establish a dose-response curve of laser exposure on the rate of cell death. For example, duration of exposure beyond 10 minutes for the 15-Hz laser needs to be explored with a set of laser parameters typically used in clinical settings. Further experiments are warranted to improve the experimental set up. For example, the embryos were centrifuged onto the tube bottom before laser exposure. The distribution of embryos on the tube bottom, however, are not well defined. Slightly non-uniformed embryo distribution will induce slightly unequal laser fluence onto each individual embryo. A safety threshold on duration of exposure could be established for this given set of laser parameters. Long-term embryo development, in addition to cell death following the time of exposure, should be assessed.

In summary, our study reports the first evidence that the laser-induced DNA damage to mouse embryos is negligible when the typical lasers used for photoacoustic imaging within a short exposure time (15-Hz laser of 5 and 10 minutes, with 1-kHz laser of 1 minute representing a high dose) are utilized. Further studies are warranted to establish a fuller safety profile for embryonic tissues and reproductive organs for this novel imaging technology.

References

1. Bell AG. The production of sound by radiant energy. Science 1881: 242–53.

2. Wang L V, Hu S. Photoacoustic tomography: in vivo imaging from organelles to organs. Science. 2012; 335: 1458–62.

3. Valluru KS, Wilson KE, Willmann JK. Photoacoustic imaging in oncology: Translational preclinical and early clinical experience1. Radiology. 2016; 280 :332–49.

4. Li S, Xia Q, Wang F, Yu X, Ma J, Kou H, et al. Laser Irradiation-Induced DNA Methylation Changes Are Heritable and Accompanied with Transpositional Activation of mPing in Rice. Front Plant Sci 2017; 8:363.

5. Zhu Y, He H. Molecular response of mitochondria to a short-duration femtosecond-laser stimulation. Biomed Opt Express 2017; 8:4965.

6. Buđa R, Vukušić K, Tolić IM. Dissection and characterization of microtubule bundles in the mitotic spindle using femtosecond laser ablation [Internet]. In: Methods in cell biology. 2017. p. 81–101.

7. Quero JMO, Villamandos RJG, Millan MM, Valenzuela JMS. The effect of helium-neon laser irradiation on in vitro maturation and fertilization of immature bovine oocytes. Lasers Med Sci 1995; 10:113–9.

8. Purschke M, Laubach H-J, Rox Anderson R, Manstein D. Thermal Injury Causes DNA Damage and Lethality in Unheated Surrounding Cells: Active Thermal Bystander Effect. J Invest Dermatol 2010; 130: 86–92.

9. Nandy S, Mostafa A, Hagemann IS, Powell MA, Amidi E, Robinson K, Mutch DG, Siegel C, Zhu Q. Evaluation of Ovarian Cancer: Initial Application of Coregistered Photoacoustic Tomography and US. Radiology 2018; 289: 740-747.

10. Yang G, Amidi E, Nandy S, Mostafa A, Zhu Q. Optimized light delivery probe using ball lenses for co-registered photoacoustic and ultrasound endo-cavity subsurface imaging. Photoacoustics 2019; 13: 66–75.

11. American National Standard for Safe Use of Lasers. Available at: https://loci.wisc.edu/sites/default/files/2017-04/American National Standard for Safe Use of Lasers.pdf. Accessed April 28, 2020.

12. Kumavor PD, Alqasemi U, Tavakoli B, Li H, Yang Y, Sun X, et al. Co-registered pulse-echo/photoacoustic transvaginal probe for real time imaging of ovarian tissue. J Biophotonics 2013; 6: 475–84.

13. Oraevsky AA, Andreev VA, Karabutov AA, Fleming RD, Gatalica Z, Singh H, et al. Laser optoacoustic imaging of the breast: detection of cancer angiogenesis [Internet]. In: Chance B, Alfano RR, Tromberg BJ, editors. Optical Tomography and Spectroscopy of Tissue III. Bellingham: SPIE; 1999: 352–63.

14. Leng X, Chapman W, Rao B, Nandy S, Chen R, Rais R, et al. Feasibility of co-registered ultrasound and acoustic-resolution photoacoustic imaging of human colorectal cancer. Biomed Opt Express. 2018; 9: 5159–72.

15. Horiguchi A, Shinchi M, Nakamura A, Wada T, Ito K, Asano T, et al. Pilot Study of Prostate Cancer Angiogenesis Imaging Using a Photoacoustic Imaging System. Urology.

2017; 108: 212–9.

16. Wong TTW, Zhang R, Hai P, Zhang C, Pleitez MA, Aft RL, et al. Fast label-free multilayered histology-like imaging of human breast cancer by photoacoustic microscopy. Sci Adv. 2017; 3: e1602168.

17. Lin L, Hu P, Shi J, Appleton CM, Maslov K, Li L, et al. Single-breath-hold photoacoustic computed tomography of the breast. Nat Commun 2018; 9: 2352.

18. Dogra VS, Chinni BK, Valluru KS, Moalem J, Giampoli EJ, Evans K, et al. Preliminary Results of Ex Vivo Multispectral Photoacoustic Imaging in the Management of Thyroid Cancer. Am J Roentgenol 2014; 202: W552–8.

19. Neuschler EI, Butler R, Young CA, Barke LD, Bertrand ML, Böhm-Vélez M, et al. A Pivotal Study of Optoacoustic Imaging to Diagnose Benign and Malignant Breast Masses: A New Evaluation Tool for Radiologists. Radiology. 2018; 287: 398–412.

20. Amidi E, Mostafa A, Nandy S, Yang G, Middleton W, Siegel C, et al. Classification of human ovarian cancer using functional, spectral, and imaging features obtained from in vivo photoacoustic imaging. Biomed Opt Express 2019; 10: 2303.

21. Kajita H, Oh A, Urano M, Takemaru M, Imanishi N, Otaki M, et al. Photoacoustic lymphangiography. J Surg Oncol 2020; 121: 48–50.

22. Knieling F, Neufert C, Hartmann A, Claussen J, Urich A, Egger C, et al. Multispectral Optoacoustic Tomography for Assessment of Crohn's Disease Activity. N Engl J Med 2017; 376:1292–4.

23. Jo J, Tian C, Xu G, Sarazin J, Schiopu E, Gandikota G, et al. Photoacoustic tomography

for human musculoskeletal imaging and inflammatory arthritis detection. Photoacoustics 2018; 12: 82–9.

24. Van Blerkom J, Antczak M, Schrader R. The developmental potential of the human oocyte is related to the dissolved oxygen content of follicular fluid: Association with vascular endothelial growth factor levels and perifollicular blood flow characteristics. Hum Reprod 1997; 12: 1047–55.

25. IEC 60825-1 Ed. 3.0 (2014); Safety of laser products – Part 1: Equipment classification and requirements. 2014.

26. International Commission on Non-ionizing Radiation Protection ICNIRP publication-2013 ICNIRP guidelines on limits of exposure to laser radiation of wavelengths between 180 nm and 1,000 μm. Health Physics 2013; 105: 271-95.

27. Valluru KS, Willmann JK. Clinical photoacoustic imaging of cancer. Ultrasonography 2016; 35: 267–80.

28. Luo H, Yang G, Zhu Q. Fiber endface illumination diffuser for endo-cavity photoacoustic imaging. Opt Lett 2020; 45: 632.

Chapter 7: A fiber endface photoacoustic generator for quantitative photoacoustic tomography

7.1 Introduction

Ultrasound (US) generators have long been studied for use in biomedical ultrasound imaging [1], focused ultrasound assisted drug delivery for treatment of tumors [2], and ultrasound non-destructive testing (NDT) [3]. However, the traditional piezo transducers are bulky, and fabricating these transducers with millimeter-scale lateral dimensions is both challenging and expensive.

Alternatively, optical ultrasound generators, especially fiber optic ultrasound generators, are attractive candidates for many ultrasound applications [4-5]. The most common optical ultrasound generation method exploits the PA effect [6], in which the generating material is excited by pulses of laser energy that cause transient heating and localized temperature rises. The temperature rise will cause contraction and expansion of the PA material due to thermal expansion effect. As a result, the periodic compression and expansion will generate acoustic mechanical waves. The PA waves' emission intensity is proportional to the light fluence and the absorption coefficient of the material. Due to the short pulse width of an ultra-fast laser, the pulse width of the generated acoustic signals can be very short, and the corresponding frequency bandwidth of acoustic signals can be broad.

Taking advantage of the submillimeter diameters of optical fibers and the PA effect, we developed a fiber-based PA wave generator (called a "PA generator" hereafter) that features a compact size and wide

bandwidth. The system is useful for a variety of applications such as quantitative evaluation of biological tissue absorption coefficients using photoacoustic imaging (PAI).

Accurately estimating functional parameters of biological tissue (e.g., total hemoglobin concentration and oxygen saturation) using PAI is challenging because the detected signals are a convolution of product of local fluence and tissue optical absorption with the system response. Computing the total hemoglobin concentration depends on the accurate estimation of local absorption profile of the tissue which is coupled with the local fluence. Nevertheless, by positioning the fiber endface of the calibrated PA generator close to the target tissue and assuming identical local fluence for the generator and tissue, we can assume that the mean PA signal ratio of the target tissue and the generator can approximate the ratio of their absorption coefficients provided that the absorption coefficients of PA generator and target tissue are linearly related. As a result, the absorption coefficient profile of the target tissue can be estimated by using the fiber endface PA generator as a reference. Such PA generators can be used with biopsy needles or surgical implantable devices for quantitative PAI. Additionally, these generators can also be imbedded inside the brain as broadband acoustic sources to activate neurons.

The PA wave generation material is an important factor. Recently, various studies have described developing and applying novel materials to improve PA wave generation efficiency. Several papers have reported that polymer-based materials show higher PA generation efficiency than metallic materials [7-8]. For instance, Biagi et al. demonstrated that, compared to metallic materials, graphite powder mixed with epoxy resin could increase the conversion efficiency by two orders of magnitude [9]. Zou et al. synthesized a gold nanocomposite by directly mixing gold nanoparticles with polydimethylsiloxane (PDMS), then coated it on the optical fiber tip for PA emission [10]. Baac et al. used a nano-composite film of carbon nanotubes (CNTs) and elastomeric polymer as an efficient PA source [8, 11]. Shi et al. combined multi-wall carbon nanotubes (MWCNTs) and PDMS to achieve a high light absorption coefficient and high

thermal expansion coefficient [12]. However, all of these PA generation materials involve complicated designs and demanding fabrication protocols. Moreover, they all lack a high optical absorption within 700-900 nm. Materials in reference [12] were designed for narrowband and sub-MHz frequency emission which are not suitable for most biomedical applications. Materials in reference [8, 11] required growing a multi-layer carbon nanotube on a fused silica substrate which is difficult to control its quality and extremely expensive. Also, PDMS based curing agent makes the manufacturing process time-consuming and difficult for controlling the fiber tip generator dimension precisely [7-12].

In this work, we report a fiber endface PA generator with a wide acoustic bandwidth, high thermal conversion efficiency, good PA singal controllability, and high feasibility (simple procedures). This novel generator could be a useful tool for calibrating the local absorption coefficient of biological tissue for quantitative PAI.

7.2 Methods and Materials

The fiber endface PA generator, as illustrated in Figure 7.1 (a) and Figure 7.1 (b), was fabricated by applying IR 144 dye (Exciton, Lockbourne, OH, USA) on the fiber tip. A piece of multimode fiber (FP1000ERT, 0.50 NA, THORLABS) with a core diameter of 1000 μm was stripped and cleaved, and the end face was polished. Then it was dipped into a mixture of IR 144 and UV adhesive (Norland Optical Adhesive 63, EDMUND OPTICS) and gradually pulled out to form a partial spherical tip due to the high viscosity and surface tension of the adhesive [13]. The tip ws exposed to UV light for several seconds for fast curing, then it was placed under a microscope for inspection. Any tip with a non-spherical shape was re-fabricated again. After the tip passes the inspection, it went through a UV exposure of several minutes to fully cure the UV adhesive.

IR 144 is a tricarbocyanine dye widely used in various biomedical applications employing near-infrared (NIR) imaging due to its high absorption cross-section at around 750 nm and strong fluorescent emission in the NIR regions. However, NIR-emitting dyes often have relatively low quantum yields (commonly in the range of 2-10% [14]) compared to the yields of traditional red-emitting fluorescent dyes (up to 96% [15]). The reported quantum yield value of IR 144 in DMSO is 5% [16], and the rest of the absorbed energy could lead to high thermal and thus PA conversion efficiency. Additionally, due to the presence of long extended conjugation in the chemical structure, IR 144 shows a high light energy conversion rate [17]. To our best knowledge, this is the first time that IR 144 has been used for PA wave generation.

We acquired the PA emission signals from the fiber endface photoacoustic generator and 200-μm diameter carbon fiber (approximated as a point source) using our previously described co-registered PAI/US imaging system [18]. The detected PA signals for each target were processed with FFT and the spectra are shown as a function of frequency (Figure 7.1 (c)). To briefly describe the PAI/US system, a Ti: Sapphire laser (Symphotics TII, LS-2122) optically pumped with a Q-switched Nd: YAG laser (Symphotics TII, LS-2134) was employed to deliver pulsed laser light (10-30 ns pulse duration, 15 Hz pulse repletion rate). For data acquisition, a commercial ultrasound system (EC-12R, Alpinion Medical Systems) and a linear ultrasound transducer (L3-12H, center frequency of 8.8 MHz and -6dB ultrasound bandwidth ≥60%) were used.

As shown in Figure 7.1 (c), the PA generator spectrum (brown color) in 2 to 7 MHz range closely follows the carbon fiber spectrum (blue) indicating a broad PA signal bandwidth of the IR 144 dye. The -30dB width of the PA generator and the 200-μm carbon fiber is 2.1-6.6 MHz and 2.2-6.8MHz, respectively.

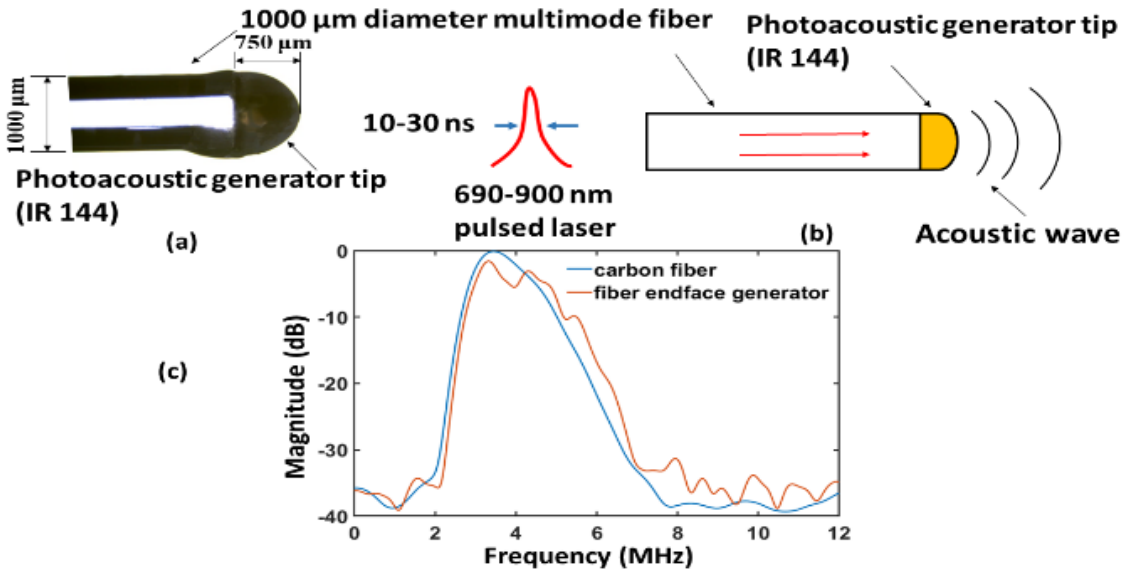

Figure 7.1: (a) Microphotograph of the fiber endface PA generator; (b) Schematic of the generator; (c) The frequency response of the PA generator and 200-µm diameter carbon fiber.

7.3 Results

The absorbance was calculated by $\log_{10}(I_0/I)$, where I_0 and I are the intensity of incident and transmitted light, respectively. By measuring absorbance at different wavelength, the absorption spectrum of IR 144 was obtained with a Beckman DU-640 spectrophotometer (Beckman Coulter, Inc., Indianapolis, IN, USA). A stock solution of IR 144 was prepared in DMSO (1 mg/ml) from which IR 144 samples with different concentrations were diluted. The samples were placed in quartz cuvettes, and their UV-Vis absorption spectra were recorded.

Figure 7.2 (a) shows absorbance versus wavelength plots for IR 144 concentrations from 0.3125 to 20 µg/ml. The peak absorbance occurs at around 745 nm. Also, the plots suggest that absorbance increases with IR144 concentration. Figure 7.2 (b) shows the peak absorbance value occurring at 745 nm as a function of IR 144 concentrations. The linear relationship of the peak absorbance and the IR144 concentrations indicates an R^2 of 0.9963. We also calculated the mean PA signal from

the recorded PA generator signals. We selected an appropriate region of interest (ROI) based on the ultrasound image and calculated the mean value of the PAT image envelopes within the ROI. Then we normalized the mean value to the corresponding fiber tip power measured by a power meter to obtain the normalized mean PA signal at each wavelength. Figure 7.2 (c) shows the normalized mean PA signal and the corresponding absorbance for wavelengths from 730 to 850 nm. The plots of the PA signal and absorbance follow similar trends, which are in accord with the PA principle that the profile of the acoustic signals is similar to the profile of the absorption coefficient for a constant fluence.

Figure 7.3 (a) shows the experimental setup for validating the calibration accuracy of the fiber endface PA generator. Three generators with three concentrations were buried with equal lateral distance inside a calibrated phantom (made of intralpid and gelatin, absorption coefficient μ_a, 0.02 cm^{-1}; reduced scattering coefficient μ_s', 4 cm^{-1}) at a depth of 20 mm. Guided by co-registered US images, the three generators were oriented perpendicular to the transducer imaging plane. However, small angles might occur and the PA signal variation was less than 3% which would not affect the results. Figure 7.3 (b) and Figure 7.3 (c) show the corresponding 1-D profiles across the three fiber endface PA generators for two sets of concentrations (2.5, 5, and 10 μg/ml; and 1.25, 2.5, and 5 μg/ml) acquired from the PA images at 745 nm. Based on the linear relationship of IR 144's absorbance and concentration at 745 nm (Figure 7.2 (b)), the true PA signal ratio of the generators with adjacent higher to lower IR 144 concentrations is around 2, which is consistent with the experimental ratios: 1.74 and 1.78 marked in Figure 7.3 (b), and 2.27 and 1.87 in Figure 7.3(c).

Figure 7.4 (a) shows the experimental setup of the PA generator calibration with either of two targets: cypate (Optical Radiology Lab, Washington University in St. Louis) and IR 140 (Exciton, Lockbourne,

OH, USA). Just as in Figure 7.3 (a), one fiber endface generator and one target were buried inside the calibrated phantom perpendicular to the transducer imaging plane at a depth of 20 mm.

The laser wavelength was 745 nm, and the IR 144 concentration was 2.5 μg/ml. Cypate and IR 140 are two frequently used NIR dyes with absorbance in the 700-900 nm range. The measured absorbance of the cypate and IR 140 samples at 745 nm were 0.92 and 0.97. Based on the results in Figure 7.2 (a), the measured absorbance of the fiber endface PA generator (2.5 μg/ml) at 745 nm was 0.39. As a result, the true PA signal ratios of cypate and IR 140 to the signal of the generator were 2.49 and 2.36, which match well with the experimental ratios: 2.34 in Figure 7.4 (b) and 2.18 in Figure 7.4 (c).

Figure 7.5 (a) shows the experimental setup of the fiber endface PA generator calibration of a mouse blood sample. The mouse blood samples were collected from a C57BL/KaLwRij mouse (10 weeks old) via cardiac puncture under deep anesthesia and transferred into EDTA tubes to prevent blood coagulation. The blood samples were diluted with saline water to achieve different absorbances. Then it was injected into a 5 mm diameter tube which was then tightly capped. The fiber generator and blood tube were submerged inside a tank filled with 0.4% calibrated intralipid solution (Fresenius Kabi, USA) perpendicular to the transducer imaging plane at a depth of 20 mm. The intralipid solution had a μ_a of 0.02 cm^{-1} and μ_s' of 4 cm^{-1}. The laser wavelength used here was 745 nm and the IR 144 concentration was 2.5 μg/ml. As shown in Figure 7.5 (b), strong PA signals (yellow) were detected from the generator and blood tube area (gray).

Meanwhile, second reflection PA artifacts were observed underneath the blood PA signals at a depth roughly two times that of the blood PA signals due to transducer face absorption. The measured absorbance of the fiber endface PA generator (2.5 μg/ml) and blood sample (diluted 20 times) at 745 nm were 0.39 and 2.04.

As a result, the true ratio of the PA signals of the blood sample and the generator was 5.22, which agrees well with the experimental ratio in Figure 7.5 (c). Figure 7.5 (d) shows the mean PA signal value of the blood sample at 745 nm as a function of the measured blood sample absorbance (1.09, 1.67, 2.1, 2.59) with respect to different dilution rates (~ 30, 25, 20, 15 times). The linear relationship of the mean PA signal and the blood sample absorbance indicates an R^2 of 0.98. We also compared the experimental blood sample absorption coefficients with respect to different dilution rate and the measured ones and there showed a good match with a difference less than 0.5 cm^{-1} in Figure 7.5 (e).

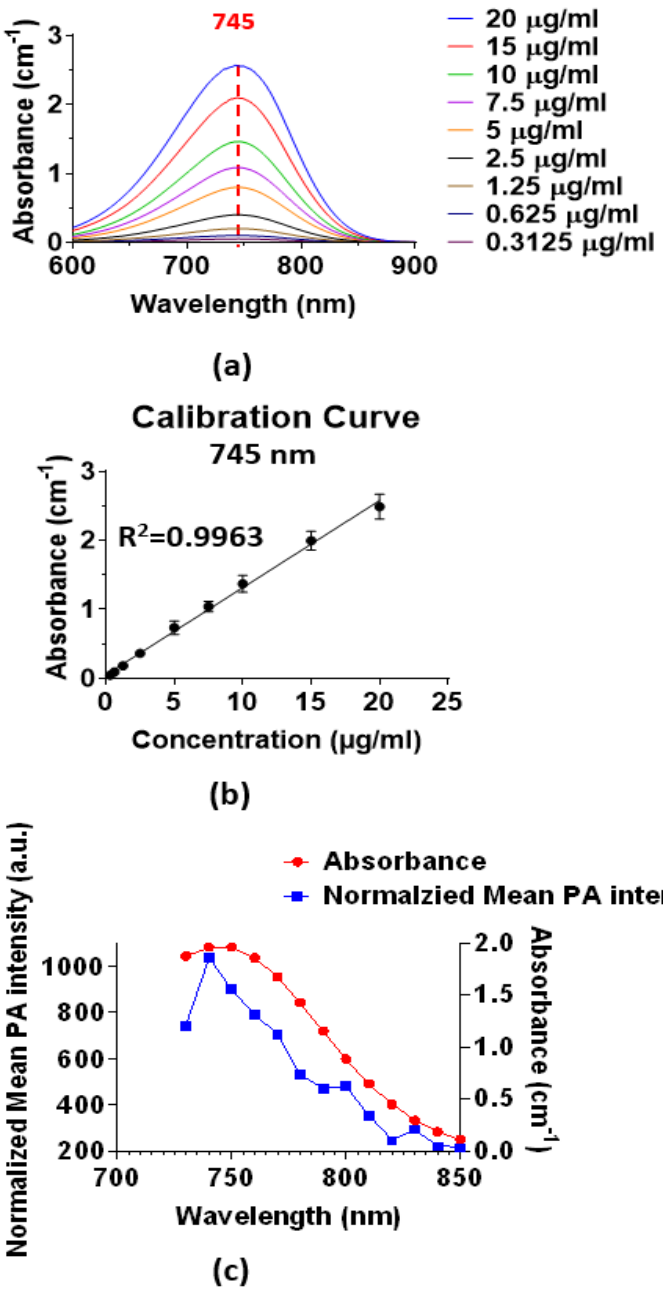

Figure 7.2: (a) Absorbance plots of IR 144 as a function of wavelength for concentrations from 0.3125 to 20 µg/ml (solvent: DMSO); (b) The peak absorbance value at 745 nm as a function of IR144 concentrations; (c) The normalized mean PA intensity and the corresponding absorbance as a function of wavelength.

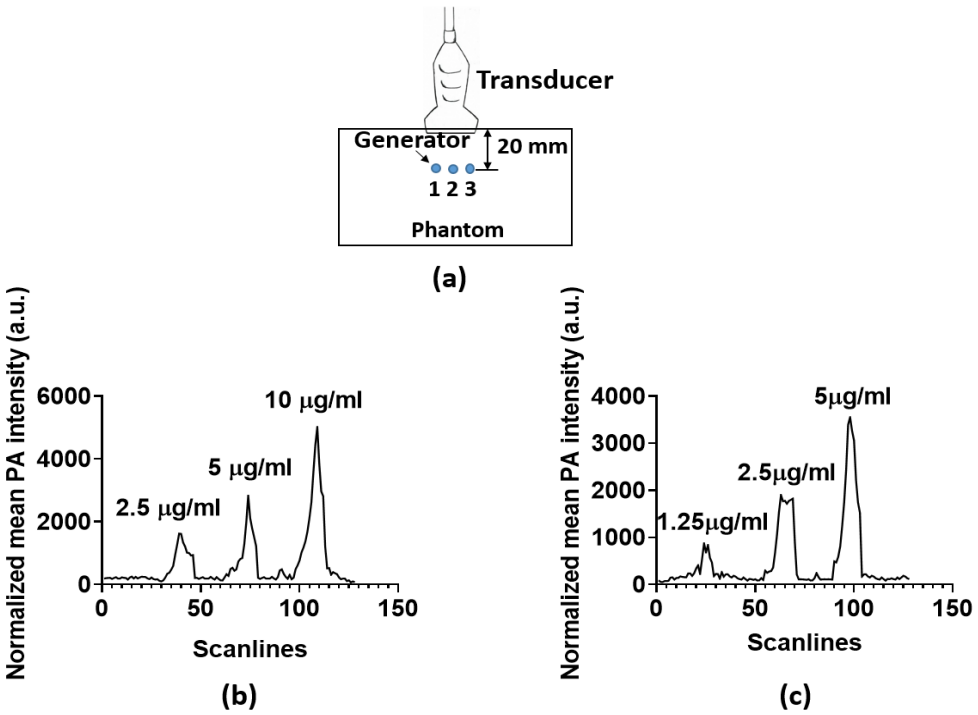

Figure 7.3: (a) Experimental setup to validate the calibration accuracy of the fiber endface PA generator (the light was delivered through the fiber itself to its endface); (b) and (c) Corresponding 1-D profiles across three different fiber endface PA generators (averaged from 10 consecutive envelopes along the depth) with respect to two sets of IR 144 concentrations (2.5, 5, and 10 μg/ml; and 1.25, 2.5, and 5 μg/ml). The PA intensity ratios of the generators with higher to lower IR 144 concentrations are also provided in each profile.

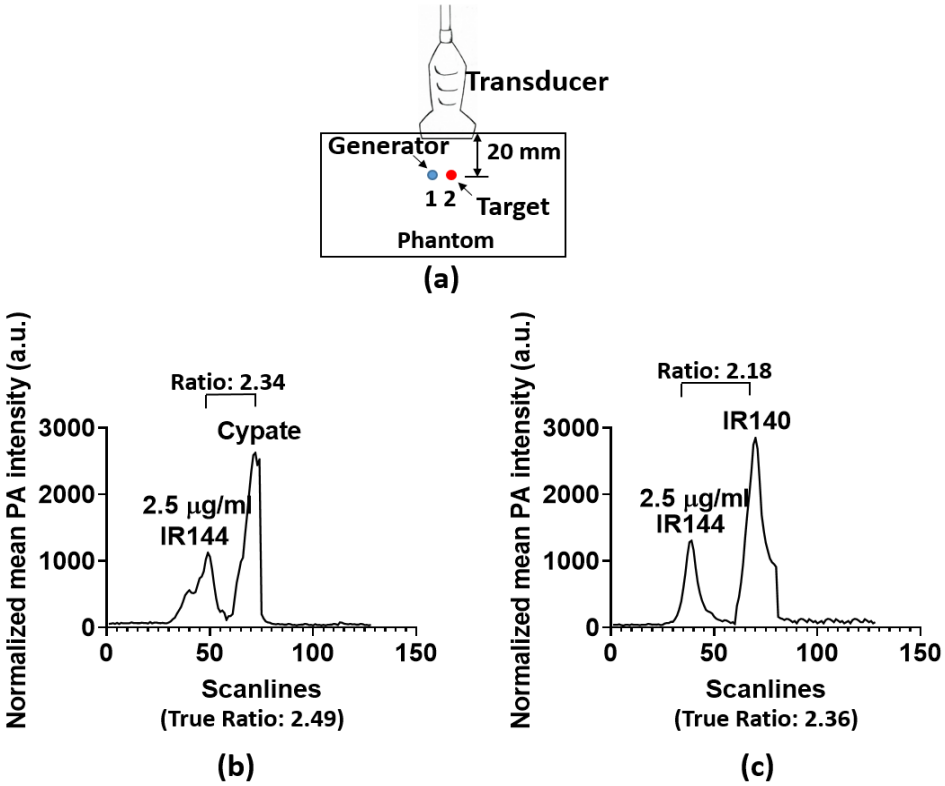

Figure 7.4: (a) Experimental setup of the PA generator target calibration (the light was delivered through the fiber itself to its endface); (b) and (c) Corresponding 1-D profiles (averaged from 10 consecutive envelopes along the depth) across one PA generator (left, IR 144 with a concentration of 2.5 µg/ml) and one target (right, cypate and IR 140). The ratios of the PA intensity of the target to that of the generator are also provided in each profile.

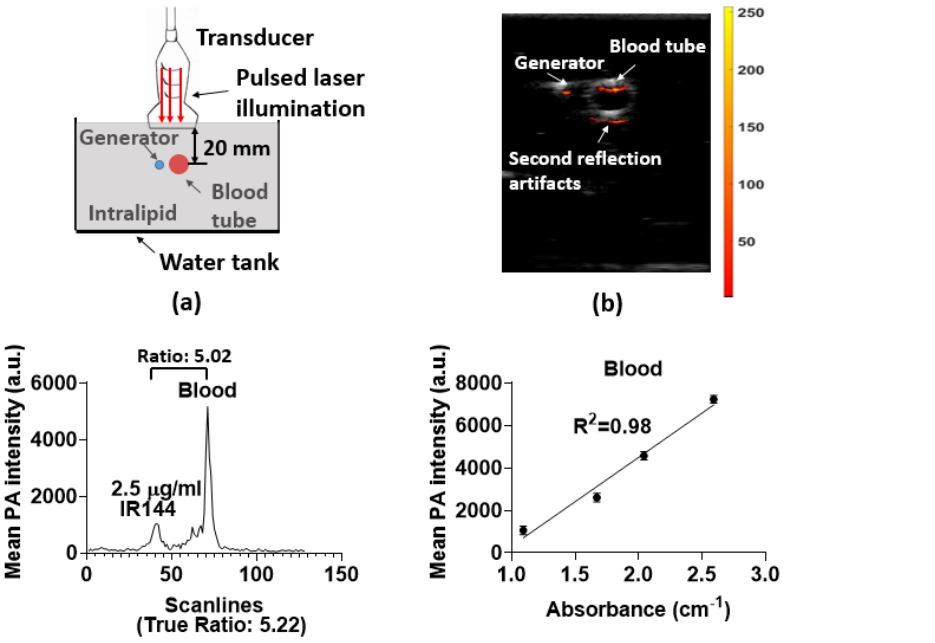

Blood sample	Experimental absorption coefficient (cm^{-1})	Measured absorption coefficient (cm^{-1})	Error (cm^{-1})
Concentration1	2.30	2.51	0.21
Concentration2	3.96	3.85	0.11
Concentration3	4.51	4.84	0.33
Concentration4	6.29	5.96	0.33

(e)

Figure 7.5: (a) Experimental setup of the fiber endface PA generator calibration of a mouse blood sample (the light was delivered from the top of the water tank perpendicular to the intralipid solution); (b) Co-registered PA/US images of the generator and mouse blood sample (dynamic range: 18 dB, colorbar refers to normalized PA signal); (c) The corresponding 1-D profile (averaged over 2 mm in depth) across one fiber endface generator (left, IR 144 with a concentration of 2.5 µg/ml) and one mouse blood sample (right, injected into a 5 mm diameter tube). The PA intensity ratio of the blood sample's intensity to the generator's intensity is also provided; (d) The mean PA intensity value of the blood sample at 745 nm as a function of the measured blood sample absorbances with respect to different dilution rates; (e) The comparison between the experimental

absorption coefficient of the blood sample based on the mean PA signal ratio and the measured absorption coefficient based on the spectrophotometer measurement (concentration 1-4 refer to 4 dilution rates of the blood sample).

7.4 Discussion and Summary

In this paper, we have demonstrated a novel fiber endface PA generator, made of a mixture of IR 144 and UV adhesive. IR 144 has been widely used in various biomedical applications with signals in the NIR range. With a high absorption cross-section and low quantum yield (5%), it achieved a high thermal conversion efficiency (>90%) and thus high PA conversion efficiency. The PA emission frequency exhibited a broad bandwidth as the point-like carbon fiber. The IR 144 absorbance at 745 nm was linearly correlated with its concentration with an R^2 of 0.9963. By experimentally validating the generator's calibration accuracy with different concentrations and different target materials, we demonstrated good consistency between the experimental and calibration results. Finally, we used the generator to calibrate the absorption coefficient of a mouse blood sample, mimicking biological tissue. Again, there was a good match between the experimental and calibration results with a difference less than 0.5 cm^{-1}.

In summary, we have introduced a novel fiber endface PA generator using IR 144 dye which can be a broadly useful tool in biomedical applications. We have demonstrated experimentally that the generated PA signal has a broadband width in the frequency range of 2-7 MHz evaluated and linearly increases with the dye concentration up to 20 μg/ml. The generator can be used as a reference to calibrate local absorption of the tissue. Additionally, IR 144 dye is commercially available which can facilitate clinical translation of such fiber-based acoustic generators. Moreover, dual modality fluorescent and

photoacoustic imaging can be achieved by utilizing IR 144's moderate quantum yield in NIR region and the good PA conversion efficiency.

References

1. A. Baerwald, S. Dauk, R. Kanthan, and J. Singh. "Use of ultrasound biomicroscopy to image human ovaries in vitro." Ultrasound in Obstetrics and Gynecology: The Official Journal of the International Society of Ultrasound in Obstetrics and Gynecology 34, 2 (2009).

2. J. Qin, T. Y. Wang, and J. K. Willmann. "Sonoporation: applications for cancer therapy." Therapeutic Ultrasound (2016).

3. G. Sposito, C. Ward, P. Cawley, P. B. Nagy, and C. Scruby. "A review of non-destructive techniques for the detection of creep damage in power plant steels." Ndt & E International 43 (2010).

4. X. Zou, N. Wu, Y. Tian, Y. Zhang, and X. Wang. "Polydimethylsiloxane thin film characterization using all-optical photoacoustic mechanism." Applied optics 52, 25 (2013).

5. Y. Tian, N. Wu, X. Zou, H. Felemban, C. Cao, and X. Wang. "Fiber-optic ultrasound generator using periodic gold nanopores fabricated by a focused ion beam." Optical Engineering 52, 6 (2013).

6. L. V. Wang, and S. Hu. "Photoacoustic tomography: in vivo imaging from organelles to organs." Science 335, 6075 (2012).

7. N. Wu, Y. Tian, X. Zou, V. Silva, A. Chery, and X. Wang. "High-efficiency optical ultrasound generation using one-pot synthesized polydimethylsiloxane-gold nanoparticle nanocomposite." JOSA B 29, 8 (2012).

8. H. W. Baac, J. G. Ok, H. J. Park, T. Ling, S. L. Chen, A. J. Hart, and L. J. Guo. "Carbon nanotube composite optoacoustic transmitters for strong and high frequency ultrasound generation." Applied physics letters 97, 23 (2010).

9. E. Biagi, F. Margheri, and D. Menichelli. "Efficient laser-ultrasound generation by using heavily absorbing films as targets." ieee transactions on ultrasonics, ferroelectrics, and frequency control 48, 6 (2001).

10. X. Zou, N. Wu, Y. Tian, and X. Wang. "Broadband miniature fiber optic ultrasound generator." Optics express 22, 15 (2014).

11. H. W. Baac, J. G. Ok, A. Maxwell, K. T. Lee, Y. C. Chen, A. J. Hart, ... and L. J. Guo. "Carbon-nanotube optoacoustic lens for focused ultrasound generation and high-precision targeted therapy." Scientific reports 2, 1 (2012).

12. L. Shi, Y. Jiang, Y. Zhang, L. Lan, Y. Huang, J. X. Cheng, and C. Yang. "A fiber optoacoustic emitter with controlled ultrasound frequency for cell membrane sonoporation at submillimeter spatial resolution." Photoacoustics 20 (2020).

13. H. Luo, G. Yang, and Q. Zhu. "Fiber endface illumination diffuser for endo-cavity photoacoustic imaging." Optics letters 45, 3 (2020).

14. P. Xu, F. Kang, W. Yang, M. Zhang, R. Dang, P. Jiang, and J. Wang. "Molecular engineering of a high quantum yield NIR-II molecular fluorophore with aggregation-induced emission (AIE) characteristics for in vivo imaging." Nanoscale 12, 8 (2020).

15. R. F. Kubin, and A. N. Fletcher. "Fluorescence quantum yields of some rhodamine dyes." Journal of Luminescence 27, 4 (1982).

16. J. Mohanty, D. K. Palit, and J. P. Mittal. "Photophysical properties of two infrared laser dyes--IR-144 and IR-140: A picosecond laser flash photolysis study." Proceedings-Indian National Science Academy Part A 66, 2 (2000).

17. F. A. Castro, A. Faes, T. Geiger, C. F. Graeff, M. Nagel, F. Nüesch, and R. Hany. "On the use of cyanine dyes as low-bandgap materials in bulk heterojunction photovoltaic devices." Synthetic Metals 156 (2006).

18. G. Yang, E. Amidi, S. Nandy, A. Mostafa, and Q. Zhu. "Optimized light delivery probe using ball lenses for co-registered photoacoustic and ultrasound endo-cavity subsurface imaging." Photoacoustics 13 (2019).

Chapter 8: Summary and Future Work

8.1 Summary

This dissertation is focused on exploring co-registered photoacoustic and ultrasound tomographic imaging on two fatal cancers: ovarian cancer and colorectal cancer. It is composed of three main parts: light delivery optimization/fiber optics, system development and optimization, and pilot patient and sample study. First project described in chapter two is related to the light delivery optimization/fiber optics part. We designed and evaluated an optimized hand-held photoacoustic and ultrasound probe suitable for endo-cavity tumor subsurface imaging. Compared to previous designs, the prototype probe, consisting of four 1 mm multi-mode optical fibers attached with 1.5 mm diameter ball-shaped fiber tips sandwiched between a transvaginal ultrasound transducer and a custom-made sheath, demonstrated a higher light output and better beam homogeneity on tissue subsurface. The simulations and experiments demonstrated that ball-shaped fiber tip design can achieve homogeneous fluence distribution on tissue subsurface with acceptable light output efficiency, suggesting its clinical potential for in-vivo endo-cavity imaging. Based on the ball lens design, we made an improved version of design in chapter three in which we developed an effective fiber diffuser tip to reduce the fluence on the target tissue surface while injecting more laser energy and enhancing the photoacoustic signal generated from the tissue. The fiber diffuser tip is made of silica microspheres mixed with UV adhesive. We compared the light diffusion effects of different microsphere materials, sizes, and concentrations, and find 10 μm silica microspheres provide the best light scattering with minimal 5% output energy loss. With Zemax simulation and experimental validation, we show this fiber diffuser tip could be a valuable tool for endo-cavity photoacoustic imaging.

In chapter four, we proposed an improved beamformer named lag-based delay multiply and sum combined with coherence factor (DMAS-LAG-CF). Simulations and phantom experiments demonstrate that compared with the conventional DAS, the proposed algorithm can provide 1.39 times better resolution and 10.77 dB higher contrast. With a cohort of 28 patient data, similar performance on contrast ratios have been observed. However, since the diagnostic accuracy between cancer and benign/normal groups is the significant measure, we have extracted photoacoustic histogram features of mean, kurtosis and skewness. DMAS-LAG-CF can improve cancer diagnosis with an AUC of 0.91 for distinguishing malignant vs. benign ovarian lesions when mean and skewness are used as features.

Continuing the pilot clinical patient/sample study, we have conducted a pilot study on 23 *ex-vivo* human colorectal tissue samples immediately after the surgical resection to investigate the ability of co-registered photoacoustic and ultrasound tomographic imaging to assess human colorectal cancer in chapter five. Co-registered photoacoustic images of malignancies showed significantly increased PAT signal compared to normal regions of the same sample. The quantitative relative total hemoglobin concentration (rHbT) computed from four optical wavelengths, the spectral features, such as the mean spectral slope, and 0.5 MHz intercept extracted from PAT and US spectral data, and image features, such as the first and second order statistics along with the standard deviation of the mean radon transform of PAT images, have shown statistical significance between untreated colorectal tumors and the normal tissue. Using either a logistic regression model or a support vector machine, the best set of parameters of rHbT and PAT intercept has achieved AUC values of 0.97 and 0.95 for both training and testing data sets respectively for prediction of histologically confirmed invasive carcinoma.

One limitation of the current system is the poor image resolution (~ 250 μm axial resolution) due to the commercial endo-cavity ultrasound transducer array (6 MHz central frequency, 80% bandwidth). To solve the problem of image resolution, we firstly decoded the pin configuration of a high-frequency transducer array (15 MHz central frequency, 9-18 MHz bandwidth) and adapted it to our home-made 128 channels ultrasound pulsing and receiving system (sampling rate: 40 MHz) to perform high frequency PAT/US imaging. To further improve the performance of photoacoustic data acquisition suitable for high-frequency transducer array, we are building a 64-channel FPGA based high frequency photoacoustic imaging system with a sampling rate of 80 MHz and signal-to-noise ratio (SNR) of 40 dB, and adapting this system to an endo-rectal probe with a side-firing fiber tip for *in-vivo* patient study.

In chapter six, since we did a lot clinical applications on human ovarian cancer and colorectal cancer, we'd like to investigate the laser safety of photoacoustic imaging especially before its adoption by clinical reproductive medicine. Potential DNA damage of photoacoustic laser exposure on preimplantation mouse blastocyst stage embryos was examined. Different embryos groups were exposed to either 5- or 10- minute 15-Hz laser doses (typical clinical doses), and 1-minute 1-kHz laser dose (significantly higher dose), respectively. We demonstrated that typical lasers and exposure times used for photoacoustic imaging do not induce increased cell death in mouse blastocysts.

In chapter seven, we presented a novel fiber endface photoacoustic generator using IR 144 dispersed within an UV adhesive. The generator provides wide acoustic bandwidth in the transducer frequency range of 2-7MHz, high thermal conversion efficiency (> 90%), good PA intensity controllability (well controlled IR 144 concentration), and high feasibility (simple procedures). Through a series of experimental validations, we show this fiber endface photoacoustic

generator can be a useful tool for a broad range of biomedical applications, such as calibrating the local absorption coefficient of biological tissue towards quantitative photoacoustic tomography.

8.2 Future Work

8.2.1 Transmission-mode Ultrasound Imaging Using the Fiber Endface Photoacoustic Generator

To demonstrate the capability of the fiber endface photoacoustic generator to image tumor morphology, we performed a simple model experiment, as shown in Figure 8.1(a). We used a motorized stage to move the fiber tip acoustic generator to several positions and recorded the acoustic signal with a linear transducer array. We put a soft plastic tube between the acoustic generator and linear transducer array to mimic a tumor. By calculating the acoustic attenuation induced by the tube from several different angles, we could reconstruct the tumor shape as shown in Figure 8.1(b). If we progress to consider real biological tissues, we can coat materials with different absorption peaks on different tips so that we can tune the laser light wavelength to control the acoustic emission at different positions, instead of mechanically changing the fiber tip position.

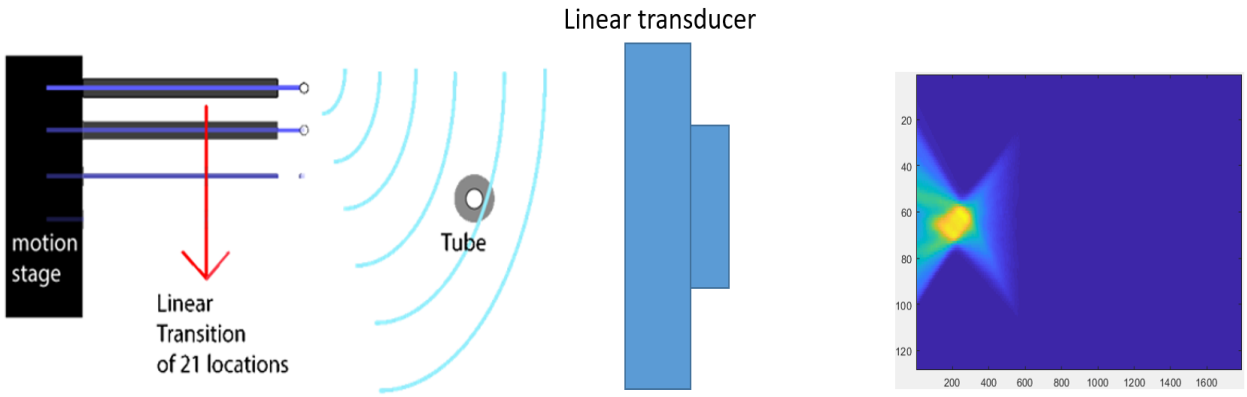

(a) **(b)**

Figure 8.1: (a) Schematic of fiber endface photoacoustic generator for transmission-mode ultrasound imaging of the tumor mimicking soft tube. (b) The Reconstruction result of the soft tube.

8.2.2 Photoacoustic Remote-sensing Imaging of Human Ovarian and Colorectal Cancer

Photoacoustic methods have demonstrated great success in many applications. However, for many clinical applications, such as wound healing, burn diagnostics, surgery and many endoscopic procedures, physical contact, coupling, or immersion is undesirable or impractical. Optical methods to detect ultrasound and photoacoustic signals have been investigated over a number of years. Very recently, Hajireza et al. proposed a non-interferometric photoacoustic remote sensing microscopy (PARS) which intentionally eliminated phase-sensitivity to exclusively monitor intensity reflectivity changes [1]. This work introduces a new mechanism and methodology to detect photoacoustic signals at the subsurface origin, where pressures are maximal. Elasto-optical refractive index changes due to photoacoustic initial pressure transients are shown to produce a significant time-varying reflection of a probe beam. Lots of applications have been demonstrated

using PARS especially on digital histology [2-3]. Also they combined PARS with optical coherence tomography (OCT) for better cancer diagnosis [4-5]. I believe PARS could be a very powerful tool for ovarian cancer and colorectal cancer diagnosis.

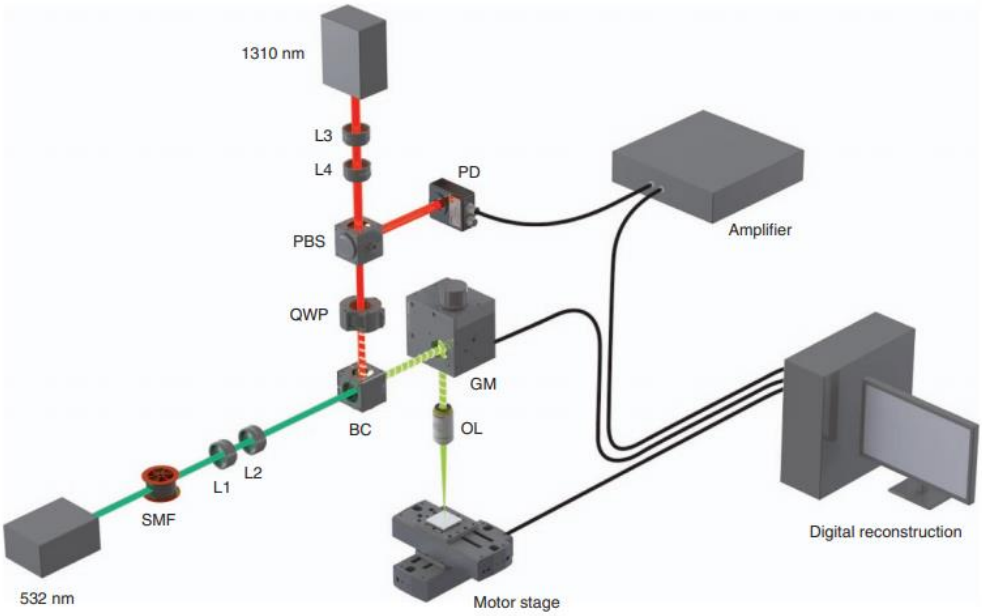

Figure 8.2: Experimental setup of photoacoustic remote-sensing microscopy (PARS) with 532-nm excitation and 1310-nm integration beams (from Ref. [1]).

References

1. Hajireza, P., Shi, W., Bell, K., Paproski, R. J., & Zemp, R. J. (2017). Non-interferometric photoacoustic remote sensing microscopy. Light: Science & Applications, 6(6), e16278-e16278.

2. Restall, B. S., Haven, N. J., Kedarisetti, P., & Zemp, R. J. (2020). In vivo combined virtual histology and vascular imaging with dual-wavelength photoacoustic remote sensing microscopy. OSA Continuum, 3(10), 2680-2689.

3. Haven, N. J., Kedarisetti, P., Restall, B. S., & Zemp, R. J. (2020). Reflective objective-based ultraviolet photoacoustic remote sensing virtual histopathology. Optics Letters, 45(2), 535-538.

4. Martell, M. T., Haven, N. J., & Zemp, R. J. (2020). Multimodal imaging with spectral-domain optical coherence tomography and photoacoustic remote sensing microscopy. Optics Letters, 45(17), 4859-4862.

5. Martell, M. T., Haven, N. J., Kedarisetti, P., Zemp, R. J., & Restall, B. (2021, March). Towards non-contact functional oxygen metabolism estimation with multi-wavelength photoacoustic remote sensing and Doppler optical coherence tomography. In Photons Plus Ultrasound: Imaging and Sensing 2021 (Vol. 11642, p. 1164233). International Society for Optics and Photonics.